STRUCTURAL AND ELECTRICAL PROPERTIES OF $CaCu_3Ti_4O_{12}$ THIN FILMS
AND THEIR APPLICATIONS
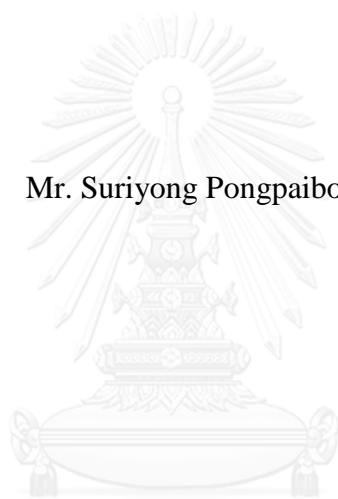
Mr. Suriyong Pongpaiboonkul

A Dissertation Submitted in Partial Fulfillment of the Requirements

for the Degree of Doctor of Philosophy Program in Nanoscience and Technology

(Interdisciplinary Program)

Graduate School

Chulalongkorn University

Academic Year 2015

Copyright of Chulalongkorn University

สมบัติทางโครงสร้างและทางไฟฟ้าของฟิล์มบางแคลเซียมคอปเปอร์ไททาเนตและการประยุกต์

นายสุริยงค์ พงศ์ไพบูลย์กุล

Thesis Title	STRUCTURAL AND ELECTRICAL PROPERTIES OF $CaCu_3Ti_4O_{12}$ THIN FILMS AND THEIR APPLICATIONS
By	Mr. Suriyong Pongpaiboonkul
Field of Study	Nanoscience and Technology
Thesis Advisor	Associate Professor Dr. Satreerat Hodak
Thesis Co-Advisor	Dr. Anurat Wisitsoraat
	Dr. Narongchai Boonyopakon

Accepted by the Graduate School, Chulalongkorn University in Partial Fulfillment of the Requirements for the Doctoral Degree

---Dean of the Graduate School
(Associate Professor Sunait Chutintaranond)

THESIS COMMITTEE

---Chairman
(Associate Professor Dr. Vudhichai Parasuk)
---Thesis Advisor
(Associate Professor Dr. Satreerat Hodak)
---Thesis Co-Advisor
(Dr. Anurat Wisitsoraat)
---Thesis Co-Advisor
(Dr. Narongchai Boonyopakon)
---Examiner
(Assistant Professor Dr. Yuttanant Boonyongmaneerat)
---Examiner
(Dr. Ratthapol Rangkupan)
---Examiner
(Assistant Professor Dr. Sukkaneste Tungasmita)
---External Examiner
(Associate Professor Dr. Pongkaew Udomsamuthirun)

สุริยงค์ พงศ์ไพบูลย์กุล : สมบัติทางโครงสร้างและทางไฟฟ้าของฟิล์มบางแคลเซียมคอปเปอร์ไททาเนตและ การประยุกต์ (STRUCTURAL AND ELECTRICAL PROPERTIES OF CaCu₃Ti₄O₁₂ THIN FILMS AND THEIR APPLICATIONS) อ.ที่ปรึกษาวิทยานิพนธ์หลัก: รศ. ดร. สตรีรัตน์ โฮดัค, อ.ที่ปรึกษา วิทยานิพนธ์ร่วม: ดร. อนุรัตน์ วิศิษฐ์สรอรรถ, อ. ดร. ณรงค์ชัย บุญโญปกรณ์, 154 หน้า.

ในงานวิจัยนี้ผลการเจือเหล็กในฟิล์มบางแคลเซียมคอปเปอร์ไททาเนตและสมบัติการตอบสนองต่อแก๊สเตรียม โดยวิธีโซล-เจล (sol- gel) มีการศึกษาอย่างเป็นระบบฟิล์มบางแคลเซียมคอปเปอร์ไททาเนตที่เจือด้วยเหล็กที่มีความ เข้มข้นต่างกันถูกปลูกลงบนแผ่นรองรับอลูมินาด้วยวิธีปั่นหมุน (spin coating) และการทำแพทเทิร์นขั้วไฟฟ้าทอง/ โครเมียมลงบนฟิล์มบางด้วยวิธีลิโทกราฟี (lithography) กระบวนการสปัตเตอร์ริ่ง (sputtering) และการลิฟท์-ออฟ (lift-off) การศึกษาลักษณะเฉพาะของฟิล์มบางแคลเซียมคอปเปอร์ไททาเนตด้วยเทคนิคการเลี้ยวเบนรังสีเอกซ์ (X-ray diffraction) เทคนิคกล้องจุลทรรศน์แรงอะตอม (atomic force microscopy) กล้องจุลทรรศน์อิเล็กตรอนแบบส่องกราด ชนิดฟิลด์อีมิสชั่น (FESEM) รามานสเปกโทรสโกปี (Raman spectroscopy) เอกซเรย์โฟโตอีมิสชั่นสเปกโทรสโกปี (X-ray photoemission spectroscopy) เทคนิคเหล่านี้ยืนยันการมีโครงสร้างเพอรอฟสไกต์ออกไซด์ (perovskite oxide) ของ แคลเซียมคอปเปอร์ไททาเนตและเฟสเจือปนไททเนียมไดออกไซด์และคอปเปอร์ออกไซด์ภายในฟิล์มบางและยืนยันการ แทนที่ของอะตอมเหล็กที่มีค่าออกซิเดชัน +3 ในตำแหน่งไททาเนียมที่มีค่าออกซิเดชัน +4 ในโครงสร้างผลึก จากการวัด การตอบสนองต่อแก๊สไฮโดรเจนซัลไฟด์พบว่าสารเจือปนเหล็กช่วยเพิ่มการตอบสนองต่อแก๊สไฮโดรเจนซัลไฟด์ ความไว ในการตอบสนองและความจำเพาะในการตอบสนองต่อแก๊สไฮโดรเจนซัลไฟด์เทียบกับแก๊สชนิดอื่นๆ เช่น แอมโมเนีย คาร์บอนมอนอกไซด์ อะเซทิลีน มีเทน เอทานอล และไนโตรเจนไดออกไซด์ โดยเฉพาะที่ปริมาณการเจือ 9 เปอร์เซ็นต์โดยน้ำหนักหรือประมาณ 3 เปอร์เซ็นต์โดยอะตอม อุปกรณ์เซนเซอร์แสดงผลการตอบรับสูงสุดประมาณ 126 ที่ 10 พีพีเอ็ม ของไฮโดรเจนซัลไฟด์ ซึ่งการตอบสนองแก๊สสูงกว่าฟิล์มที่ไม่เจือเหล็กที่อุณหภูมิการดำเนินการ 250 องศา เซลเซียส บทบาทของสารเจือปนเหล็กต่อกลไกของการตอบสนองแก๊สของแคลเซียมคอปเปอร์ไททาเนตได้รายงานผลใน งานวิจัยนี้ การจัดเรียงตัวสูงของระนาบเฉพาะของฟิล์มบางแคลเซียมคอปเปอร์ไททาเนตปลูกลงบนแผ่นรองรับแลน ทานั่มอลูมิเนตระนาบหนึ่งศูนย์ศูนย์ (LAO(100)) นีโอดีเมียมแกลเลตระนาบ 100 และ 110 (NGO(100) และ (110)) ด้วย วิธีโซลเจล แผ่นรองรับเหล่านี้ได้เลือกมาเพื่อการปลูกฟิล์มบางแคลเซียมคอปเปอร์ไททาเนตเนื่องจากมีความแตกต่างของ การเข้าคู่ระหว่างแลตทิชของฟิล์มและแผ่นรองรับน้อย (small lattice mismatch) การเลี้ยวเบนของรังสีเอกซ์แสดงให้ ทราบว่า ชั้นฟิล์มบางแคลเซียมคอปเปอร์ไททาเนตตั้งฉากกับแผ่นรองรับ (c-axis perpendicular) ภาพพื้นผิวและ ภาคตัดขวางแสดงความเรียบและพื้นผิวที่ไม่มีรอยร้าวและขนาดของพื้นผิวเกรนที่ใหญ่และจับตัวกันอย่างหนาแน่น รอยต่อระหว่างฟิล์มกับแผ่นรองรับผลึกเดี่ยวคมชัด ในงานวิจัยนี้ พบว่าการจัดเรียงตัวของระนาบเฉพาะของฟิล์มบาง แคลเซียมคอปเปอร์ไททาเนตสามารถที่จะถูกปรับเปลี่ยนได้โดยการปลูกผลึกลงบนแผ่นรองรับที่ต่างชนิดและต่างระนาบ โดยไม่ต้องมีชั้นบัฟเฟอร์นำไฟฟ้าขั้นระหว่างฟิล์มและแผ่นรองรับ ความสัมพันธ์ระหว่างการจัดเรียงตัวที่ชอบมากกว่า ระนาบอื่น ๆ ของฟิล์มบางแคลเซียมคอปเปอร์ไททาเนตและสมบัติทางไดอิเล็กทริกถูกรายงานและนำเสนอ

สาขาวิชา วิทยาศาสตร์นาโนและเทคโนโลยี	ลายมือชื่อนิสิต _____
ปีการศึกษา 2558	ลายมือชื่อ อ.ที่ปรึกษาหลัก _____
	ลายมือชื่อ อ.ที่ปรึกษาร่วม _____
	ลายมือชื่อ อ.ที่ปรึกษาร่วม _____

5587855520 : MAJOR NANOSCIENCE AND TECHNOLOGY

KEYWORDS: CALCIUM COPPER TITANATE THIN FILM / SOL GEL / METAL OXIDE SEMICONDUCTOR / SMART MATERIAL / GAS SENSOR / CAPACITOR / PREFERENTIAL ORIENTATION / SURFACE AND INTERFACE

SURIYONG PONGPAIBOONKUL: STRUCTURAL AND ELECTRICAL PROPERTIES OF $CaCu_3Ti_4O_{12}$ THIN FILMS AND THEIR APPLICATIONS. ADVISOR: ASSOC. PROF. DR. SATREERAT HODAK, CO-ADVISOR: DR. ANURAT WISITSORAAT, DR. NARONGCHAI BOONYOPAKON, 154 pp.

In this research, the effects of Fe-doping on structural and gas-sensing properties of $CaCu_3Ti_4O_{12}$ (CCTO) thin film prepared by a sol–gel methodwere systematically studied. Sol–gel-derived CCTO thin films with different concentrations of Fe-doping were deposited on alumina substrates by spin-coating technique and Au/Cr interdigitated electrodes were patterned onto the films by photolithography, sputtering and lift-off processes. Characterizations by X-ray diffraction (XRD), atomic force microscopy (AFM), field emission scanning electron microscopy (FESEM), energy dispersive X-ray spectroscopy (EDS), Raman spectroscopy, X-ray photoemission spectroscopy (XPS) confirmed the perovskite CCTO phase with TiO_2 and CuO secondary phases and suggested the substitution of Fe^{3+} ions at Ti^{4+} sites of CCTO structure. From gas-sensing measurements, Fe dopants greatly enhance H_2S response, response time and H_2S selectivity against NH_3, CO, C_2H_2, CH_4, ethanol and NO_2. In particular, 9 wt% ($\sim$3 at%) Fe-doped CCTO sensor exhibited the highest response of $\sim$126 to 10 ppm H_2S, which was more than one order of magnitude higher than that of the undoped CCTO sensor at a low optimum operating temperature of 250 ºC. The roles of Fe-dopant on gas-sensing mechanisms of CCTO sensor were proposed. Furthermore, highly-oriented $CaCu_3Ti_4O_{12}$ (CCTO) thin films have been deposited successfully on $LaAlO_3$(100), $NdGaO_3$(100) and $NdGaO_3$(110) substrates using a sol-gel method. These substrates were chosen in terms of small lattice mismatch between CCTO and the substrate. The X-ray diffraction patterns showed that the CCTO film layers grow with the c-axis perpendicular to the substrate surface. The plane view and cross sectional FE-SEM images showed a smooth and crack-free surface throughout the film with large grains and dense packing. The interface between the CCTO film and the single crystal substrate was sharp. In this experiment, it was shown that the preferred orientation of CCTO thin films can be manipulated by growing on various types of substrates and different substrate orientations without any conducting buffer layers. The correlation between the preferred orientations of the films and their dielectric properties were also reported.

Field of Study: Nanoscience and Technology Student's Signature ⬚⬚⬚⬚⬚⬚⬚⬚⬚⬚

Academic Year: 2015 Advisor's Signature ⬚⬚⬚⬚⬚⬚⬚⬚⬚⬚

Co-Advisor's Signature ⬚⬚⬚⬚⬚⬚⬚⬚⬚⬚

Co-Advisor's Signature ⬚⬚⬚⬚⬚⬚⬚⬚⬚⬚

ACKNOWLEDGEMENTS

CONTENTS

List of Figures

จุฬาลงกรณ์มหาวิทยาลัย
CHULALONGKORN UNIVERSITY

List of Tables

CHAPTER I

INTRODUCTION

1.1 Background and Motivation

CaCu$_3$Ti$_4$O$_{12}$ (CCTO) is a metal-oxide semiconductor (MOS) material with a cubic-phase pseudo perovskite structure (space group Im-3). CCTO has recently been shown to have extraordinarily high dielectric constant on the order of 10^5, 10^4, 10^3 for the single crystal, ceramic, and thin film forms, respectively [1-4]. In addition, CCTO exhibits either p-type or n-type conductivity behavior depending on processing characteristics [5, 6] and shows non-ohmic behavior due to the presence of Schottky potential barriers at its grain boundaries between semiconducting grains [7]. CCTO has been deposited on substrates by various methods including pulsed laser deposition (PLD) [8], metal organic chemical vapor deposition (MOCVD) [9], RF-magnetron sputtering [10], and sol-gel [11]. Various types of transition metals such as Ni, Cr, Eu, FeNb and others has been loaded into CCTO to enhance or adjust its dielectric properties [12-16]. The dielectric properties including dielectric constant, loss tangent and dielectric relaxation of the metal doping Fe-doped CCTO ceramics and films have been studied recently [17, 18]. For instance, it is found that the dielectric constant of CaCu$_3$Ti$_{4-x}$Fe$_x$O$_{12}$ ceramic decreases dramatically from 10^5 to 50 in a frequency range of 1 kHz to 1 MHz as Fe-doping content increases from x = 0 to 0.2 and three relaxation

process occurs [19]. Additionally, CCTO has a wide range in the temperature dependence of dielectric properties between 100 and 600 K at 10 kHz, making it potential as a pyroelectric sensor [20, 21]. Recently, CCTO has been explored as an alternative candidate to conventional metal oxides such as WO_3, SnO_2, ZnO, and In_2O_3 for gas sensing applications. CCTO is [21] relatively few investigated as gas-sensing materials. Firstly, CCTO thin films exhibit effective resistive changes under exposure to O_2 and N_2 [22]. In addition, CCTO film with hollow hemisphere structures (diameter of ~800 nm) prepared through microsphere template patterning and deposited on alumina substrates is shown to have better gas sensitivity than the original thin film form [23]. Furthermore, CCTO has been doped with metal catalysts to improve its gas-sensing properties. However, there has still been only few reports on doped CCTO gas sensors. For example, Mg-doping in CCTO is shown to provide improved selectivity towards water vapor [24]. Iron (Fe) is a useful additive for gas sensing applications due to its high catalytic activity and low cost. It has been employed to enhance the gas sensing performances of several metal oxides including WO_3, SnO_2 and ZnO. Nevertheless, it has never been applied to CCTO for gas-sensing. In this thesis, Fe-doped CCTO thin films are prepared by a sol-gel process with different doping concentration and the effect of Fe doping on gas-sensing properties of CCTO films is systematically investigated towards hydrogen sulfide (H_2S). Recently, many research groups have reported the gas sensing property of several materials toward H_2S. L. Xing and L. Xue with their colleagues fabricated NiO/ZnO nanowire for high and fast H_2S response in the ranging from 1000 to 100 ppm [25]. N. D. Chien et al. prepared SnO_2 thin film sensitized with CuO Island for H2S-sensing enhancements [26]

In addition, reducing size of microelectronic devices in the form of thin films such as capacitors in dynamic random access memory (DRAM) has attracted much interest in the industry and research fields. In recent years, $CaCu_3Ti_4O_{12}$ (CCTO) has been considered to be the first choice in reducing device dimension because of its giant dielectric constant over a wide temperature (100-600K) and frequency range up to 1 MHz [7, 27]. For more details, the dielectric constant of CCTO single crystal and ceramic is on the order of 10^5 and 10^4, respectively whereas that for the film form is on the order of 10^3 -10^4 depending on its crystal structure either polycrystalline or epitaxy [28-30] There has been no ferroelectric lattice distortion observed by either high-resolution X-ray [27] or neutron powder diffraction [31] experiments like found in other ferroelectric or relaxer materials such as $(Ba, Sr)TiO_3$ (BST) [32] and $SrTiO_3$ (STO) [33] Normally the dielectric response of CCTO is related to its microstructure and crystallinity. Several research groups have investigated the synthesis and characterization of CCTO thin films by using different growth techniques including chemical and physical depositions. In the work of Shri Prakash et al., the CCTO thin films deposited on $Pt/Ti/SiO_2/Si$ substrate using radio frequency magnetron sputtering exhibited high dielectric constant of 5000 at 400K in the frequency of 1 kHz [34]. D. Hu et al. synthesized ZnO-doped CCTO thin films grown on Si (100) in order to obtain the high dielectric permittivity and the low dielectric loss in the capacitor devices [35]. J. Wolfman et al. studied a Schottky type barrier at the bottom electrode CCTO thin film capacitor fabrication [36]. However, high quality CCTO thin films could be epitaxially grown on various substrates with or without conducting buffer layers in order to increase the dielectric constant and suppress the dielectric loss [28]. Lin et al. have shown that the epitaxial CCTO thin films grown on $LaAlO_3$ (001) by pulsed laser

deposition reached the dielectric constant of about 10,000 at room temperature with the dielectric loss of 0.05 at 1 MHz [37]. The growth of CCTO thin film with (h00) preferential orientation on $SrTiO_3$ (100) (STO) substrates by using a chemical method was reported [38]. Li et al. have prepared CCTO thin film exhibiting the (h00) preferential orientation on $LaNiO_3$-coated silicon substrate by a sol-gel process [28]. However, there were few reports on the influence of substrate types on the crystal structure and surface morphology of CCTO films and there are fewer dealing with sol-gel preparation. The aim of this work is to study the effects of chosen substrate types on the crystal structure and the morphology of CCTO thin films prepared by a sol-gel method. CCTO bulk ceramic has a cubic structure with a lattice constant of a=7.36 Å (a/2=3.68 Å). Lanthanum aluminate ($LaAlO_3$, LAO) is rhombohedral at room temperature, and undergoes a phase transition to cubic structure at about 500-800 °C. It is also twinned which can be seen by visual inspection. A pseudo cubic lattice parameter for LAO (100) is about 3.79 Å and the lattice mismatch between CCTO film and LAO substrate is 2.5% [39]. Neodymium gallate ($NdGaO_3$, NGO) single crystal substrate is known to be a substrate for the growth of high-T superconducting thin film [40] and perovskite dielectric thin films [41]. NGO has distorted perovskite orthorhombic structure (Pbnm) which may provide better epitaxial phase in CCTO thin film. The lattice parameters for NGO are a=5.44 Å, b=5.50 Å, and c=7.71 Å, with corresponding pseudo-cubic lattice parameters of a^c =3.86 Å, b^c =3.87 and c^c =3.87 Å [JCP Pattern No. 73-2299.]. Thus, the lattice mismatch between CCTO film and NGO substrate is 4.9%. One advantage of utilizing NGO as a substrate is no twining effect and phase change compared with lanthanum aluminate (LAO) during annealing process. Therefore, it is possible for hetero-interface perovskite structures in order for observation the highly-

orientation of CCTO on NGO substrates. Since the giant dielectric constant at room temperature is believed to associate with an internal barrier layer capacitance related to Schottky barriers at the grain boundaries, in this thesis it is worth to systematically study their grains at the surface morphology and cross section as well.

1.2 Scope of this thesis

In this research, the experiment concerning Fe-doped CCTO thin films were prepared by sol-gel process on alumina substrates with different doping concentration and the effect of Fe doping on gas-sensing properties of CCTO films is systematically characterized towards various gases in order for selectivity and sensitivity such as NH_3, CO, C_2H_2, CH_4, H_2S, ethanol and NO_2. The main focus on the gas sensing part in this thesis is the enhancement H_2S-sensing performances with Fe-doping in CCTO thin films prepared by a sol-gel method. Furthermore, highly-oriented $CaCu_3Ti_4O_{12}$ (CCTO) thin films were deposited on different types of single crystal substrates; $LaAlO_3$ (100), $NdGaO_3$ (100) and $NdGaO_3$ (110) substrates using a sol-gel method. These films were fabricated as thin film coplanar capacitors at which I expected that the crystal structures of CCTO thin films can be manipulated by growing on various types of substrates without any conducting buffer layers. The resulting films were characterized for physical and chemical property aspects using several techniques. The X-ray diffraction (XRD), field emission scanning electron microscopy (FE-SEM), and atomic force microscopy (AFM) are utilized to characterize the crystal structure, the cross section, the surface morphology and the roughness of the films. X-ray photoemission spectroscopy (XPS), energy dispersive X-ray spectroscopy (EDX), and

Raman spectroscopy are used to support the evidence of chemical compositions and confirm the crystal structures of resulting CCTO thin films and arising secondary phases in the film under certain growth conditions.

1.3 Overview of this thesis

Chapter II introduces the crystal structure of CCTO with several drawings and the general concept of CCTO properties such as IBLC model, dielectric constant, dielectric loss, the interaction between gas and solid surface.

Chapter III explains the basic principles of characterization techniques utilized for CCTO analysis such as XRD, FESEM, XPS, AFM, and Raman spectroscopy.

Chapter IV is the experimental part for the thin film processing and the device fabrication based on gas sensing and dielectric measurement.

Chapter V is the discussion of the experimental results. For example, thin films grown on different types of substrates will be explained in details and the gas measurement and dielectric properties will be revealed for information in the research.

Chapter VI is the overall conclusion for my dissertation.

CHAPTER II

THEORITICAL BACKGROUND

2.1 Calcium Copper Titanate CaCu$_3$Ti$_4$O$_{12}$ (CCTO)

Figure 2.1 shows the crystal structure of CaCu$_3$Ti$_4$O$_{12}$ (CCTO) illustrating a pseudo cubic perovskite oxide structure of stoichiometric type (A'A"$_3$M$_4$O$_{12}$). All crystal drawings are simulated by Material Studio 6.0 under license of Faculty of Science, Chulalongkorn University and Mathematica 10 student version. Ca^{2+} ion shares the A' site as CaO$_{12}$ (icosahedral coordination, 20 faces) as shown in Figure 2.2. Cu^{2+} ion shares the A" site and is in square-planar coordination with oxygen atoms as the nearest neighbors forming CuO$_4$ as represented in Figure 2.3. The square planar structures for Cu^{2+} bond with four oxygen atoms, and the large Ca^{2+} ions are located in eight corners as well as body centered position. Ti^{4+} ion is at the M site and coordinates with six oxygen ions in a slightly distorted octahedron (TiO$_6$) as displayed in Figure 2.4. In other words, Ti^{4+} ions dwelling in centrosymmetric positions are surrounded by six oxygen atoms as octahedral sites. TiO$_6$ octahedral cages are tilted about 20° with respect to the unit cell axis to accommodate local distortion leading to non-ferroelectricity in CCTO. The bonding distance between Ca-O in CCTO crystals is 2.604 Å which is shorter than 0.116 Å predicted through ionic radii and then it is the

consequence of pushing out to expand the lattice parameter. Ti-O bonding is also under tensions leading to the increasing of polarizability of the crystal structure.
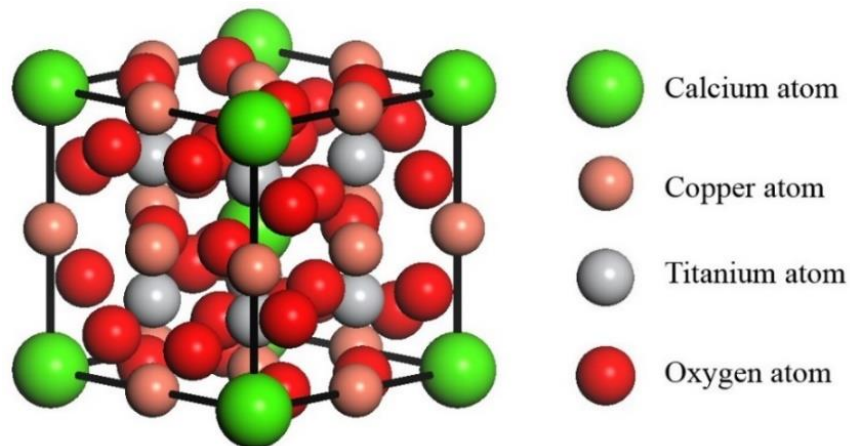
Figure 2.1: The conventional unit cell of $CaCu_3Ti_4O_{12}$ crystals.

CCTO is classified in the Im-3 space group (No. 204) and the lattice constant is approximately 7.391 Å. The discovery of colossal dielectric constant in $CaCu_3Ti_4O_{12}$ (CCTO) has been an interesting topic for material research because CCTO exhibits high permittivity values approaching to approximately 10^5 for single crystals, 10^4 for bulk polycrystalline, and 10^3 for thin films [1-4] with the board range of temperature between 100-600 K without any phase transitions and the frequency independent from 100 Hz to 1 MHz, and CCTO exhibits high loss tangent (0.05-0.1). However, the dielectric constant of CCTO suddenly drops to ≈ 100 below 100 K. These properties made CCTO suitable for use in microelectronic devices in a wide range of temperature and frequency. CCTO also shows the nonlinear I-V characteristic behavior. As known for decades, the ideal capacitor material requires high dielectric constant and low dielectric loss.

<center>(a)   (b)</center>
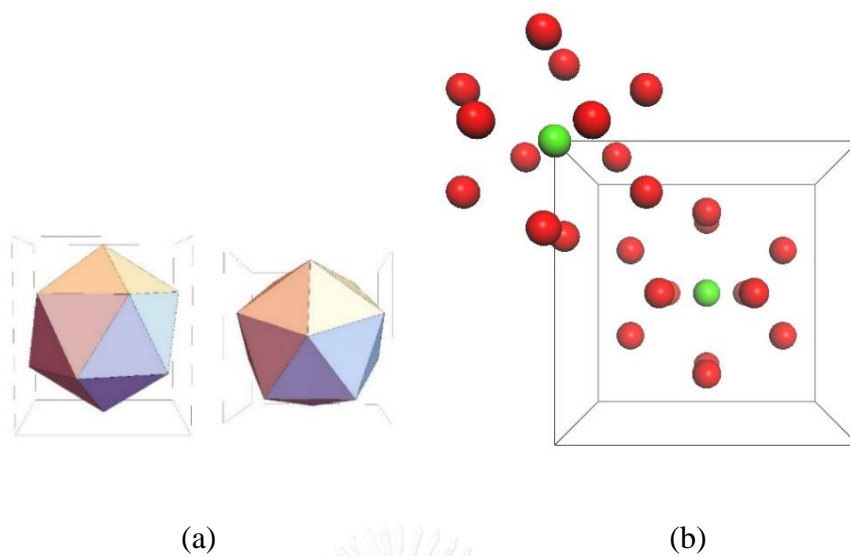
Figure 2.2: The Icosahedron coordination of CaO_{12}. (red atom : O and green atom : Ca)

<center>(a)   (b)</center>
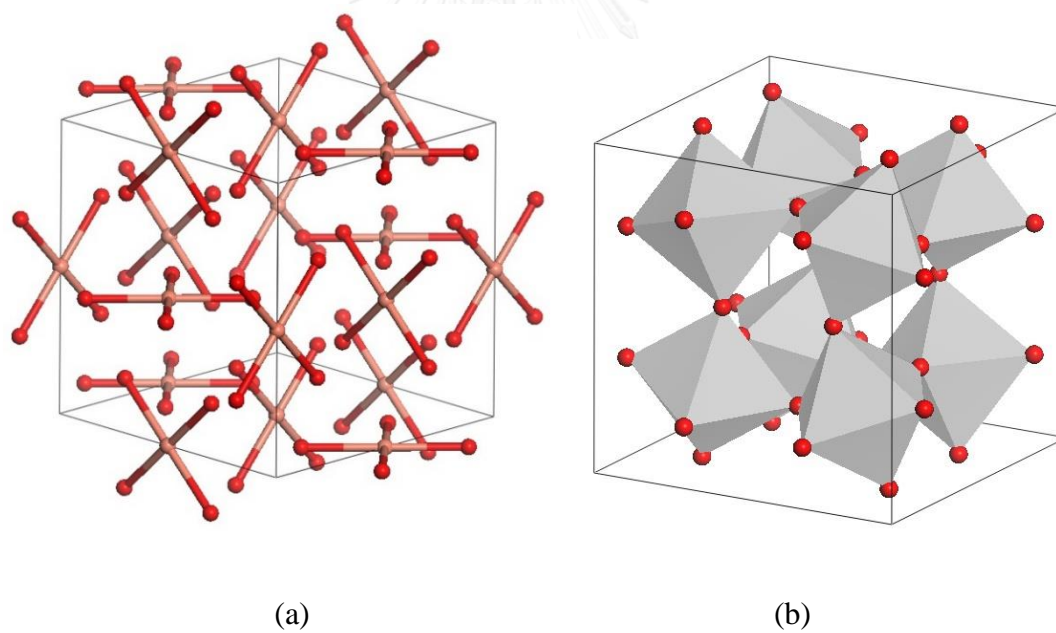
Figure 2.3: (a) The square planar coordination CuO_4 and (b) The octahedral coordination TiO_6. (orange atom : Cu and red atom : O)
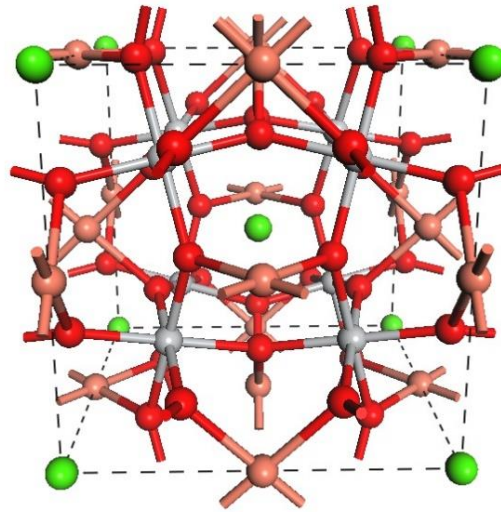
Figure 2.4: The line coordination of $CaCu_3Ti_4O_{12}$ (green atom : Ca, orange atom : Cu, silver atom : Ti, and red atom : O)

2.1.1 The intrinsic properties of CCTO

The intrinsic properties are informing effects of high polarizability and non-ferroelectricity of CCTO crystals under consideration of perfect stoichiometry, no defects, and only single domain crystal of CCTO. For example, the effect arising local dipole moments in crystals cause constrains from tilted TiO_6 octahedral shapes with 141° angle in each connection which is off center for displacement of Ti ions. Meanwhile, the transition to ferroelectric state for CCTO is unable to be occurred because the TiO_6 octahedral tilt is accommodated by Cu^{2+} square planar coordination. The occupying into the crystal site between Ca^{2+} and Ti^{4+} behaves as if they are donors and acceptors, respectively. These causes will make the polarizability increase or decrease if the A' or M sites are replaced with other elements. An intrinsic origin in the form of a ferroelectric relaxation was still defended in 2005 [42]. Others ignored an

intrinsic origin and replaced with an extrinsic one, for example in 2002, Sabramanian and Sleight proposed that the numerous twin boundaries may constitute such barrier layers [31]. In the same year, D. Sinclair et al. concluded from CCTO ceramic data obtained from impedance spectroscopy, CCTO is electrically heterogeneous, composed of semiconducting grains with insulating grain boundaries, and attribute the giant dielectric constant phenomenon to an internal barrier layer capacitance (IBLC) [7]. This IBLC model is reviewed and discussed in detail in the next section.

2.1.2 The extrinsic properties of CCTO

Understanding CCTO mechanisms become convenient, if it is illustrated in term of extrinsic properties such as point, line, planar defects or other imperfections as well as describing in the simple microstructure, morphology, domain boundaries and boundary layers. The Internal Barrier Layer Capacitance (IBLC) is the popular model to be described in the term of extrinsic properties in order to understand the behavior of huge dielectric constant of CCTO, and it can be hence experimentally observed through dielectric measurements.

2.1.2.1 Internal Barrier Layer Capacitance (IBLC) model

The IBLC model is defined as the barrier layer structure with semiconducting areas enclosed by insulating layers and it is established to explain the very large capacitance behavior in both polycrystalline and ceramic of CCTO as demonstrated the model in the However, this IBLC model proved to be correct for the ceramic CCTO case, however, it faced problems when it is used with the single crystals with no grain boundaries. Figure 2.5 (a) illustrates the typical behavior of IBLC model. The grain boundary (gb) and the bulk (b) can describe the idealistic of colossal dielectric where each grain boundary or bulk type contribution is described by one RC circuit element consisting of a resistor and capacitor in parallel as shown in Figure 2.5 (b). The resistors R_1 and R_2 related to the bulk and the gb resistivity (ρ_1 and ρ_2), respectively and the capacitors C_1 and C_2 represent bulk and the gb permittivity (ε_1 and ε_2), respectively [7].

(a)   (b)
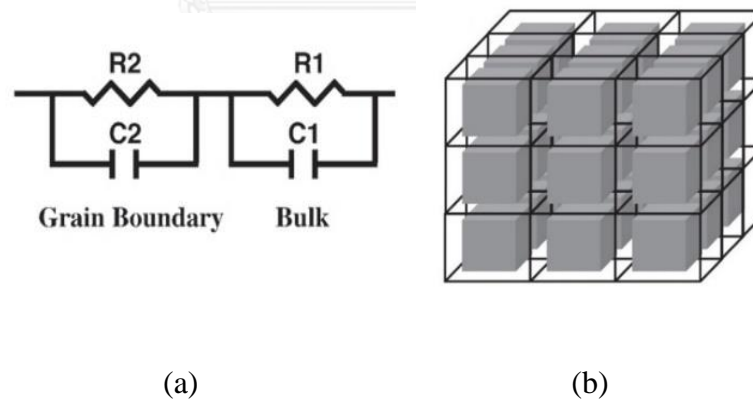
Figure 2.5: Schematic the capacitance circuit and IBLC diagram [7].

According to IBLC model, the colossal dielectric constant ε_r of heterogeneous electro-ceramic material can be revealed as the equation below. ε_{gb} is the dielectric constant of grain boundary, t_g and t_{gb} are the wideness and thickness of grains and grain boundaries respectively. The tiny value of ε_{gb} with the thin thickness of grain boundaries can also affect the giant dielectric constant as extrinsic properties description [43].

$$\varepsilon_r = \varepsilon_{gb} \frac{t_g + t_{gb}}{t_{gb}} \tag{2.1}$$

CCTO grains behave as n-type semiconducting carriers distinguished by inter-granular boundary phases of p-type carriers consisted of CuO. Φ_B is a potential barrier needed for electronic carriers to move through the inter-granular boundaries and its electrons jump from one grain to another. This barrier potential can be changed under an applied voltage in a way that depends on the relative resistances grain (R_g) and grain boundaries (R_{gb}). The two possibilities for consideration are shown from the Figure 2.6 [44].

The two circumstances of model are as follows [44]

$R_{gb} \gg R_g \rightarrow \Delta\Phi_B$ (V) < 0; C (V) < 0; The Schottky Barrier-like behavior

$R_{gb} \sim R_g \rightarrow \Delta\Phi_B$ (V) > 0; C (V) > 0; Metal oxide semiconductor-like (MOS) behavior.
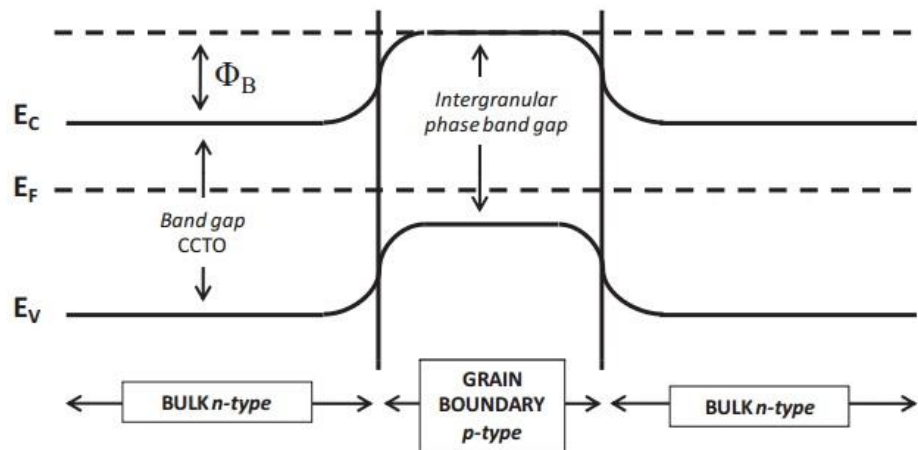
Figure 2.6: The energy band diagram of n-type CCTO grain sizes and p-type CuO intergranular boundary [44].

The first case, it appears when an external electric field is applied and the barrier height decreases ($\Delta\Phi_B$ (V) < 0) because of the carrier accumulation on the semiconducting grain near to the grain boundary. Then, the carriers jump over the grain boundary to the next semiconducting grains. The negative charge transports produce a reduction of the capacitance with the applied electric field. For this phenomenon for IBLC model, grain boundary resistances are very high and the dielectric loss is low because conductive effects are not limited. As shown in Figure 2.7 (a) grain boundary conduction can appear at low frequencies.

The second case, when the barrier height is induced an increase, the capacitance is raised. The charge carriers on both grains and grain boundaries accumulate at either side of the interphase leading to an increasing in the barrier height ($\Delta\Phi_B$ (V) > 0) as shown in Figure 2.7 (b) this should be very useful for sensor material because the sensitivity along grain boundary would be conductive due to small variations on their nature which can response to some certain gases. Therefore, this model supports different new application for CCTO depending on modification of grain boundary structure [44].
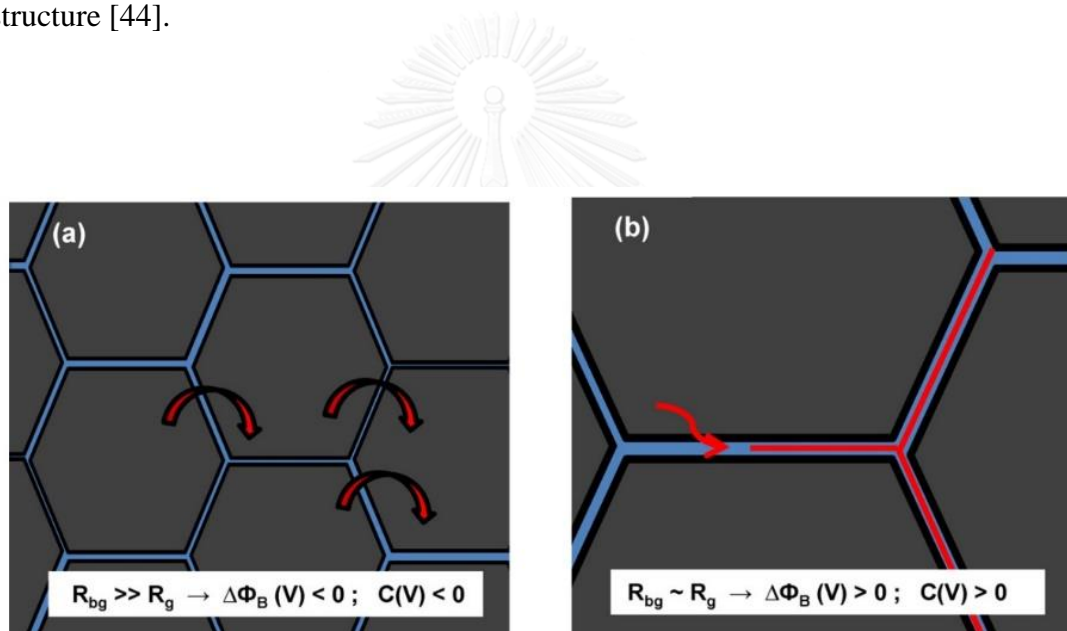
Figure 2.7: The schematic diagrams both of two phenomena arising in microstructure of CCTO [44].

2.2 Polarization in materials (Dielectric response)
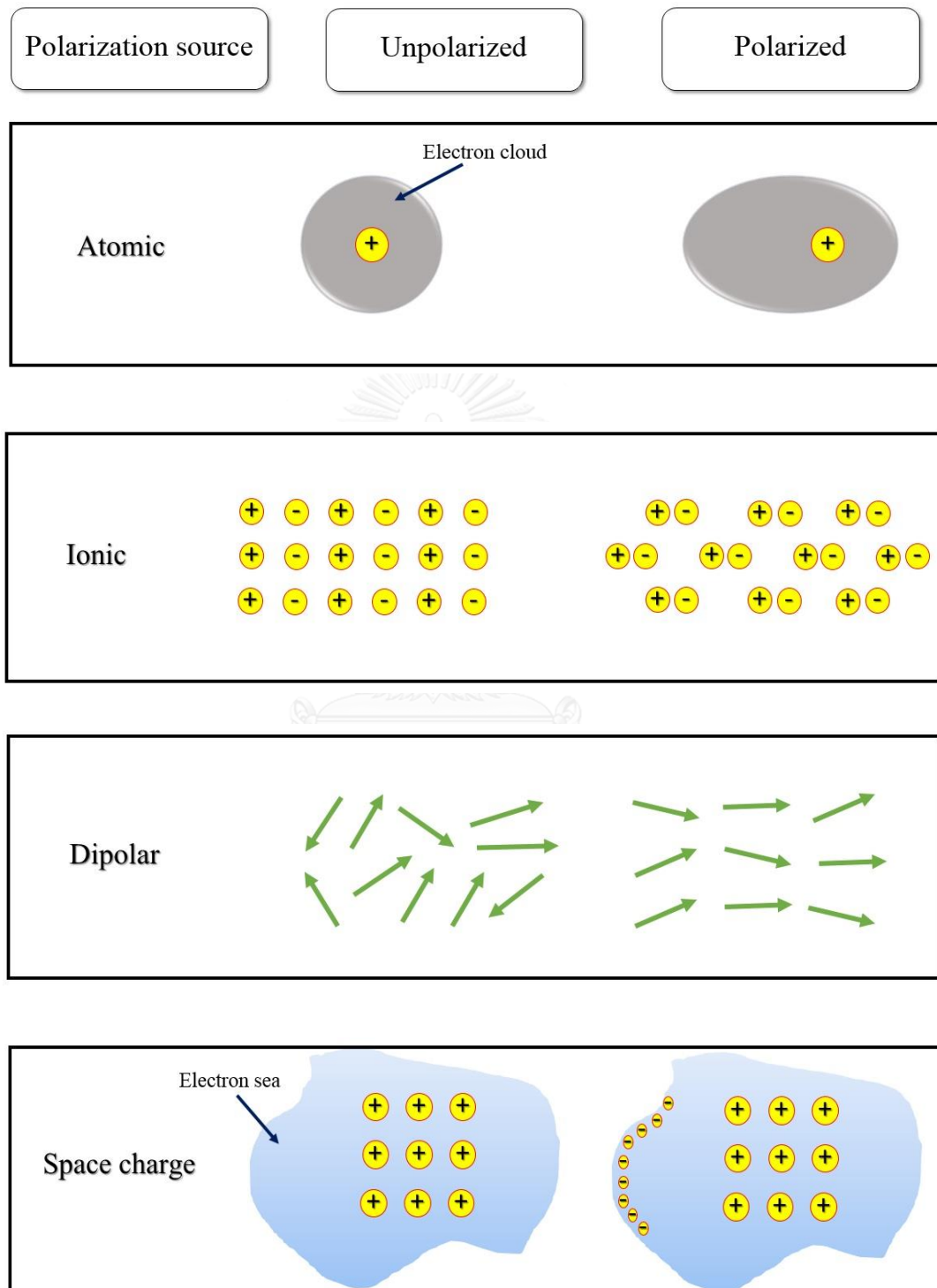
Figure 2.8: Simple schematic of polarization mechanisms [45].

When dielectric materials are under an external electric field, this makes electric charges in solid crystals shift and they become polarized. The summation of electric dipole moment vectors in materials is nonzero. The polarization P is defined as **the dipole moment per unit volume** as shown on the Eq. (2.2) [45].

$$\vec{P} = \frac{1}{V} \sum_n q_n \cdot \vec{r}_n \qquad C/m^2 \qquad (2.2)$$

V = volume of material shapes.

q_n = charges

$\vec{r}_n$ = displacement between positive and negative charges
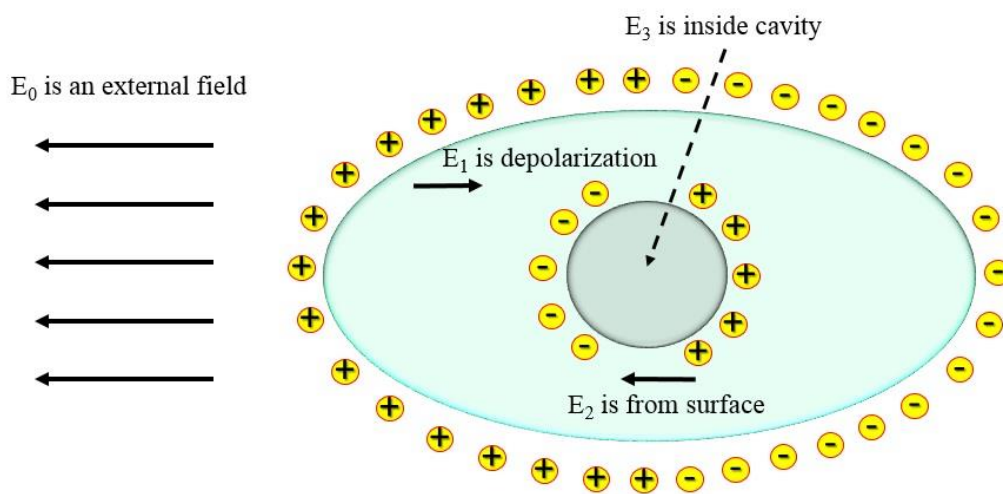
Figure 2.9: The Schematic of dielectric material under external electric field and local field [45].

2.2.1 Local electric field on dielectric materials

The electric field interacting with dielectric materials is known as the polarizing field or the local field, E_{local}. The local field acting on the reference dipoles is given by the summation below [45].

$$\vec{E}_{local} = \vec{E}_0 + \vec{E}_1 + \vec{E}_2 + \vec{E}_3 \qquad (2.3)$$

The Gauss's law of electrostatic

$$\vec{\nabla} \cdot \vec{D} = \rho \qquad (2.4)$$

The displacement vector D in vacuum is given by

$$\vec{D} = \varepsilon_0 \vec{E}_0 \qquad (2.5)$$

While the dielectric material is applied by external electric field E_0, then the displacement vector is given by

$$\vec{D} = \varepsilon_0 \vec{E} + \vec{P} \qquad (2.6)$$

Substituted the Eq. (2.5) into (2.6)

$$\varepsilon_0 \vec{E}_0 = \varepsilon_0 \vec{E} + \vec{P} \qquad (2.7)$$

Then, external applied electric field, E_0

$$\vec{E}_0 = \vec{E} + \frac{\vec{P}}{\varepsilon_0} \qquad (2.8)$$

Depolarization field, E_1

E_1 is the polarizing charges lying on the external surface of dielectric materials.

$$\vec{E}_1 = -\frac{N\vec{P}}{\varepsilon_0} \tag{2.9}$$

As seen from the equation, the parameter N is called as depolarization factor. N depends on the geometric shapes. For the slab capacitor $N = 1$.

Lorentz cavity field, E_2

E_2 is the polarization charges lying on the surface of cavity.

$$\vec{E}_2 = \frac{\vec{P}}{3\varepsilon_0} \tag{2.10}$$

Field of dipoles inside cavity, E_3

E_3 is the other dipoles lying within the Lorentz cavity.

$E_3 = 0$ is for the case of the symmetric structure like cubic structure, while $E_3 \neq 0$ is for other crystal structures such as monoclinic, triclinic, hexagonal, etc.

$$\vec{E}_{local} = \left(\vec{E} + \frac{\vec{P}}{\varepsilon_0}\right) - \frac{\vec{P}}{\varepsilon_0} + \frac{\vec{P}}{3\varepsilon_0} \tag{2.11}$$

The Lorentz relation is shown at (2.12).

$$\vec{E}_{local} = \left(\vec{E} + \frac{\vec{P}}{3\varepsilon_0}\right) \tag{2.12}$$

2.2.3 Dielectric constant

The dielectric constant or the permittivity in material is under the measureable effect of Coulombic interaction between positive and negative charges. The permittivity of the material is defined as the ratio of the electric displacement D to the electric field intensity E.

$$\varepsilon = \frac{\overline{D}}{\overline{E}} = \varepsilon_r \varepsilon_0 \qquad (2.13)$$

ε_r is the relative permittivity of the medium (dimensionless) or so called the dielectric constant

ε_0 is the permittivity of free space (8.85×10^{-12} C^2/N·m^2)
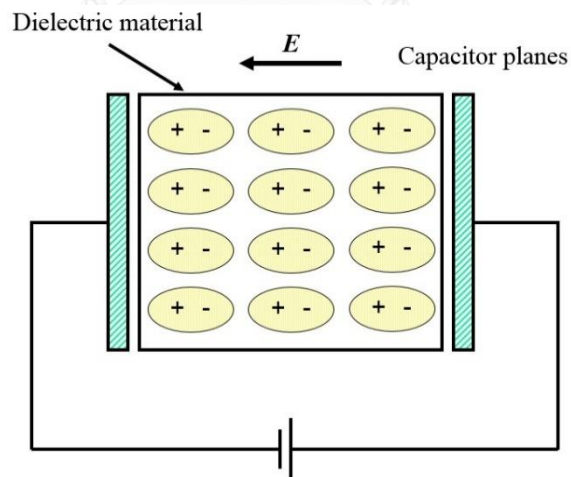
Figure 2.10: Simple diagram of capacitor in one dimension.

As seen from the Figure 2.10, the field generated by the charges is E_0 which can be found out by measuring the potential difference V_0 between two plates of capacitor with the distance L between the plates by using the relation as below [45].

$$E_0 = \frac{V_0}{L} \tag{2.14}$$

The applied electric field can polarize any dielectric medium, the relation between the applied electric field E, the potential difference V across the plates separated by a distance L can be written as:

$$E = \frac{V}{L} \tag{2.15}$$

The relation of ε_r in terms of applied electric field E, the potential difference V and the capacitance C, can be shown as:

$$\varepsilon_r = \frac{E_0}{E} = \frac{V_0}{V} = \frac{C}{C_0} \tag{2.16}$$

The very well-known parallel plates of capacitor formula is defined as:

$$Q = CV \tag{2.17}$$

$$\vec{P} = (C - C_0)V = (\varepsilon - \varepsilon_0)\vec{E} \tag{2.18}$$

$$\vec{P} = (\varepsilon_r - 1)\varepsilon_0\vec{E} \tag{2.19}$$

$$\varepsilon_r = 1 + \frac{\vec{P}}{\varepsilon_0\vec{E}} = 1 + \chi_e \tag{2.20}$$

The term $\chi_e = \frac{\vec{P}}{\varepsilon_0\vec{E}}$ in (2.20) is called the electric susceptibility.

The electric susceptibility is defined as the dependence of electric field on the materials with external parameters such as frequency, pressure, and temperature. For parallel-plates as seen from the Figure 2.9, it is defined as

$$C = \varepsilon \frac{A}{d} = \varepsilon_r \varepsilon_0 \frac{A}{d} \tag{2.21}$$

It is obviously the capacitance depends on the dielectric constants which are characteristic in each type of material, areas of plates which relied on geometrical shapes, and distance between plates [45].

2.2.4 Electronic polarizability

The total polarizability normally can be divided into four main parts [45].

1. The electronic contribution is due to the displacement of the electron relative to a nucleus.

2. The ionic contribution occurs when the charged ions in both negative and positive charges to be separated from equilibrium points.

3. The dipolar polarizability is a cause of molecules with a permanent electric dipole moment which can change orientation in an applied electric field.

4. The space charge region is a result of polarized charges accumulating on the surface and between interfaces.

$|{\sim}10^9 \text{ Hz}|$ $|{\sim}10^{12} \text{ Hz}|$ Ultraviolet

Space charge

Dipolar

Ionic

Electronic
(atomic)

Total Polarizability
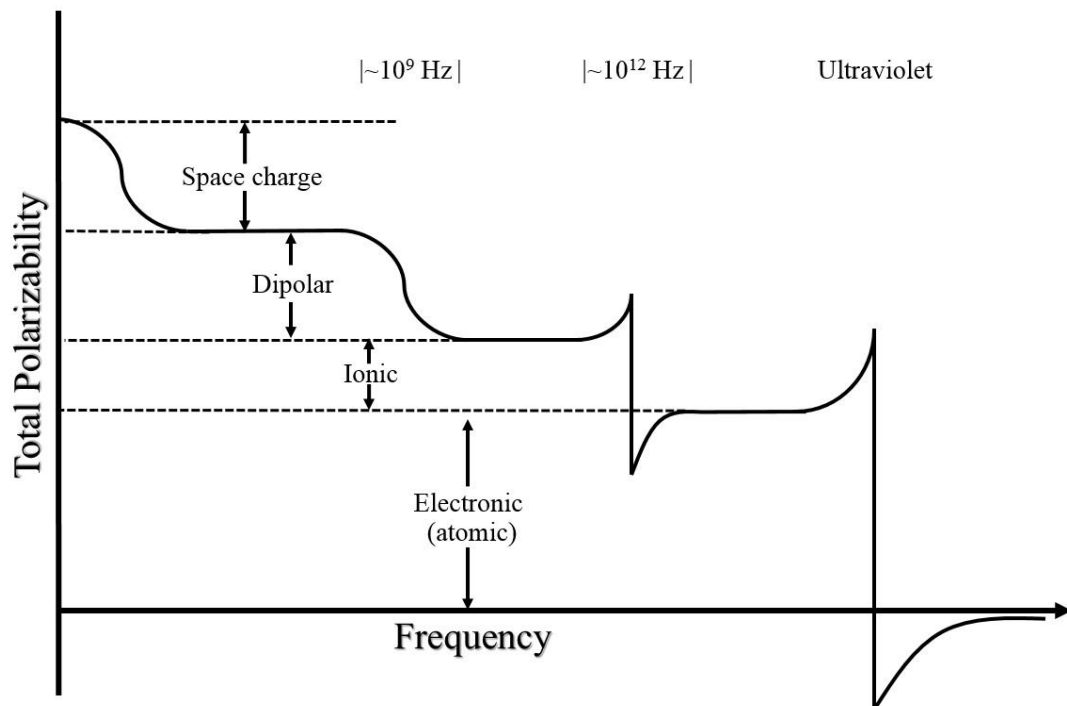
Frequency

Figure 2.11: Frequency dependence of several contribution to the polarizability [45].

2.2.5 The dielectric loss tangent

Dielectric loss quantifies the inherent dissipation of electromagnetic energy for a dielectric material, e.g. heat. This effect does not depend on the geometry of capacitors. Basically, the dielectric loss is expressed as the loss tangent (the dissipation factor). As shown in the Figure (2.12), the simple circuit for a capacitor is applied by voltage with alternating current (AC).

$$V = V_0 e^{i\omega t} \tag{2.22}$$

The alternating current through the capacitor is as from (2.23).

$$\frac{dQ}{dt} = I = C\frac{dV}{dt} \tag{2.23}$$

$$I = C(V_0 e^{i\omega t})i\omega = i\omega CV \tag{2.24}$$

From the formula for the parallel plates capacitor with dielectric material or without any dielectric material, $C = \frac{\varepsilon_r \varepsilon_0}{d}A$ or $C_0 = \frac{\varepsilon_0}{d}A$, the dielectric constant can be separated to the real and the imaginary parts.

$$\varepsilon_r = \varepsilon_r' - i\varepsilon_r'' \tag{2.25}$$

Substituted (2.25) into (2.24)

$$I = I_c + I_L \tag{2.26}$$

I_c is the charging current or out of phase component and I_L is the loss current or in-phase current component.

$$I = i\omega\varepsilon_r' C_0 V + \omega\varepsilon_r'' C_0 V \tag{2.27}$$

$$\tan\delta = \frac{\varepsilon_r''}{\varepsilon_r'} \quad \text{and/or} \quad \delta = \tan^{-1}\left(\frac{\varepsilon_r''}{\varepsilon_r'}\right) \tag{2.28}$$

The dielectric loss can be parameterized in terms of either the loss angle δ or the corresponding loss tangent or so called as tan (δ) [45].

Capacitor

$I_c = \omega\varepsilon_r' C_0 V$

I

δ

$90-\delta$

$I_L = \omega\varepsilon_r'' C_0 V$

V

(a)   (b)
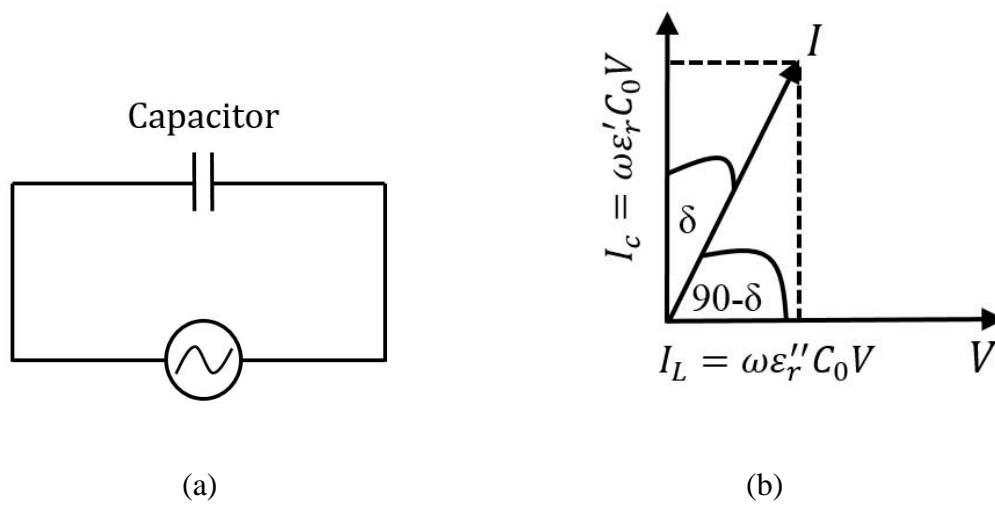
Figure 2.12: (a) A capacitor with AC circuit and (b) Phasor diagram of a capacitor filled with dielectric material.

2.3 Metal oxide gas sensor

A chemical gas sensor is a kind of smart electronic device that interacts with gas phase and it then transforms to a signal. In the modern chemical gas sensor it is considered as transducers to be able to convert chemical reaction in any form such as electrical, optical, and mechanical to measureable signal information. In order for chemical sensing application to response for the gas target, the metal oxide compounds material must be selective for specific type of gas detection. The interaction between gas and metal catalytic leads to the change in electrical properties causing the change in sensor signal. Therefore, understanding chemical reactions and conductance mechanisms is the total significance of a metal oxide chemical gas sensor [46].

2.3.1 The mechanisms of gas sensor

Currently, the ionosorption and reduction-reoxidation mechanisms have become two main different models in order to describe the performance of metal oxide based gas sensing devices. The ionosorption model focus consideration only on space-charge effects for the result of electric surface potential from ionosorption of gas molecules, while the reduction-reoxidation model interprets the sensing phenomenon through oxygen vacancies associating the diffusion of oxygen and oxygen vacancies between bulk inside and surface of sensing materials [46].

2.3.1.1 The Oxygen ionosorption mechanism

Oxygen has a domination on the electrical conductivity and work function of semiconductive materials. As a result of oxygen influence on metal oxide surface, it leads to a decrease in the concentration of conduction electron density and it also increase in the work function. The magnitude of change in electrical properties depends on the temperature and types of metal oxide.

$$O_2(\text{gas}) \leftrightarrow O_2(\text{ads})$$

$$O_2(\text{ads}) + e^-\,(\text{Conduction Band}) \leftrightarrow O_2^-(\text{ads})$$

$$O_2^-(\text{ads}) + e^-\,(\text{Conduction Band}) \leftrightarrow O_2^{-2}(\text{ads})$$

$$O_2^{-2}(\text{ads}) \leftrightarrow 2O^-(\text{ads})$$

$$O^-(\text{ads}) + e^-\,(\text{Conduction Band}) \leftrightarrow O^{-2}(\text{ads})$$
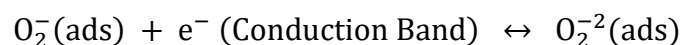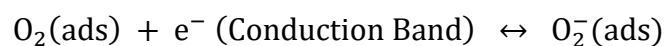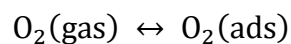
The phenomenological reaction between oxygen ionosorption and on n-type carriers are the cause of ionosorbed oxygen species formed due to the transfer of conduction electrons from semiconductor and they can be considered as free oxygen ions because of electrostatic stabilization on the surface. The ionized oxygen in each specie (O_2^-, O^-, O^{-2}) depends on temperature. At low temperature between 150 and 200 °C, adsorbed oxygen molecules receive one negative charge as shown O_2^-(ads). At high temperature between 200 and 400 °C or higher, it is considered as dissociative atoms as seen O^-(ads) and O^{-2}(ads) ions. Otherwise, neutral oxygen species as physisorbed oxygen do not play any role in gas sensor [46].

2.3.1.2 Oxygen-Vacancy model

This model illustrates the behavior on oxygen vacancies on the surface, which are considered to be dominators on the role of chemi-resistive behavior. The n-type metal oxide semiconductor whose oxygen vacancies act as electron donors. The reaction between gases and oxygen control the surface conductivity and overall sensing behavior. However, the oxygen-vacancy mechanisms depend on type of gases and metal-oxide semiconductor.

$$\frac{1}{2}O_2 + V_o^{\bullet\bullet} + 2e^- \leftrightarrow O_o$$
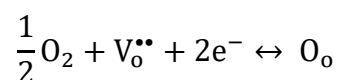
2.3.2 Band bending between gas phase and MOS surface

The adsorbed oxygen molecule on the metal oxide surface can trap electron from the conduction band. As a result, both adsorbed oxygen and surface itself become negative compared to bulk inside, and this can induce a space charge between the interior of the metal oxide and its surface. The negative surface charge is compensated by a space charge layer from the bulk. The positive space-charge region which is reduced electron densities around there is called an electron-depleted layer. As a result, the conduction band bends upward for n-type carrier concentration [46].
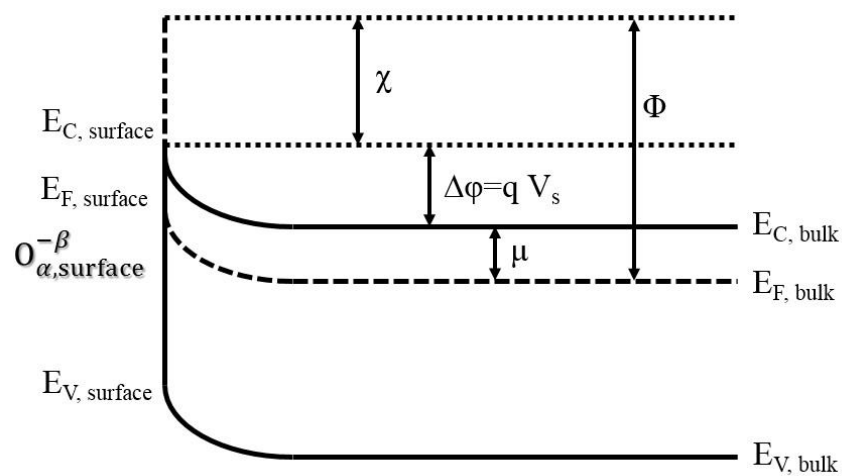
Figure 2.13: The simple band bending diagram of n-type metal oxide illustrates the influence of adsorption on surface conductivity [46].

$$\Delta\varphi = qV_s = q\ (E_{C,\ surface} - E_{C,\ bulk}) \qquad (2.29)$$

$$\Phi = (E_C - E_F)_{\ bulk} + qV_s + \chi \qquad (2.30)$$

$O^{-\beta}_{\alpha,\ surface}$ is a chemisorbed oxygen species ($\alpha = 1$ and 2 for atomic and molecular form respectively, and $\beta = 1$ and 2 for singly and doubly ionized form of oxygen respectively. χ is electron affinity, μ is electrochemical potential, Φ is the work function, $\Delta\varphi = qV_s$ is ionosorption of work function. $E_{C,\ surface}$ $E_{V,\ surface}$ and $E_{F,\ surface}$ are conductance valance and Fermi band edge, respectively [46].

2.3.3 Working principle of gas sensor

While the thermal oxidation is activated to sensing materials, the adsorbed oxygen species behave as electron acceptors on the surface. The electrons are removed from the conducting band E_C because they are trapped by acceptor adsorbate at the surface which lead to electron-depleted region behind. Therefore, the depth of positively-charged space charge layer Λ_{air} is enlarged due to negative surface potential. In addition, the depth of the space-charge layer associates to the Debye-length (L_D) depending on the temperature at a particular donor concentration [46].

$$L_D = \sqrt{\frac{\varepsilon_0 \varepsilon k_B T}{e^2 n_d}} \qquad (2.31)$$

In the polycrystalline structure the electrical conductivity appear along percolation paths by means of grain to grain contacts of micro or nanoparticles. As a consequence of the increased potential barriers at the grain boundaries as called Schottky barriers involved directly to the thermodynamic equilibrium of the oxygen adsorption and desorption reactions. This phenomenon affects an increase in resistance. The Maxwell-Boltzmann distribution describes the number of electrons which succeed in passing through the potential barrier, the conductance G of the sensing layer is shown by Eq. (2.32).

$$G \approx \exp(\frac{-eV_s}{k_BT}) \qquad (2.32)$$

2.3.4 Particle sizes

The mechanism controlling the conductivity change and its magnitude depends on the ratio between grain size (D) and Debye screening length (Λ). In the case of large grains (D > 2Λ), the sensitivity or rather the conductivity is nearly independent of the grain size and mostly dominated by the bulk conductivity. In the case of small grains (D $\leq$ 2Λ) the whole crystallite is depleted, the conduction channels vanish and the conductivity becomes grain size controlled.

As illustrated in both Figure 2.14 and 2.15, when oxygen gases adsorb the surface, oxygen molecules separate to atoms and it attaches one electron in each from the conduction band. This leads to the increase potential barriers between grain boundaries. Meanwhile CO removes one oxygen from the surface of the lattice to form better stable CO_2, then oxygen vacancy is produced. The oxygen vacancy becomes

ionized and it turns the electron back to conduction band. Additionally, the small grain sizes from the Figures 2.16 and 2.17, the crystalline grains control the conductance. When oxygen gases adsorb on the surface and separation to oxygen atom, the electrons from conduction band surface are also trapped by oxygen atom. As a consequence, the conduction band shifts upward far from Fermi level. In contrast, when the small grains interact with reducing gas on the surface, the conduction band moves near Fermi level [46].
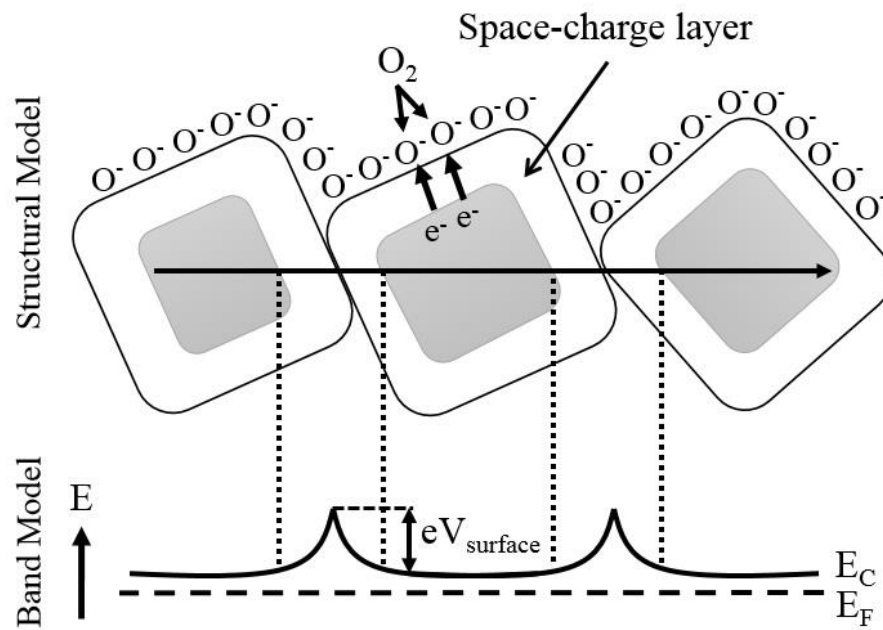
Figure 2.14: The mechanism of oxidizing gas on n-type carrier [46].
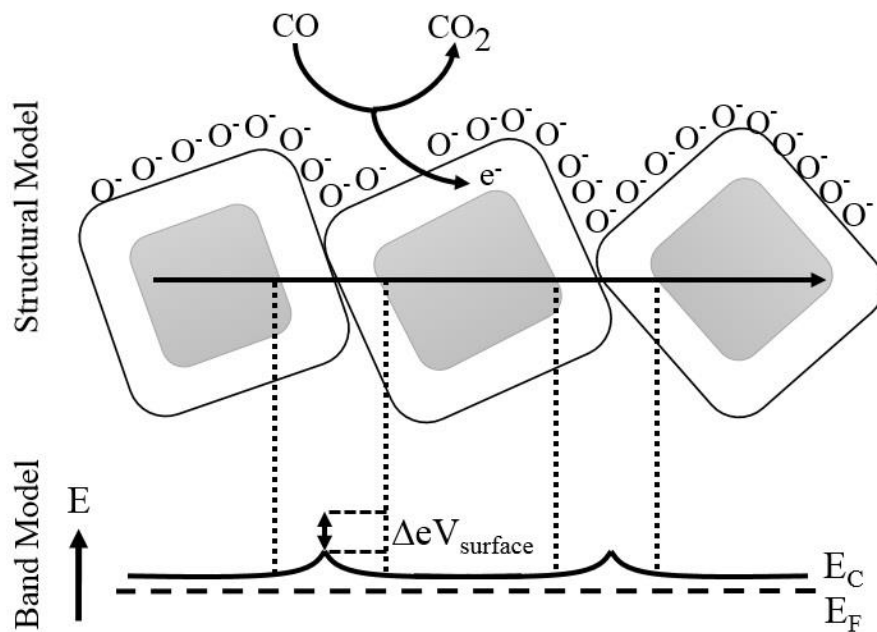
Figure 2.15: The mechanism of reducing gas on n-type carrier surface [46].
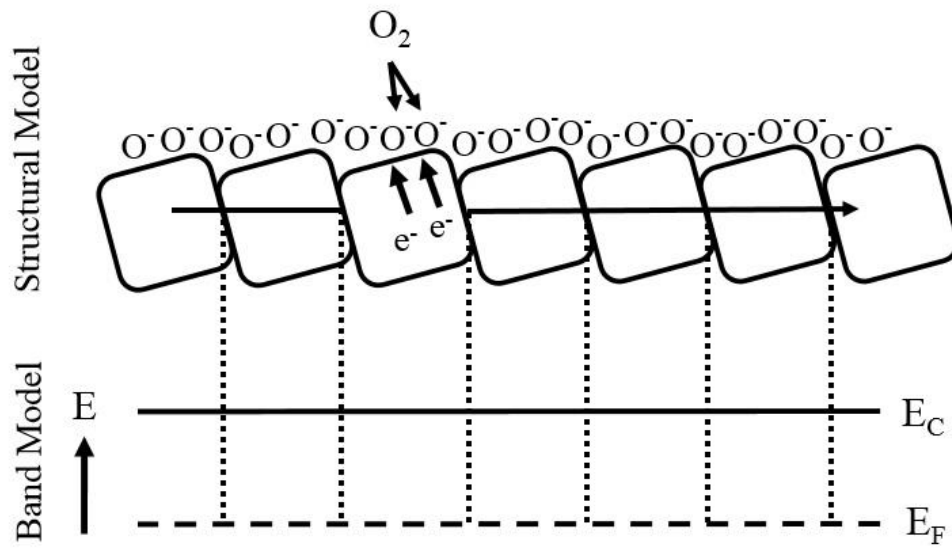
Figure 2.16: The mechanism of reducing gas on n-type carrier surface [46].
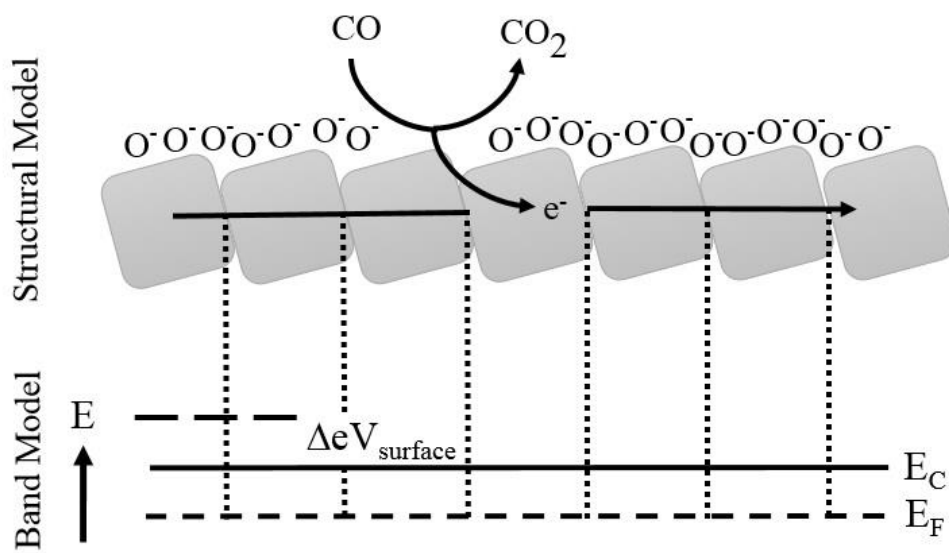
Figure 2.17: The mechanism of reducing gas on n-type carrier surface [46].

2.3.5 Reducing acid: Hydrogen sulfide (H_2S)

There are two factors on the interaction between H_2S and metal oxide surface.

1. H_2S is a strong reducing agent with the ionization potential by 4.10 eV.

2. The heterolytic cleavage on the bonding between Sulfur and hydrogen is quite easy through the formation of new donor-acceptor bond.

$$M^{n+}-O^{2-} \xrightarrow{H_2S} \begin{bmatrix} H \\ | \\ S \end{bmatrix}^{-} + \begin{matrix} H^+ \\ | \\ O^{2-} \end{matrix} \quad (a)$$
$$\begin{matrix} | \\ M^{n+} \end{matrix}$$

$$M^{n+}-O^{2-} \xrightarrow{H_2S} \overset{HOH}{-M-S^{2-}} \quad (b)$$

$$
\begin{matrix}
H & & & H \\
| & & & | \\
O\cdots H \quad H & & & O\cdots H \quad H \\
| \quad \diagdown S \diagup & \longrightarrow & | \quad \vdots \\
M-[\,]- O^{2-} & & M-[S_x] \quad O^{2-}
\end{matrix}
\quad (c)
$$
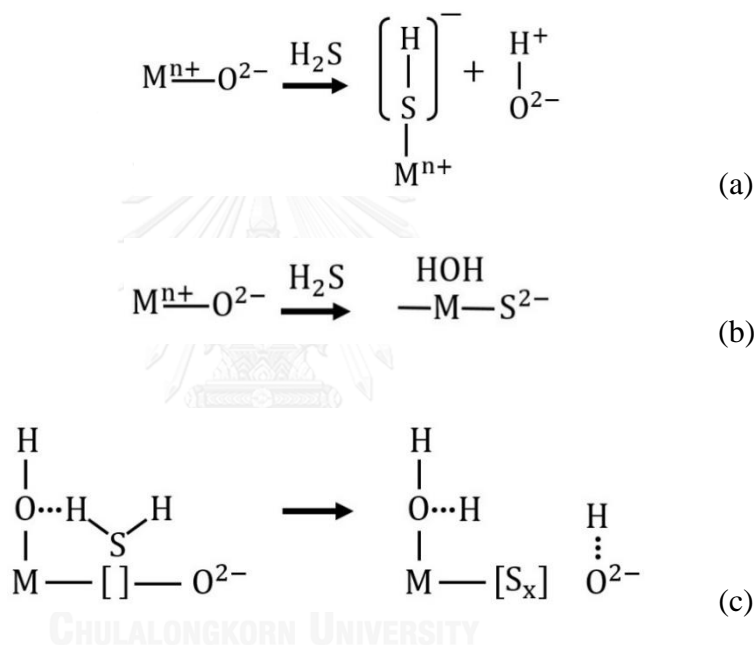
Figure 2.18: The possibility reactions of H_2S gas sensing on metal oxide.

As a result of inter-action with hydrogen sulfide the following changes are found at the oxide surfaces including formation of sulfides, partial blocking of Lewis acid site, reduction of metal cation with variable valences, oxidation of sulfur and increasing acidity of the surface through formation of SO_x groups [46].

CHAPTER III

CHARACTERIZATION TECHNIQUES

In this chapter, the techniques used to characterize the CCTO films are briefly explained. As known, microscopy and spectrocopy techniqures are crucial keys for material research in order to expore the preperties of interesting materials. X-ray difractrometry (XRD) was used to examine the crystal structure as well as the preferential orientation of the films including the secondary phases or impurity phases in the films. Field emission scanning electron microscope (FESEM) equipped with energy dispersive X-ray spectroscopy (EDS) and atomic force microscope (AFM) used to investigate the surface morphology, cross-section and grain size will be described in this chapter. X-ray photoemission spectroscopy (XPS) and Raman spectroscopy used to obtain the information of the chemical analysis of the films will be described briefly as well.

3.1 X-ray diffraction (XRD)

X-ray is a type of electromagnetic wave with energy in the range of 200 eV - 1 MeV and its wavelength is in the range approximately between 0.5 - 120 Å. Due to the

short wave length of X-rays comparable with the size of distance between atoms which are the range of 0.5 - 2.5 Å, thus it is able to be applied for crystal structure measurement with diffraction technique. X-ray diffraction is very useful for crystal analysis in various forms of materials such as powders, thin films, composites and alloy materials, nanostructures, liquid crystals and etc.

3.1.1 The Bragg's Law

When the incident X-ray beam shines to the parallel lattice planes separating by d spacing, the path difference of two rays occurring from adjacent planes is 2d sin θ, where the θ angle is measured from the horizontal plane to the direction of the incident beam. Only constructive interference of reflected X-ray from the lattice planes can be detected from X-ray detectors when the path difference is an integral number n of wavelengths λ and the reflection can occur for λ ≤ 2d. Generally, there are many types of metal target which can generate X-ray wavelength. Copper and molybdenum are common targets used in the X-ray tube. Normally, other wavelengths having small intensity of X-ray beam are filtered out to be monochromatic wavelength, only K-α wavelength is left to probe the samples. The Bragg's law can be defined as below [47].

$$2d_{hkl} \sin \theta = n\lambda \qquad\qquad (3.1)$$
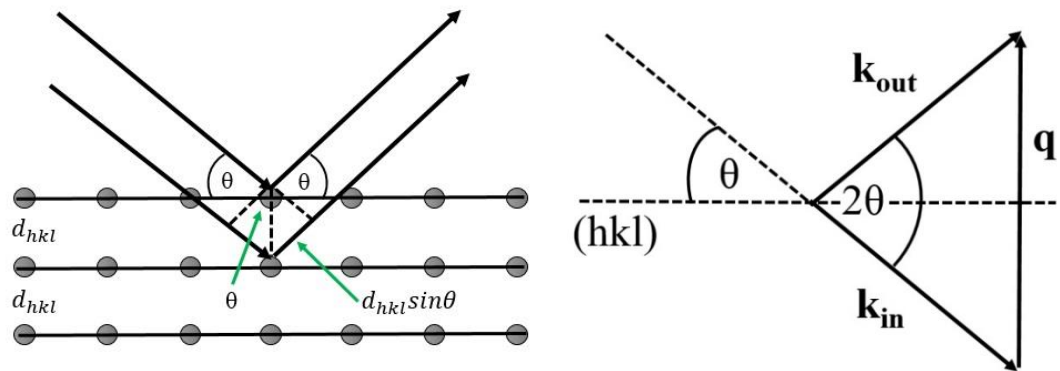
Figure 3.1: The Bragg's law and the scattering vector or reciprocal vectors [47].

When the X-ray interacts with atoms in crystals, it induces harmonic oscillations of the shell electrons of atoms. With the emission of X-ray as the elastic process, the scattering wave remains the same frequency in both of incident and outgoing wave vectors as shown below the Eq. (3.2).

$$|\vec{k}_{in}| = |\vec{k}_{out}| = |\vec{k}| = \frac{2\pi}{\lambda} \qquad (3.2)$$

The scattering vector q can also defined as reciprocal vector

$$q = \vec{G} = \vec{k}_{out} - \vec{k}_{in} \qquad (3.3)$$

XRD experiments were carried out in a diffractometer (Bruker D8 Discover) equipped with a high-speed VANTEC detector and a Cu K1$_\alpha$ X-ray source (λ = 0.15406 nm, 40 kV, 40 mA). The signals were collected with a resolution of 0.02°/step, a scanning speed of 3°/min and a 2 range of 20°-80°.

3.1.1.2 The Reciprocal lattices

The reciprocal lattice vector [47] is perpendicular to the lattice planes with miller indices (hkl) and the distance d_{hkl} between two such adjacent planes is given by

$$d_{hkl} = \frac{2\pi}{|G_{hkl}|} \tag{3.4}$$

$$\vec{G} = h\vec{b}_1 + k\vec{b}_2 + l\vec{b}_3 \qquad h, k, l \text{ interger} \tag{3.5}$$

$$\vec{b}_1 = 2\pi \frac{\vec{a}_2 \times \vec{a}_3}{\vec{a}_1 \cdot (\vec{a}_2 \times \vec{a}_3)} \quad \vec{b}_2 = 2\pi \frac{\vec{a}_3 \times \vec{a}_1}{\vec{a}_2 \cdot (\vec{a}_3 \times \vec{a}_1)} \quad \vec{b}_3 = 2\pi \frac{\vec{a}_1 \times \vec{a}_2}{\vec{a}_1 \cdot (\vec{a}_1 \times \vec{a}_2)} \tag{3.6}$$

The vector b_i and their linear combinations are called reciprocal lattice vectors in Fourier space. The inter-planar spacing (d_{hkl}) has a relationship of the Miller indices and lattice constants. For CCTO structures, it represents the cubic phase and NGO structure displays the orthorhombic phase. Meanwhile, LAO can exhibit two phases of thermal variations which are rhombohedral structure at room temperature and cubic phase at temperature higher than 420 °C. The relationship between d-spacing (d_{hkl}) and the lattice constant (a,b,c) for each type of phases is shown in equations below.

$$\frac{1}{d_{hkl}^2} = \frac{h^2 + k^2 + l^2}{a^2} \qquad\qquad \text{Cubic phase}$$

$$\frac{1}{d_{hkl}^2} = \frac{h^2}{a^2} + \frac{k^2}{b^2} + \frac{l^2}{c^2} \qquad\qquad \text{Orthorhombic phase}$$

$$\frac{1}{d_{hkl}^2} = \frac{[(h^2 + k^2 + l^2)\sin^2\alpha + 2(hk + kl + lh)(\cos^2\alpha - \cos\alpha)]}{(1 + 2\cos 3\alpha - 3\cos^2\alpha)a^2} \qquad \text{Rhombohedral phase}$$

3.2 X-ray Photoelectron Spectroscopy (XPS)

X-ray photoelectron spectroscopy (XPS) reveals information on the elemental composition and speciation of matters by evaluating the electronic structure of atoms and ions dwelling with in the surface region of the samples being analyzed. Since the Photoelectron spectroscopy is the electron-photon interaction which an electron initially occupying to energy states of an atom or ion is ejected by a photon. If the photo energy is sufficient, it will result in the electron emission from the atom or ion leading to the ionization. The kinetic energy (K.E.) distribution of the emitted photoelectrons (i.e. the number of emitted photoelectrons as a function of their kinetic energy) can be measured using any appropriate electron energy analyzer and a photoelectron spectrum can thus be recorded. This is very helpful because the quantization of energy is a function of the electron binding energy (B.E) in elements and environmental specific where the binding energy of the electron refers to the difference in energy between the ionized and neutral atoms. In fact, the binding energies of energy levels in solids are conventionally measured with respect to the Fermi-level of the solid, no the vacuum level involving a small correction (the work function, $\emptyset$) to the equation as seen in Eq. (3.7). Figure 3.2 shows the band structure related to photoelectron emissions [48].
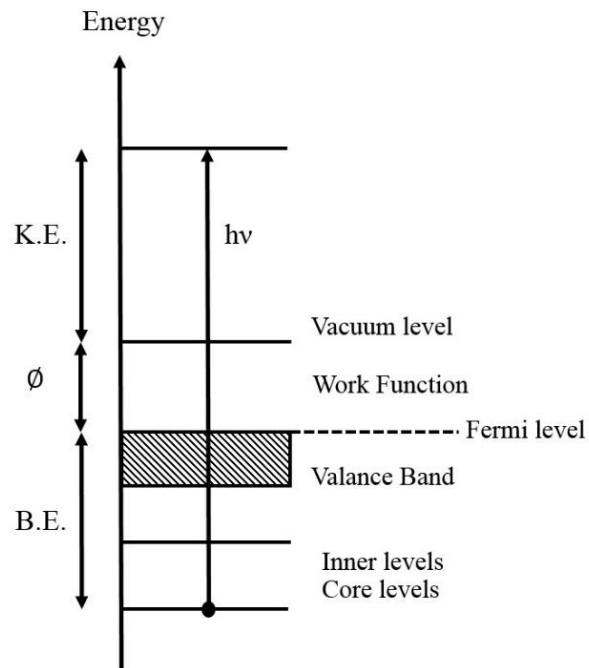
Figure 3.2: The band structure related to photoelectron emissions.

$$\text{K. E.} = \text{E}_{\text{photon}} - \emptyset - \text{B. E.} \qquad (3.7)$$

$\emptyset$ is the work function of spectrometer

E_{photon} is the photon energy

B. E. is the binding energy of electrons

K. E. is the kinetic energy of emitted electrons

Sometimes, to simplify BE is taken to be a direct measure of the energy required to just remove the electron concerned from its initial level to the vacuum level and the KE of the photoelectron is again given by :

$$K.E. = h\nu - B.E. \tag{3.8}$$

The chemical state and elemental composition of sol–gel films at room temperature were analyzed by XPS (AXIS Ultra DL) using a monochromatic Al K_α X-ray excitation source.

3.2.1 Basic spectral interpretation

The atomic number indicates the number of protons within the core of an atom. There are two main phenomena for XPS analysis. The initial state effects appear due to ground state bonding and spin orbit splitting and final state effects can be a consequence of photoelectron-induced polarization and rearrangement [48].

3.2.1.1 Initial state effect

Initial state effect is a result from the electronic structure of any atom or ion undergoing photoelectron emission which is existed before the photoelectron emission process. These effect consist of spin-induced interaction and columbic interaction. Spin-induced interaction or spin orbit splitting: All photoelectrons from orbitals illustrated by a nonzero angular momentum quantum number (l>0) will be exhibited as

a fine structure which shows the splitting of core level into two levels. This is called another name as spin orbit splitting, and it is an atomic property which exhibits an element and level specific degeneracy and energy separation. Spin orbit splitting is due to the coupling of the magnetic fields provided by an electron spinning around its own axis as defined by magnetic spin quantum number (m_s). Therefore, there are two possible magnetic field splitting out as shown from the Table 3.1 [48].

Table 3.1: Illustrates the spin orbit splitting factors for electrons in the specific orbits.

Orbitals	l=(n-1)	m_s	j=|l±m_s|	Area ratio=2j+1
p	1	$\pm\frac{1}{2}$	$\frac{3}{2}, \frac{1}{2}$	2:1
d	2	$\pm\frac{1}{2}$	$\frac{5}{2}, \frac{3}{2}$	3:2
f	3	$\pm\frac{1}{2}$	$\frac{7}{2}, \frac{5}{2}$	4:3

3.2.1.2 Final state effect

Core hole-induced rearrangement (subsequent excitation and relaxation processes): This effect influences the K.E. of photoelectrons as they depart the photoelectron emitting atom and ion. If a valence electron were to be excited within the timescale of photoelectron emission, it will reduce the K.E. of the outgoing

photoelectron by that same amount. If this excited valence electron were then to return back to its ground state or some other lower energy state, the de-excitation energy, may then be transferred back to the departing photoelectron, therefore influencing the measured K.E. and thus the resultant B.E. value derived. It leads to more existence than one state. Therefore, more than one photoelectron peaks are observed from specific level of a specific element. There are three common groups as following [48].

Shake-up satellites (excitation of valence band electrons): This process results from transitions of valence electrons to discrete and non-discrete levels located close to E_F. The process causes the satellites and the asymmetries on the main photoelectron peak [48].

Shake-off satellites (removal of valence band electrons): This is a cause of electron excitation from valence levels into unbound continuum states located above vacuum level. As a result, these lead to the broad electron peak [48].

3.3 Field Emission Scanning Electron Microscopy (FESEM)

Field Emission Scanning Electron Microscope (FESEM) is a high resolution scanning electron microscope which is developed from ordinary SEM. The main differences between FESEM and SEM are the emitting types; field emitter for FESEM and thermionic emitter for SEM. In the thermionic emitter, a filament is heated up using electrical current. The most two commons thermionic emitters are Tungsten (W) and

Lanthanum Hexaboride (LaB_6) while field emitter is usually made of Tungsten (W) single crystal wire (~100 nm diameter) shaped into a small sharp point [49].

As result of low brightness produced by thermionic source, it is a main cause of not having enough current density in order to focus electron beam into small spot size for higher resolution. Moreover, the thermionic emission needs high temperature for activation at the filament leading to short life time in utilization approximately 2330 and 1530°C for tungsten hairpin and single or multi-crystal of lanthanum hexaboride, respectively.

In contrast, field emission gun (FEG) does not need to heat the filament, but the large amount of electrons are pulled off from the FEG by strong electrostatic field called an extraction voltage. FEG represents better significant advantages than thermionic emitters consisting of high brightness (100x), high current, much smaller electron spot size for high resolution, and long life time. Thus, in operating FESEM, the ultrahigh vacuum is needed in the column of the microscope. FESEM (SU-8000, Hitachi) and EDX (EDAX, AMETEK) operated at 10 kV were used to examine the morphology of the films and determine the elemental composition, respectively.

3.3.1 Electron-matter interaction

There are three main phenomena occurring during electron beam interaction with samples as shown in Figure: 3.3.
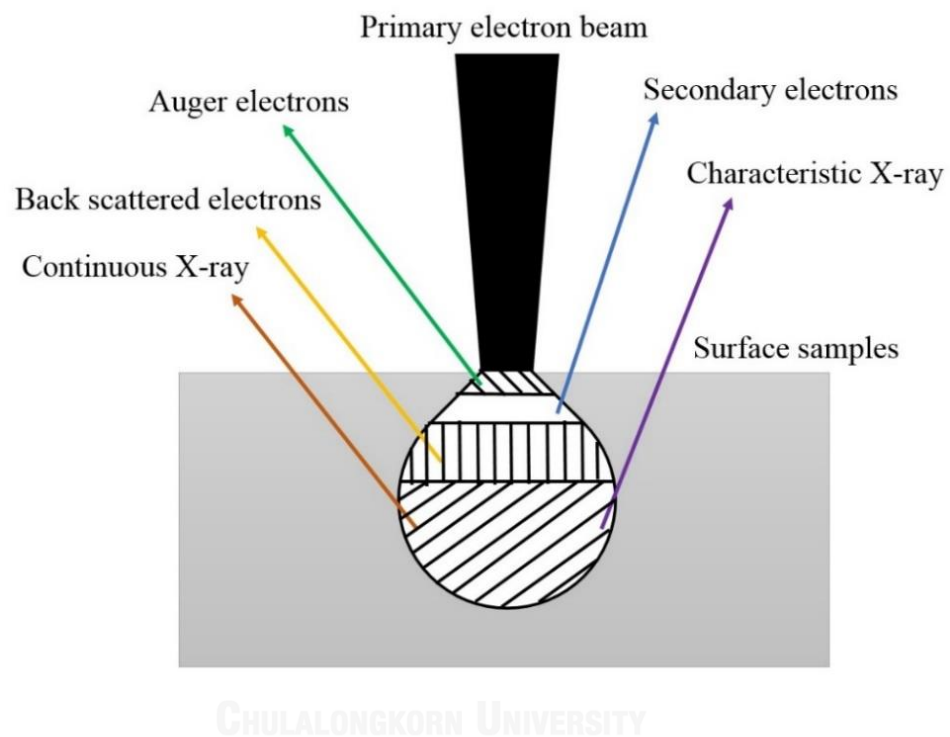
Figure 3.3: The various types of generated X-rays after electron beam is focused on the sample surface.

3.3.1.1 Secondary electrons

When the primary electron beam hits a sample, it interacts with the atoms in the sample. Primary electrons colliding electrons from the inner shells of atoms on surface and transfer energy to ionize atom and this phenomenon is called inelastic collision. The energetic electrons due to colliding with primary electron are called secondary electrons. Basically, secondary electrons have energies approximately 2-50 eV [49].

3.3.1.2 Backscattered electrons (BSE)

While primary electron beam bombards on the surface, there will be some electron backscattered electrons without energy loss or elastic collisions. Generally, the electron trajectory is changed by more than 90 degree from the forward direction of motion and backscattered electrons have energies in the kV range [49].

3.3.1.3 Characteristic X-rays

When the secondary electron is knocked out from atoms leaving a vacancy, then an electron will transition from higher energy level to occupy in that vacancy. The rules of each possible transition obey the selection rules. As a result, the energy released from the electron transitions as characteristic X-rays and that can be used to identify the type of elements and the quantity of each element of the specimen. This concept is used in electron dispersive X-rays spectroscopy [49].
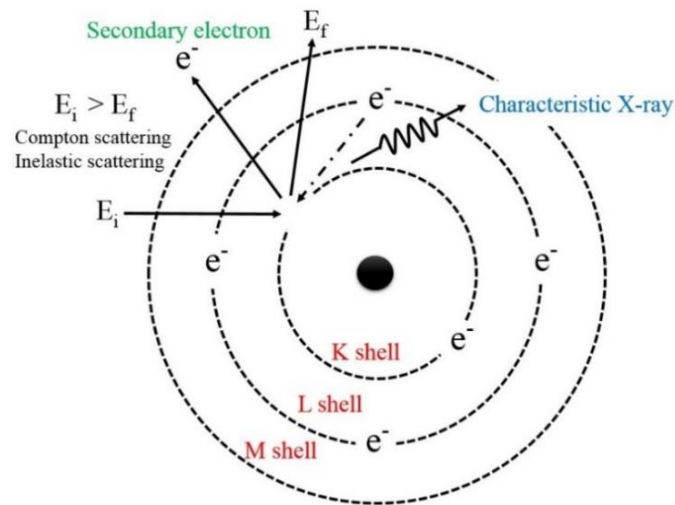
Figure 3.4: The Characteristic X-ray and secondary electrons.

3.3 Atomic Force Microscope (AFM)

Atomic Force Microscope (AFM) is an alternative instrumental equipment for surface morphology analysis. The basic principle for generated image in AFM is laterally scanning on the samples under a fine tip. The interaction between the tip and surface can be described by Lennard Jones potentials shown in Figure: 3.5. AFMs operate by measuring force between a tip and the sample. The probe consists of a cantilever with a very sharp tip to scan over a sample surface. As the tip approaches near surface sample in the range higher than 2 Angstrom, the attractive forces increase and the energy increase as negative potentials causing the cantilever to deflect towards the surface. While the tip approaches near atoms on surfaces with less than one Angstrom, the repulsion begins playing a role instead of attractive force because the cloud electrons start overlapping in each other as defined by Pauli's repulsion causing

the cantilever to deflect away from the surface. The AFM can be operated normally in three modes, a contact mode, a non-contact mode and a tapping mode depending on the application as described below:

Contact mode: the deflection of cantilever is kept constant.

Non-contact mode: the tip is oscillated at the resonance frequency and the amplitude of the oscillation is kept constant.

Tapping mode: the operation is somewhere between the contact and non-contact mode.

For a non-contact mode and a tapping mode, the cantilever is vibrated or oscillated at a given frequency. The sample is placed on the PZT scanner. The measurement of an AFM is made in three-dimensional topography, the horizontal X-Y plane and the vertical Z dimension. As shown in Fig. 3.6, a laser beam from He-Ne laser tube is used to detect cantilever deflections towards or away from the surface. Any cantilever deflection while scanning on the roughness surface will cause slight changes in the direction of the reflected beam tracking the changes by a photo diode detector [50].
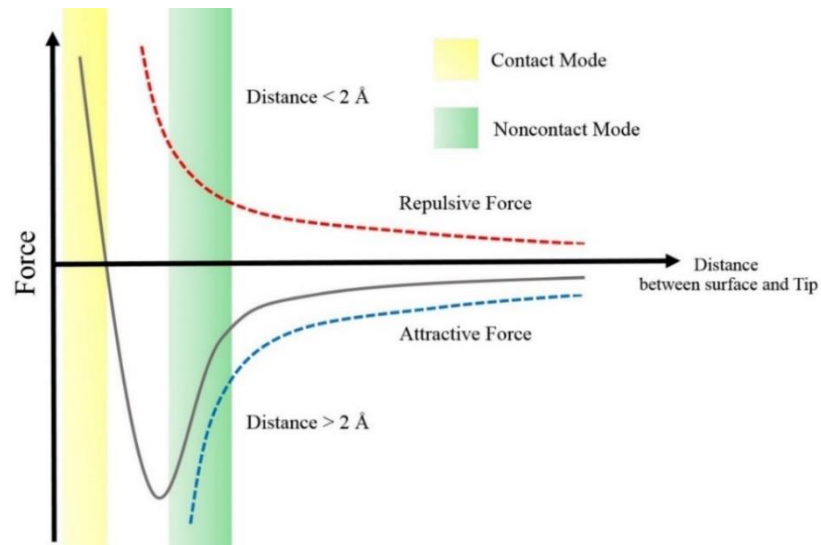
Figure 3.5: The Lennard Jones potential.
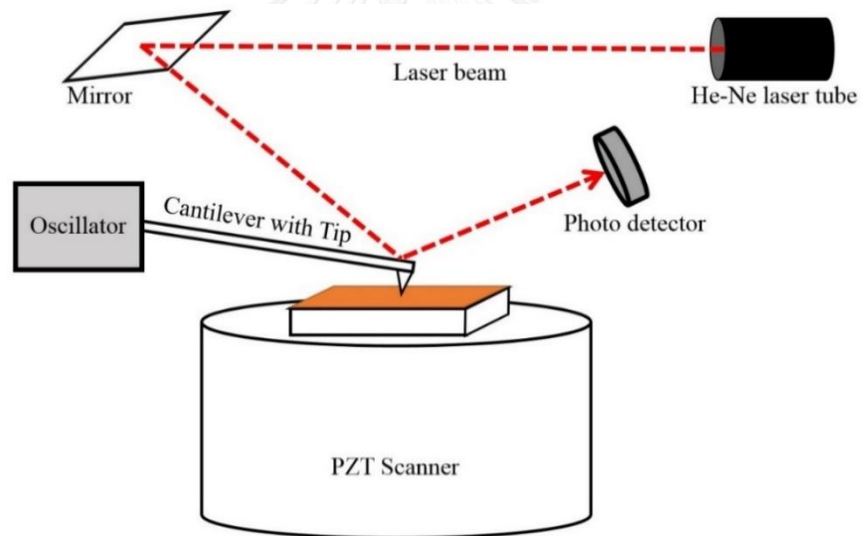
Figure 3.6: The schematic diagram of atomic force microscope.

The measurements were performed with Atomic Force Microscopy (AFM, VEECO model Nanoscope IV) by using tapping mode with scanning area size 1x1 and 2x2 μm^2 in order to observe surface morphology and the roughness of the films.

3.3.1 Root Mean Square Roughness (RMS roughness)

The roughness average is the most widely used value to compare among other samples. The RMS roughness is defined as the standard deviation of the surface height values which are varying across the whole horizontal surface area. RMS roughness is always a positive sign [50].

$$RMS = \sqrt{\frac{\sum_{i=1}^{N}(Z_i - \overline{Z})^2}{N}} \qquad (3.8)$$

Z_i is the surface height for each point.

$\overline{Z}$ is the average of the surface height over a region of interest.

N is the number of point over a region of interest.

3.4 Raman spectroscopy

Raman spectroscopy is the inelastic scattering of a photon and of course an alternative technique for structural analysis. This technique is used to observe molecular vibrations by an inelastic scattering process at which an absorbed photon is re-emitted with lower energy. The difference between the energy of excitation photons and the energy of scattered photons corresponds to the energy required to excite a molecule to a higher vibrational mode. While molecule and basis in crystals are vibrationally quantized by the monochromatic light, its scattering leads to Raman shifted lines which cause the changes in the polarizability [51].

There are three main types of emitted radiation of Raman scattering

1. Rayleigh (elastic) scattering

2. Stoke (inelastic) scattering

3. Anti-stoke (inelastic) scattering

Figure 3.7: The Raman scattering diagram [51].
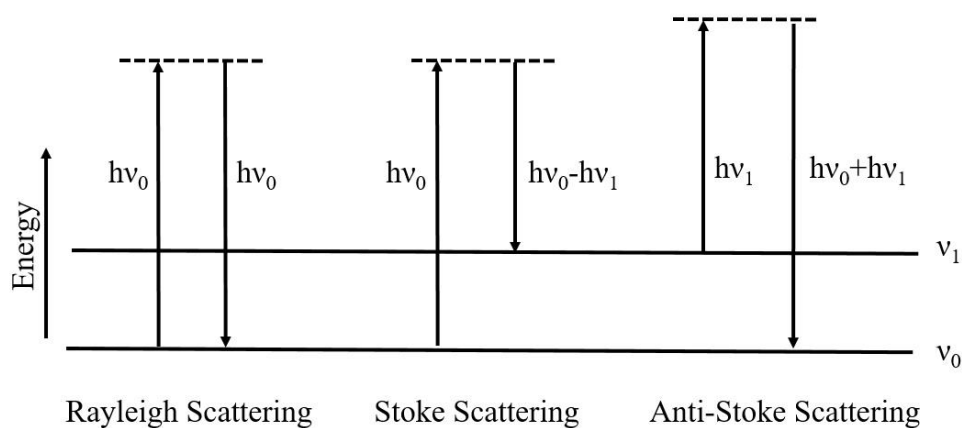
$$\nu_0 - \nu_1 \text{ (Stoke line)} > \nu_0 + \nu_1 \text{ (Anti-stoke line)}$$

Here are some applications of Raman spectroscopy. Raman scattering can be utilized in order to require of composition, structure, coordination of metal-ligands and stability of molecules. Samples can be also both liquid and solid. Therefore, Raman spectroscopy can be performed in wide range of scientific research such as biology, chemistry, and material research. The chemical fingerprint and vibration modes of the material phases were verified by Raman Spectroscopy (NT-MDT, NTEGRA Spectra) with a red laser source (= 633 nm).

CHAPTER IV

EXPERIMENTAL METHODOLOGY

This chapter focuses on the experimental details divided into three main parts. The first part concerns sol-gel synthesis and thin film preparation. Second part, the CCTO and Fe-doped CCTO thin film characterizations through spectroscopy and microscopy such as X-Ray Diffraction (XRD), Field Emission Scanning Electron Microscopy (FESEM), Energy Despersive X-ray scpectroscopy (EDX), Raman spectroscopy, and Atomic Force Microscopy (AFM) are described. The third part is about photo-litthography process, the gas sensing and capacitance measurements.

4.1 CCTO preparation

4.1.1 CCTO and Fe-doped CCTO thin film synthesis

The specimens of $CaCu_3Ti_4O_{12}$ doped with Fe at 0, 3, 5, 7 and 9 wt% were prepared by adding the necessary amounts of iron(II) sulfate heptahydrate ($Fe(II)SO_4 \cdot 7H_2O$, UNILAB, 98%) into the sol precursor solutions, which would be used to deposit sensing films. To prepare the sol solution, calcium acetate dehydrate ($Ca(C_2H_3O_2)_2 \cdot xH_2O$, Sigma, 99%) and copper (II) acetate dehydrate ($Cu(II)(C_2H_3O_2)_2 \cdot H_2O$, Fluka, 99%) were dissolved into glacial acetic acid (25 ml) and

maintained under magnetic stirring for 24 hours at room temperature. A solution containing 6.12 gram of titanium (IV) isopropoxide (Ti(OCH(CH$_3$)$_2$)$_4$, Sigma, 97%) dissolved in 3 ml of ethylene glycol and 3 ml of formamide was then added to the mixture. The previous precursor solution was heated at 120 °C before adding titanium (IV) isopropoxide, ethylene glycol and formamide. The container was sealed and continued heating at 120 °C for 4-5 hours. Some precipitates might be developed in the precursor solution within a few hours. In all cases, the clear supernatant portion of the precursor mixture would only be used to produce sensing films. The thickness of the films depending on the numbers of the depositing film layer (# layers) can be controlled by the repeating the deposition steps. The sol-gel procedure for CCTO film preparation is summarized as shown in Figure 4.1.

According to Y. Kaza [52], a former postgraduate student who was studying the effect of annealing temperature on the crystal structure of CCTO observed by XRD experiment. From the results, there were no any CCTO diffraction peaks for the films annealed at temperature lower than 800 °C (600 °C and 700 °C) and the grain sizes of CCTO annealed at 800 °C exhibited smaller grains compared to that of CCTO films annealed at 1000 °C. The variation of the microstructures based on the grain sizes for Fe-doped CCTO film was small. In addition, as reported from T. Supasai's doctoral thesis [53], the surface grain sizes of another type of perovskite films (SrTiO$_3$/BaTiO$_3$) multilayer films annealed at 1000 °C varied dramatically with Fe-doping concentration. In general, the grain size may vary to some extent with the degree of metal doping. Thus, to only address the effect of grain sizes and doping on the sensing capabilities of the films, the Fe-doped CCTO films annealed at 800 °C are selected to study their gas sensing properties. Also, the temperature at 800 °C was selected for annealing growth

condition for gas sensing devices due to small surface grains regardless of their crystallinity. It is possible that the surface area of reaction of the film increases with smaller grains [54]. For capacitor fabrication, the temperatures at 800 $^{\circ}$C and 1000 $^{\circ}$C were chosen for annealing conditions in order to compare the crystallinity and the preferred orientation of the films affecting to the improvement of dielectric constants.
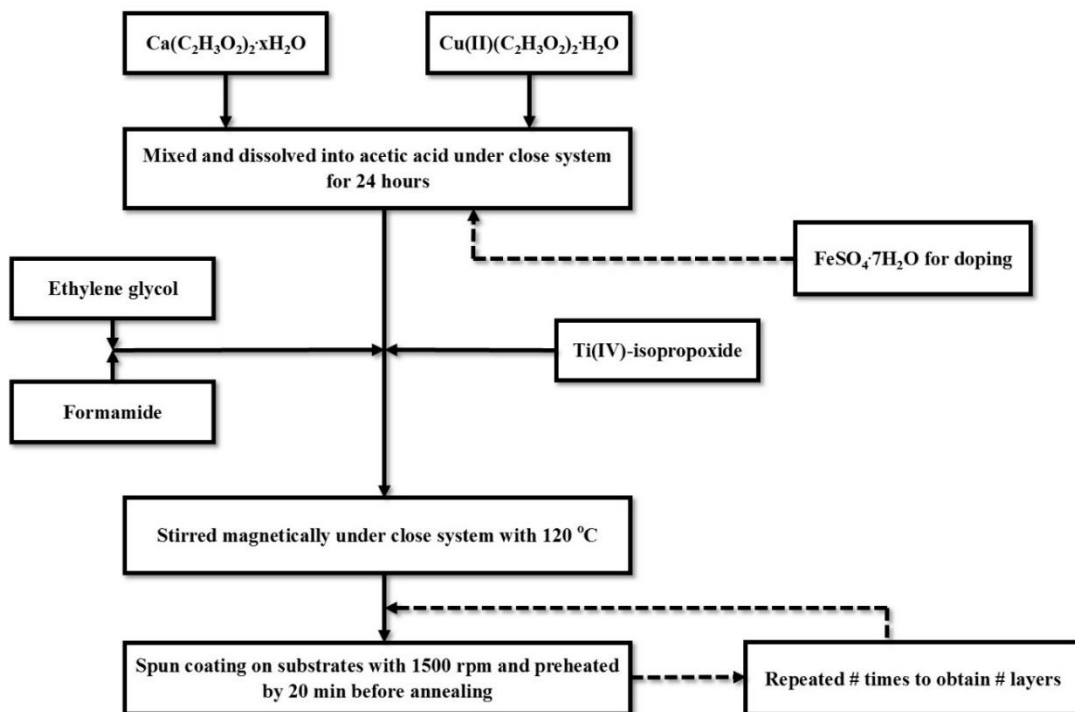
Figure 4.1: The flow chart diagram of pure and Fe-doped CCTO synthesization.

In addition, the concentration of Fe dopants cannot be added over 9 wt% as a result of saturation in precursor solution which become gel quite quickly during heating and a lot of precipitation.

4.1.2 Substrate types and substrate conditioning

There are four main types of substrates used in this experiment such as silicon (100), lanthanum aluminate (LaAlO$_3$; LAO) (100), neodenium gallate (NdGaO$_3$; NGO) (100), and alumina substrates (Al$_2$O$_3$), and some physical properties have been shown in the following tables (Tables 4.2-4.5). For gas sensing applcations, alumina are utilized as substrates and it is cut to 2.5 cm×2.5 cm×0.2 mm size. Silicon substrates with the area of 10 mm^2 are for only thin film characterization, but not for device fabrication. LaAlO$_3$ and NdGaO$_3$ substrates are used for the insulator base in fabricating CCTO film coplanar capacitors due to the small lattice mismatch between the film and the substrate, small difference in thermal expansion coefficient compared to CCTO, and small dielectric constants and loss tangent (δ), dielectric constant (ε) which is ~ 23 for LaAlO$_3$ and ~ 20 for NdGaO$_3$.

In order to grow thin films with good quality, the substrates have to be very cleaned and no dusts or any organic materials on their surface. Those substrates were put vertically into the slots made of Teflon for ultrasonic cleaning purpose. All types of substrate were ultrasonically cleaned in two steps with acetone and isopropanol alcohol (IPA) for 15 min in each cycle. After finishing cleaning process, the samples were heated approximately at 80 ºC for water elimination. Next, the precursor solution was dropped onto each type of substrate (silicon, alumina, lanthanum aluminate, and neodymium gallate) placed on the spinning chuck equipped with the spin coating system. The constant spinning speed is 1500 rpm maintained for 30 sec. The samples were then baked at 120 °C for 20 min as so called dying or pre-heating process before being annealed at 800 °C for one hour with a constant ramping heating rate of 10 °C

per min from room temperature. The certain number of cycles of spin coating was applied to each chosen substrate to obtain homogeneous and optically smooth films with a single layer thickness of approximately 100 nm.

Table 4.1: Si (100) substrate properties. (SurfaceNet GmbH, Germany)

Physical properties of Si (100) substrate	
Crystallographic structure	Cubic phase lattice constant a=5.43 Å
Twinning structure	Twin free
Color	Shiny gray (Polished side)
Density	2.33 g/cm^3
Melting point	1420 °C
Thermal expansion	4.05×10^{-6} K^{-1}
Dielectric constant	~11.9 at 300 K

Table 4.2: LaAlO$_3$ (100) substrate properties. (SurfaceNet GmbH, Germany)

Physical properties of LaAlO$_3$ (100) substrate	
Crystallographic structure	Rhombohedral phase at room temperature lattice constant a=b=5.43 Å and c=13.123Å
Twinning structure	Orthogonal twin plane along (100)
Color	Shinny light brown (Polished side)
Density	6.52 g/cm^3
Melting point	2080 ºC
Thermal expansion	1.0×10^{-5} K^{-1}
Dielectric constant	~25 at 300 K
Dielectric loss	3.0×10^{-4} at 300 K

Table 4.3: NdGaO$_3$ (100) substrate properties. (SurfaceNet GmbH, Germany)

Physical properties of NdGaO$_3$ (100) substrate	
Crystallographic structure	Orthorhombic phase lattice constant a=5.426 Å b=5.496 Å and c=7.707 Å
Twinning structure	Twin free
Color	Shinny dark violet (Polished side)
Density	7.56 g/cm^3
Melting point	1605 ºC
Thermal expansion	9.0×10^{-6} K^{-1}
Dielectric constant	~9 at 300 K
Dielectric loss	~2.0-3.0×10^{-3} at 300 K

Table 4.4: Alumina substrate properties. (obtained from NECTEC)

Physical properties of Al$_2$O$_3$ substrate	
Crystallographic structure	Rhombohedral phase lattice constant a=b=4.759 Å and c=12.993 Å
Twinning structure	Twin free
Color	White
Density	3.85 g/cm^3
Melting point	2052 ºC
Thermal expansion	~8.18×10^{-6} K^{-1}
Dielectric constant	~9.8 at 300 K
Dielectric loss	~2.0×10^{-4} at 300 K

4.1.3 Sol-gel

The sol-gel method is a wet chemical process for colloidal-particle synthesis consisting of organic inorganic compound in a solution. It is a useful approach to prepare materials in the form of complex metal oxide and others with a variety of shapes, such as porous structures, thin fibers, dense powders and thin films. A sol is a stable dispersion of colloidal particles or polymers at which may be amorphous or crystalline in a solvent. While a sol is particles in a liquid, an aerosol is particles in a gas phase A gel consists of a three dimensional continuous network, which encloses a liquid phase. The sol-gel solution includes metal alcoxides ($M(OR)_2$) where R is alkyl group. There are two main processes, hydrolysis and condensation, in the sol-gel mechanism [55].

$$MOR + H_2O \rightarrow MOH + ROH \qquad \text{Hydrolysis}$$

$$MOH + MOR \rightarrow MOM + ROH \qquad \text{Condensation}$$

$$MOH + MOH \rightarrow MOM + H_2O \qquad \text{Condensation}$$

Actually, both hydrolysis and condensation processes occur at the same time. Hydrolysis is the reaction of water with some precursor molecule with the formation of usually undesired. In the hydrolysis, the alkyl group is exchanged by hydroxyl group coming from the water molecule. Repeating the reaction of this kind on the titanium alcoxide leads to the formation of a hydrated titanium oxide in our preparation case. Condensation can be described as networking process in which an alcohol is eliminated

upon reaction between metal hydroxide and metal alcoxide. The condensation reaction can also occur between two metal hydroxide molecules whereby a water molecule is eliminated. The main products from these reactions are networked oxides and thus, condensation could be considered a polymerization. Condensation continues during the heating stages of the preparation where water and alcohol molecules are irreversibly eliminated while only the refractory oxide phase is left.

4.1.4 Spin coating process

Spin-coating process has been a versatile utilization in both biological and physical science for several decades. It can be applied for thin film preparation. Basically, the process associates through dropping a solution on a substrate during high speed rotation. Then, the centripetal acceleration is a cause of the solution spreading out from substrates. There are many factors that could affect the gel formation during the spinning process. For instance, the fluid viscosity is related to the thickness formation behavior of the film during spinning process at constant spinning speed. Solvent evaporation also occurs during the coating process. The surface tension on substrates affects the adhesion between viscously liquid phase and solid surfaces. The percentage of solid particles mixture dissolved into precursor solution can vary the thickness of films. The thickness variation for thin film deposition with spin coating can be described with the Eq. (4.1).

$$t \propto \frac{1}{\sqrt{\omega}} \hspace{4cm} (4.1)$$

t is the film thickness and ω is the angular velocity. This equation defines the relationship of film thickness which is inversely proportional to square root of angular velocity.

After the CCTO films were obtained, the films grown on alumina LAO and NGO substrates are brought to fabricate the interdigited Au/Cr electrodes by UV light patterning or lithography process. The CCTO films deposited on silicon substrates are used for only common characterizations. Briefly, the interdigitated electrodes were patterned by a standard photolithographic patterning process using a positive photoresist (AZ 4620, Microchem Inc.), sputtering of Cr/Au layers and photoresist exposure to a UV light and followed by lift-off process by ultrasound treatment in acetone. Note that for the capacitor devices, the electrode is made of aluminium (Al) because it is cheaper than gold (Au). The film sensors were then annealed at 400 ºC to remove all carbon residues from the surfaces. Finally, the sensors were cut into individual coplanar sensor/capacitor with the area of 2mm×3mm using a dicing saw (Model: ADT 7100 Series 2 VECTUS). The CCTO films on alumina were loaded into a gas-sensing chamber for the gas sensing purpose. On the other hand, the CCTO on LAO and NGO substrates were probed to measure the capacitance and corresponding loss tangent.
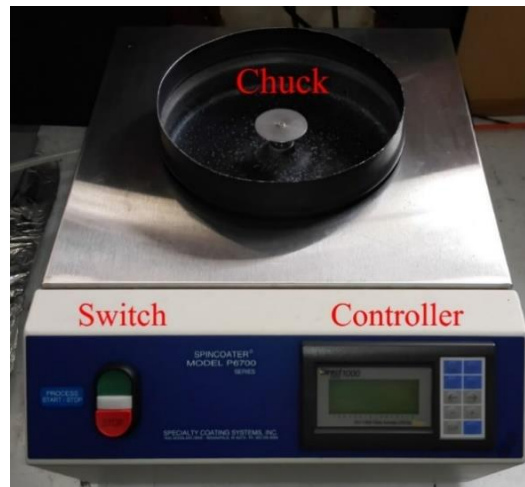
Figure 4.2: The spin coators MODEL P6700 Series.
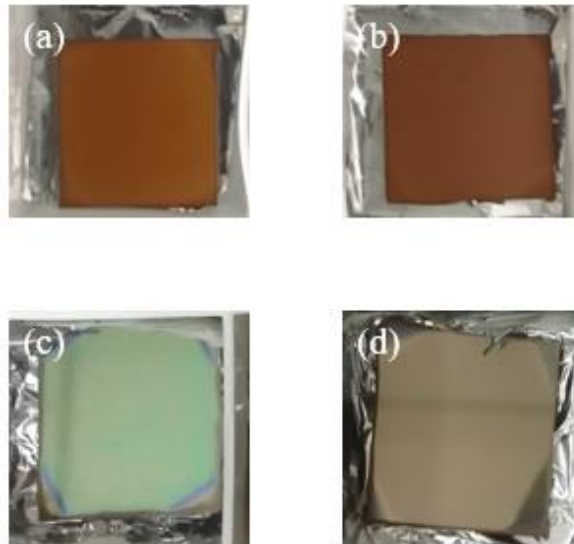
Figure 4.3: (a) and (c) Undoped and (b) and (d) Fe-doped CCTO on alumina and silicon substrates.

(a) Spin coated positive photoresist

(b) UV exposing on quartz stacked on shadow mask to photoresist

UV light
Quartz
Shadow mask
Photoresist

(c) Lift off photoresist in developer and DI water

(d) Sputtering electrode on the pattern

Metal electrode

(e) Lift off by ultrasonic with acetone
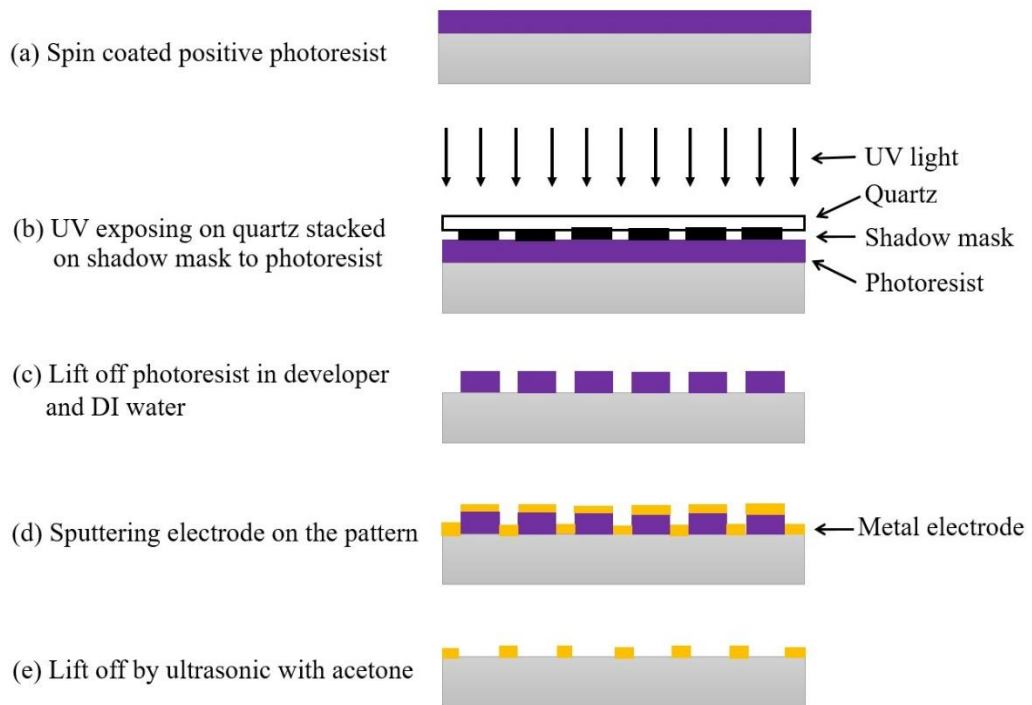
Figure 4.4: The overall process of photolithography for patterning metal electrodes.

Figure 4.5: Spin coating the substrate with the photoresist.
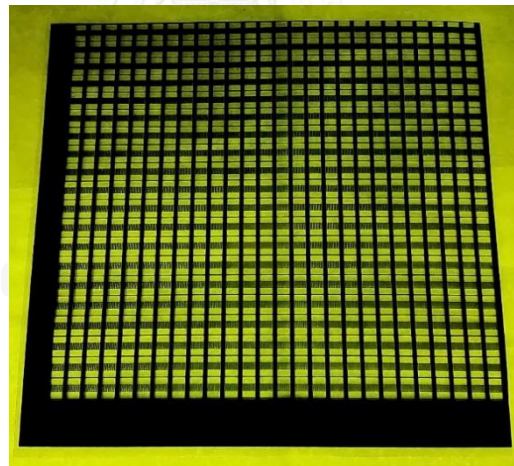
Figure 4.6: The inter-digitated shadow mask.
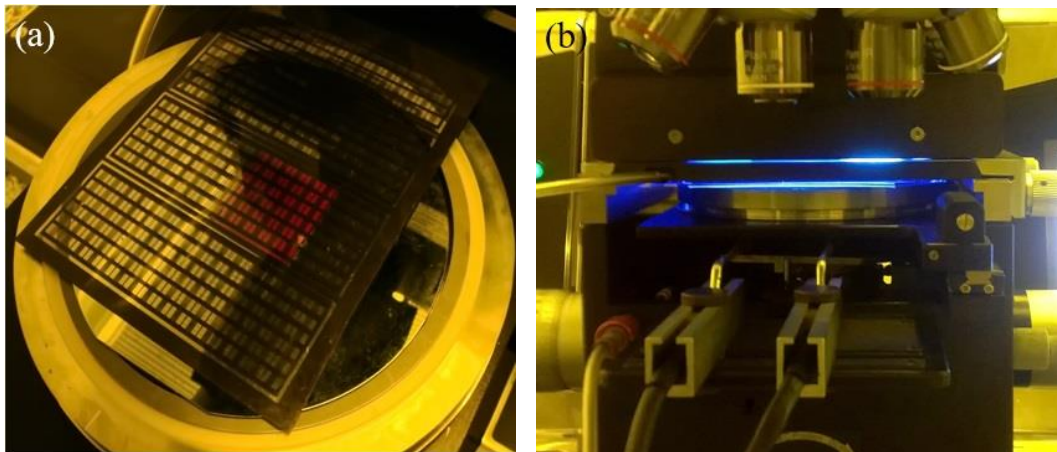
Figure 4.7: (a) Placing the inter-digitated shadow mask onto the CCTO film previously coated with the photoresist b) Exposure of the photoresist to UV light.
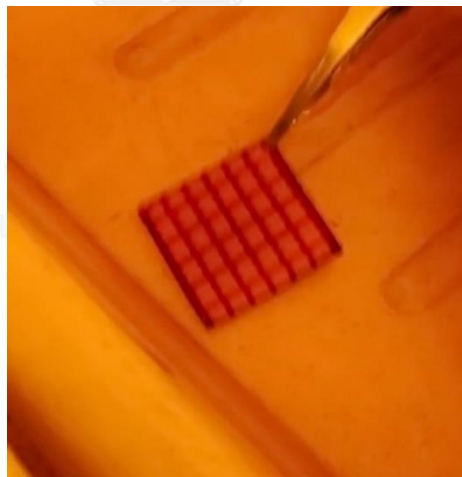
Figure 4.8: Developing the pattern in the developer.
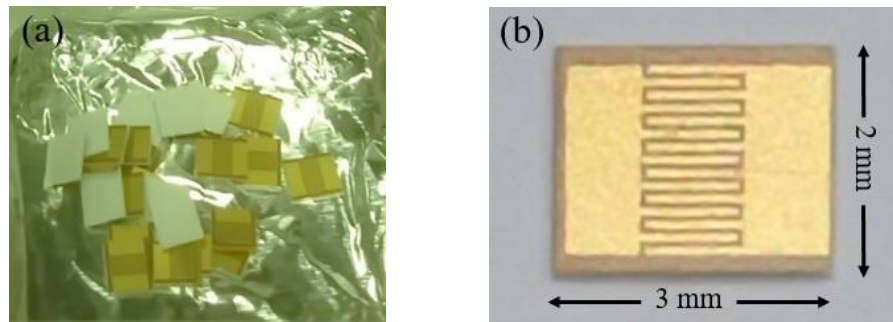
Figure 4.9: (a) The devices after dicing (b) The individual device.
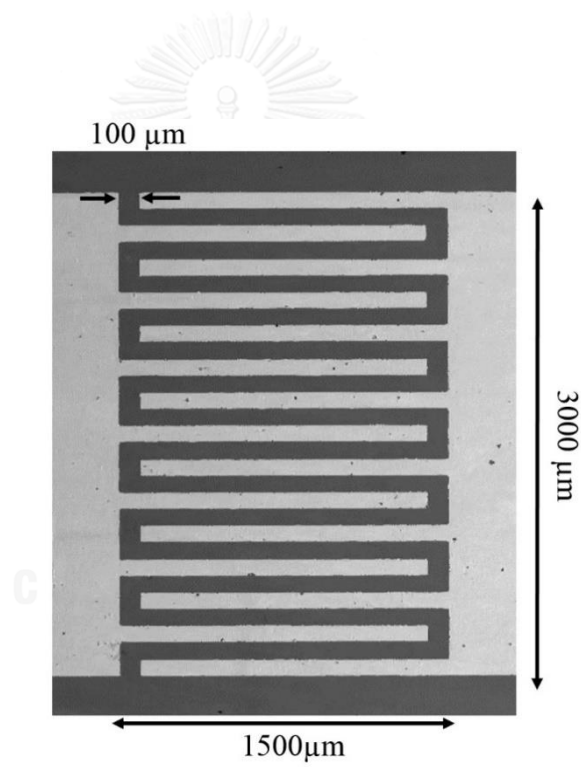
Figure 4.10: The photograph of patterned sample.

4.2.3 Gas sensing measurement

All types of gas sensing characterization are measured at Nanoelectronics and MEMs laboratory, National Electronic and Computer Technology Center (NECTEC). The sensing measurement is begun performing by thermally activated samples in the chamber through temperature controller. For gas sensing measurements, CCTO sensors were heated by an external NiCr heater to the operating temperatures ranging from 150 to 350°C under dry air in a stainless steel chamber. The target gas source was flowed at different flow rates to mix with dry air to obtain desired concentrations using mass flow controllers (Brook Instrument). The resistances of various sensors were continuously monitored with a computer-controlled system by voltage-amperometric technique with 10 Volt dc bias and current measurement through a 6487 Keithley picoammeter. The gas sensing properties of CCTO sensors were characterized in terms of response and response time as a function of gas concentration and operating temperature towards various gases including hydrogen sulfide (H_2S), ammonia (NH_3), nitrogen dioxide (NO_2), ethanol (C_2H_5OH), carbon monoxide (CO), methane (CH_4) and acetylene (C_2H_2).

The gas-sensing response (S) is given by

$$S = \frac{R_a}{R_g} \qquad (4.2)$$

R_a and R_g are the electrical resistances of sensor measured in the presence of pure dry air and reducing gas, respectively.

The definition is reversed for oxidizing gas. The response time is the time required to reach 90% of the steady-state response signal and the recovery time is the time to recover to 90% of the baseline value.
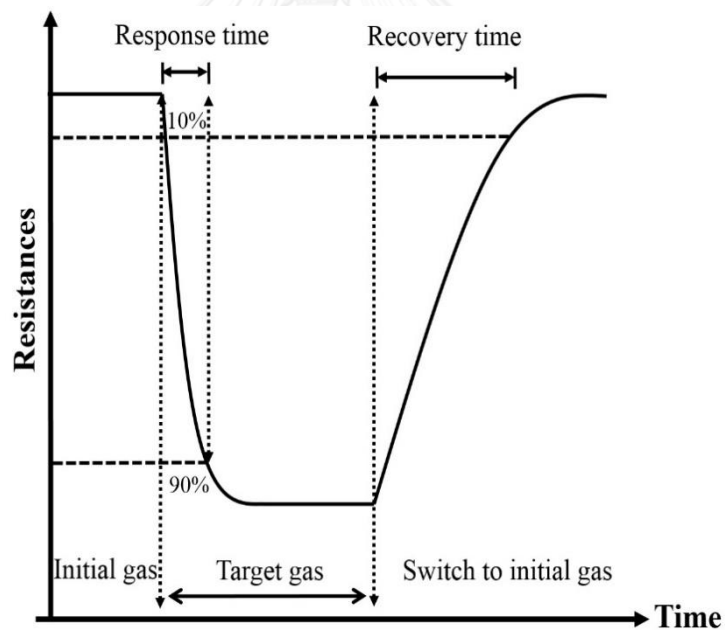
Figure 4.11: The sensing diagram.
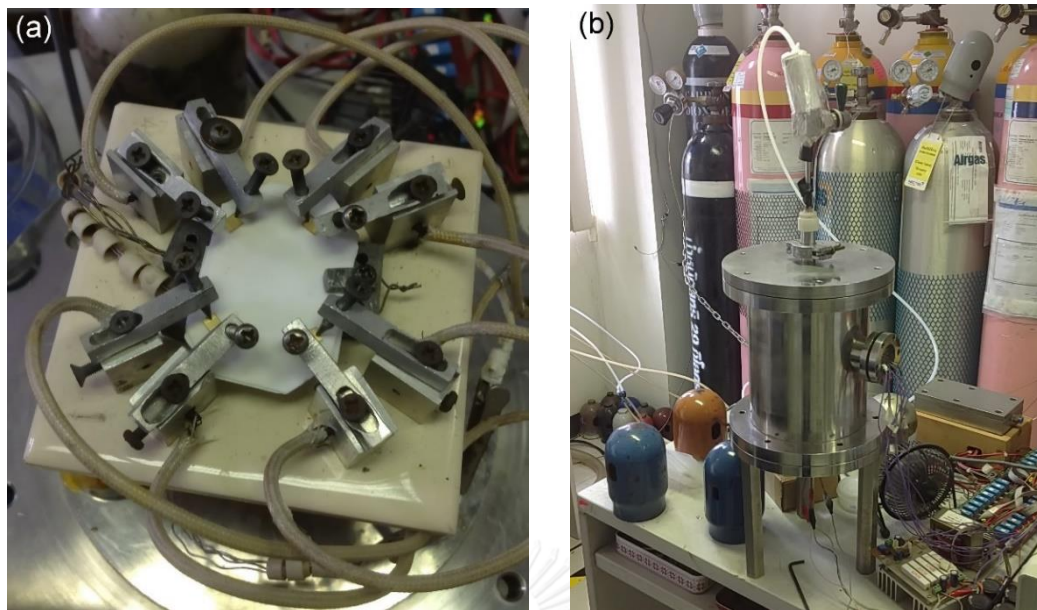
Figure 4.12: (a) The sensing devices loaded onto the state are contacted with probes and (b) The gas chamber for gas sensing measurements.

4.2.4 Capacitance measurement

In this research, our coplanar thin film capacitors are probed using a commercial LCR analyzer (Model: 4294A, Agilent) in order to measure capacitance and loss tangent for both undoped and Fe-doped CCTO films deposited on single crystal substrates. The capacitance of CCTO thin films can be converted to dielectric constant by using Fernell's approximation. The condition for capacitance measurements are set at room temperature with the range of frequency between 10-1000 kHz and applied voltages at 500 mV which will be tested in this research.

Figure 4.13: Impedance analyzer (Agilent 4294A).

4.2.4.1 Fernell's approximation

Fernell's analysis [56]can be used to approximate the dielectric constant of thin film coplanar capacitors patterned with interdigitated electrodes as expressed below:

$$\varepsilon_{film} = \varepsilon_{substrate} + \frac{C-K(1+\varepsilon_s)}{K[1-\exp\left(\frac{-4.6h}{G+W}\right)]} \qquad (4.3)$$

ε_{film} and $\varepsilon_{substrate}$ are dielectric constant of the film and the substrates, respectively. G and W are the spacing and width of figure, respectively and h is the film thickness. K is a constant magnitude in unit pF depending on the area and gap of coplanar electrode which can be calculated by the polynomial equation shown below;

$$K = 6.5(\frac{G}{W+G})^2 + 1.08\left(\frac{G}{W+G}\right) + 2.37 \qquad (4.4)$$

C is the capacitance per unit length which is shown below;

$$C = \frac{C_m}{LN} \qquad (4.5)$$

C_m is the measured capacitance from the experiment in unit pF and L is the overlapping figure length in unit meter. N is the number of the spacing figure. Therefore, all parameters of interdigitated electrode have to be known in order to calculate the dielectric constant of the material.

CHAPTER V

RESULTS AND DISCUSSION

In this chapter, the results from the experiments are divided into six sections. The first section illustrates the crystal structure and the surface morphology of undoped and Fe-doped CCTO thin films grown on silicon substrates. The second section is about the effect of single crystal substrate types on the crystal structure and the surface morphology of undoped and Fe-doped CCTO thin films. The third section concerns the characterization of Fe-doped CCTO thin films grown on alumina substrates. The next section is about the gas sensing application of Fe-doped CCTO thin films deposited on alumina substrates followed by the fifth section, gas sensing mechanism description for H_2S which shows the best response to our CCTO films. The final section presents the dielectric properties of undoped and Fe-doped CCTO thin films deposited on LAO (100) and NGO (100) substrates.

5.1 The crystal structure and surface morphology of undoped and Fe-doped CCTO films grown on Si (100)

The CCTO films were deposited on Si (100) substrates by a precursor solution with spin coating technique. The films on Si (100) were crystallized by annealing at high temperatures, only two conditions at 800 and 1000 ^{o}C in air atmosphere for one hour for each layer of deposition. The spinning depositing process was repeated until the film thickness is thick enough to observe the intensity of X-ray patterns of the CCTO polycrystalline films which showed various planes. The CCTO grains on the film surfaces were confirmed by AFM measurements. As represented on the first condition of annealing at 800 ^{o}C in Figure 5.1 (a), the film exhibited high intensities of three main diffraction peaks, (220), (400), and (422) with other characteristic peaks (211), (310), (222), (321), and (322). This confirmed the CCTO film on Si (100) was polycrystalline. These XRD data will be useful later for comparison when the XRD patterns is represented for CCTO grown on single crystal substrates in section 5.2. However, there were some other tiny phases appearing on the film such as (110) and (220) of TiO_2 and (111) of CuO. Figure 5.1 (b) shows the XRD patterns of the film annealed at 1000 ^{o}C. There were obviously seen only three main characteristic diffraction peaks of CCTO with the secondary phase of TiO_2 having the same planes as appeared in the film annealed at 800 ^{o}C. The surface morphology of the CCTO films illustrated by AFM images reveals that there are completely different grain sizes in both films. It is noticed that the grain sizes increased as the annealing temperature increased

from 800 to 1000 ºC as shown in Figure 5.2. The X-ray patterns results of pure CCTO and Fe-doped CCTO films on Si substrates are shown in the Figure 5.3. With increasing Fe doping content increased, the peak intensities of the secondary phase of TiO_2 in rutile phase, (111) and (211) planes, increased. Obviously, the intensity diffraction peak of rutile phase at (110) plane increased due to increasing of Fe dopants in the film. The (111) plane of CuO was also observed in every sample treated under the annealing temperature at 800 ºC, but pure CCTO annealed at 1000 ºC does not show the peaks of CuO.
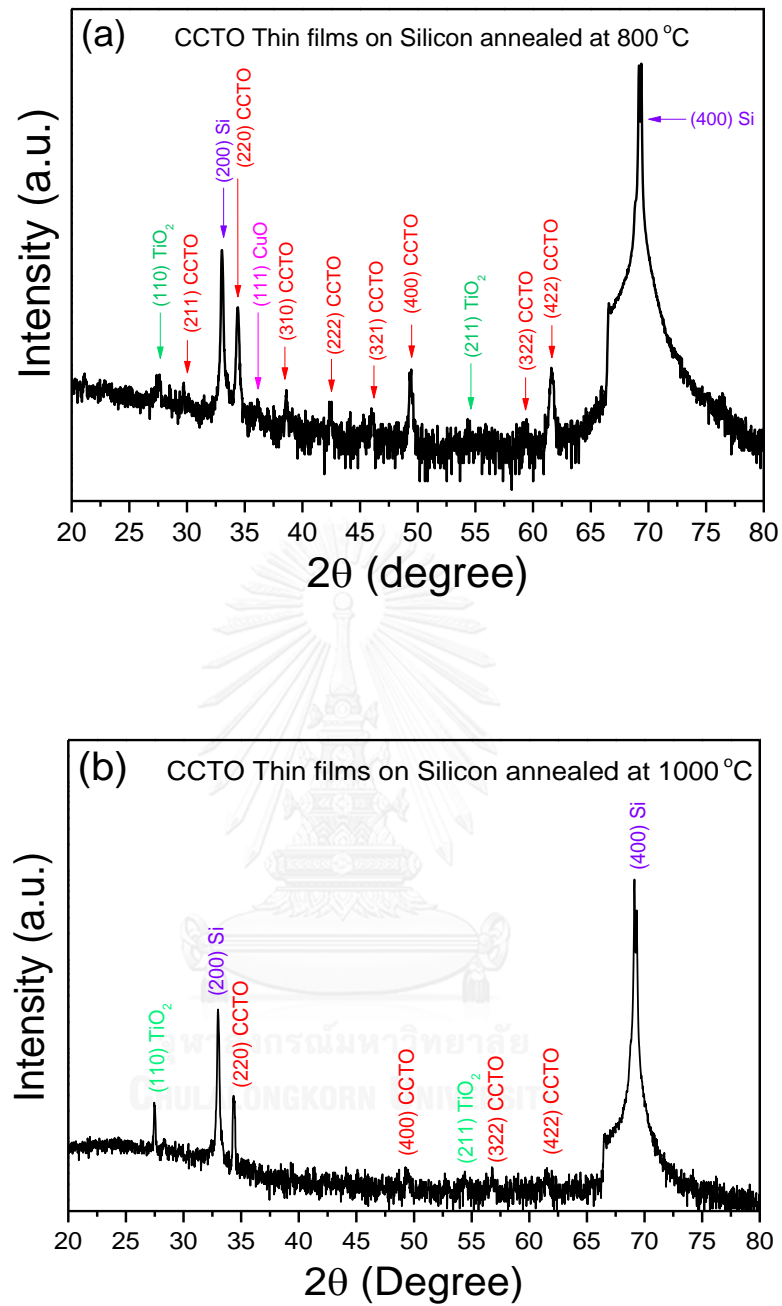
Figure 5.1: The XRD patterns of CCTO thin films annealed at (a) 800 and (b) 1000 ℃.

(a)

(b)

(c)

(d)
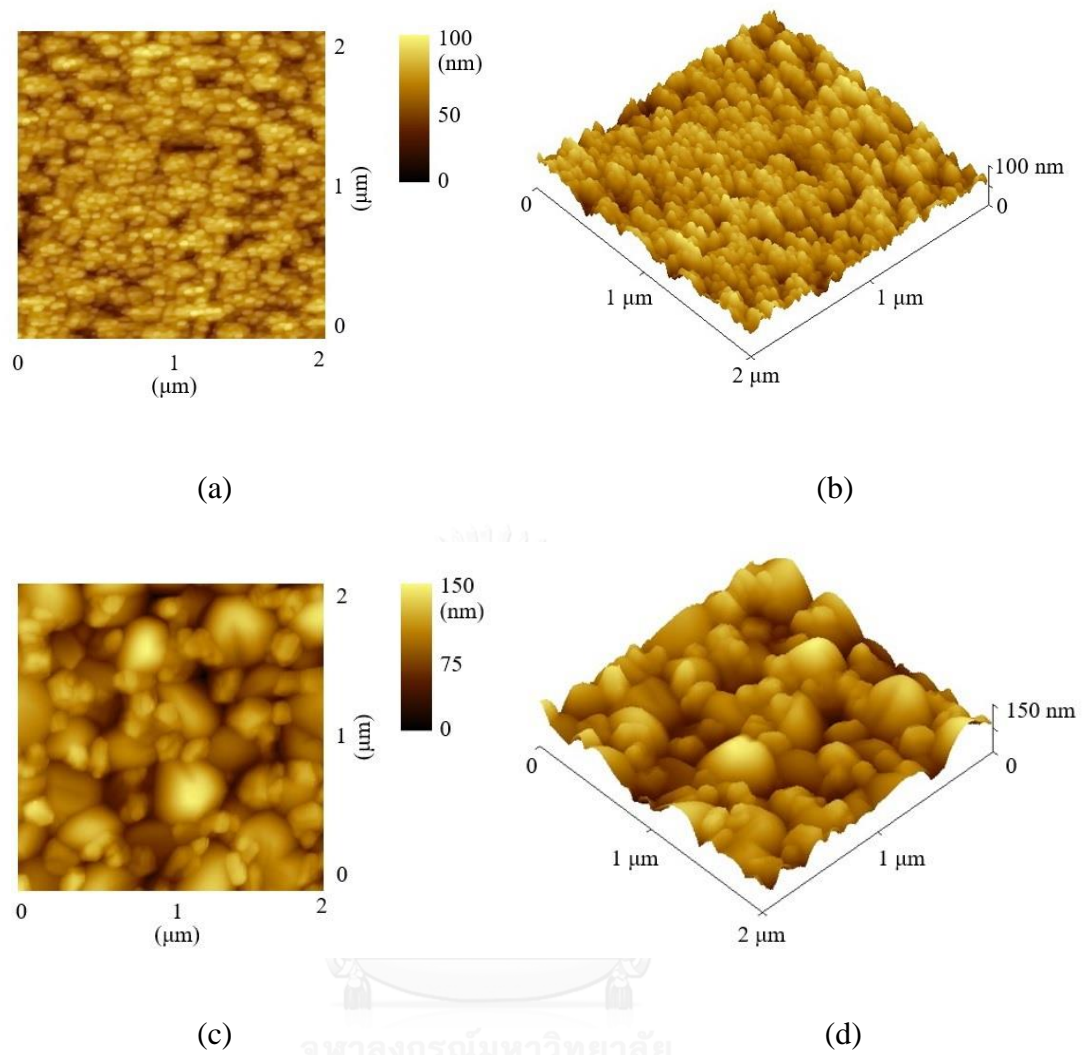
Figure 5.2: AFM images with scanning area of 2x2 μm^2 in 2D and 3D of CCTO thin films grown on Si substrates (a) and (b) were annealed at 800 °C, (c) and (d) were annealed at 1000 °C.
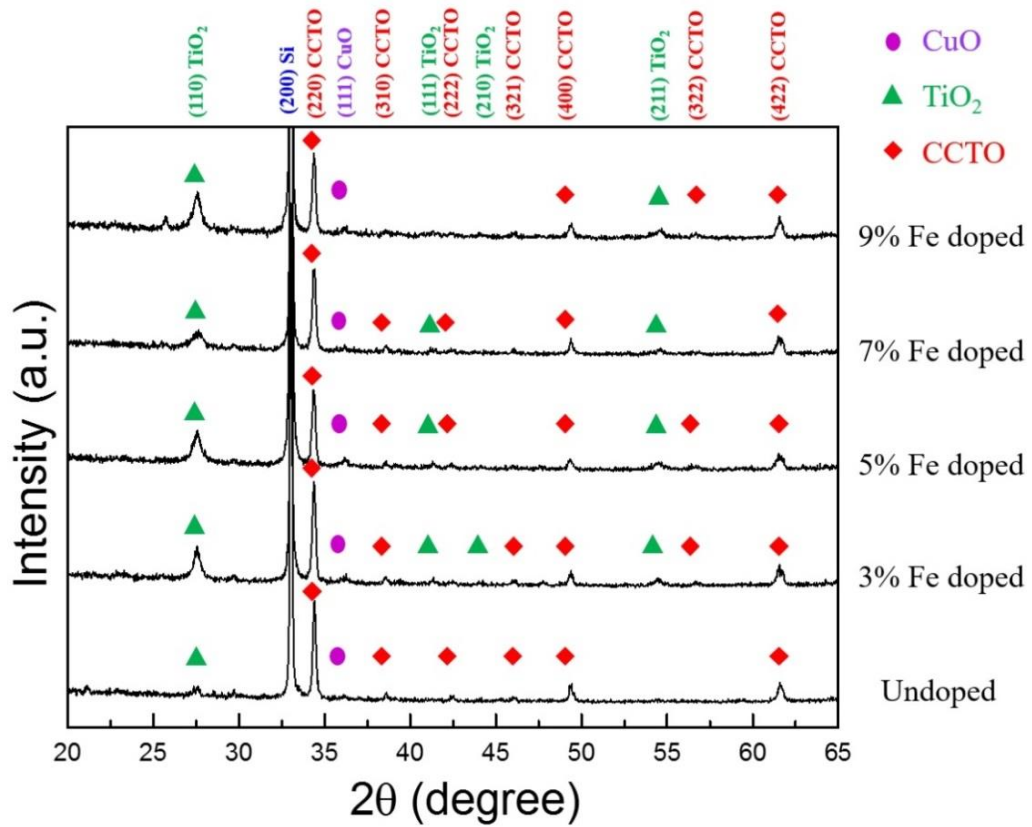
Figure 5.3: The XRD patterns of CCTO thin films grown on silicon substrates fixed annealing temperature at 800 ºC with different concentration of Fe dopants.

5.2 The influences of LAO (100) and NGO (100) single crystal substrates to preferential orientated planes of pure CCTO crystal growth

In this work, CCTO films were synthesized on LAO(100), NGO(100) and (110) single crystal substrates by a sol-gel spin coating technique. Figure 5.4 presents the XRD patterns of the CCTO films grown with different layers, two (2L) and four (4L) layers, grown on LAO (100) substrates annealed at 800ºC and 1000ºC, respectively. The intensity of the LAO substrate peaks is much stronger than that of CCTO films because the thickness of the substrate (~0.5 mm) is obviously much thicker than that of the films in the order of a few hundred nanometers. Thus, to observe the film signals, the XRD patterns were plotted in log scale allowing the secondary or impurity phases in the film to be clearly observed along with high diffraction peaks from the substrate. The (h00) reflections consisting of (200), (400) and (600) from the CCTO films are the dominant features in the film spectrum for all studied growth conditions, besides the strong diffraction peaks from the LAO substrate. Three important peaks of CCTO appeared at 2θ = 24.28º, 49.30º and 77.58º, which are indexed as the (200), (400) and (600) reflections from CCTO, respectively. However, the (200) peak is not clearly seen due to the overlapping with (100) diffraction peak from LAO substrate. From the calculation using the strongest (400) peak position, the CCTO film has a cubic structure with a lattice constant $a = 7.388$ Å ($a/2 = 3.694$ Å), while LAO has a pseudo cubic structure with a calculated lattice constant of $a = 3.79$ Å. The calculated lattice constant of the CCTO film (3.694 Å) is slightly larger than that of bulk CCTO (~3.68

Å), indicating a unit cell volume expansion of ~1% as compared to bulk CCTO. The lattice mismatch, defined as the ratio between the difference in the lattice parameter between the film and the substrate and the lattice parameter of the substrate. Thus, the calculated lattice mismatch of the CCTO film and LAO substrate is $\left|\frac{(3.694-3.79)\text{Å}}{3.79\text{Å}}\right| \times 100\% \sim 2.5\%$ which is considered to be a rather small mismatch.
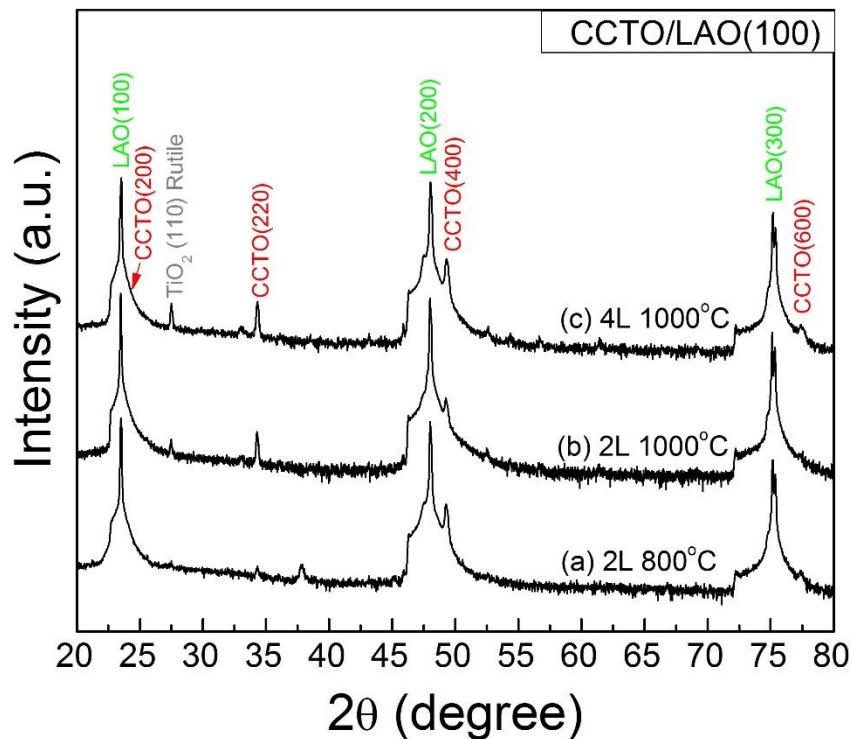
Figure 5.4: θ-2θ X-ray diffraction scan of CCTO films deposited on LAO (100) substrates annealed at 800 ℃ and 1000 ℃, respectively. (a) two-layered CCTO/LAO(100) film annealed at 800 ℃, (b) two-layered CCTO/LAO(100) film annealed at 1000 ℃, (c) four-layered CCTO/LAO(100) film annealed at 1000 ℃.
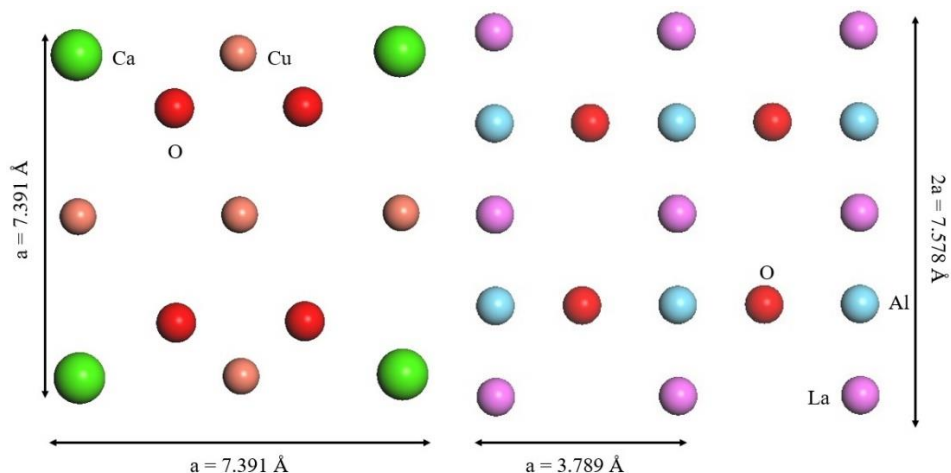
Figure 5.5: The cleaved CCTO (2h00) and LAO (h00) plane models illustrated atomic locations.

For all the studied growth conditions, CCTO films were deposited on LAO (100) substrates tends to be (h00) oriented due to the small lattice mismatch between the film and the substrate. This indicates that the CCTO film layers grow with the c-axis perpendicular to the substrate surface. Our XRD patterns of the samples are similar to that of CCTO thin film grown on LaNiO$_3$-coated Si substrate by sol-gel method at which LaNiO$_3$ (LNO) acts as seed layer during the film growth [28]. However, there was one extra (220) orientation besides a small detectable TiO$_2$ rutile impurity phase which was clearly seen for the case of such a high temperature annealing at 1000°C only. The intensities for both (h00) peaks including the addition (220) phase and TiO$_2$ (110) rutile phase increased as the film thickness increased from two-layered deposition to four-layered deposition. As known, for CCTO powders and ceramics, the maximum intensity belongs to (220) peak. To evaluate the (h00) preferential orientation of the

film, the maximum (400) intensity peak representative of all (h00) film peaks was chosen to define the ratio of (400)-orientation $\alpha_{(400)}$ relative to (220) peak for CCTO/LAO(100) films [28].

$$\alpha_{(400)} = \frac{I^{film}_{(400)} / (I^{film}_{(220)} + I^{film}_{(400)})}{I^{powder}_{(400)} / (I^{powder}_{(220)} + I^{powder}_{(400)})} \qquad (5.1)$$

where $I^{film}_{(400)}$ and $I^{film}_{(220)}$ are the relative intensities of (400) peak and (220) peak of CCTO thin film, respectively, $I^{powder}_{(400)}$ and $I^{powder}_{(220)}$ are the relative intensities of (400) peak and (220) peak of CCTO powder from XRD database (75-1149), respectively. If the value of $\alpha_{(400)}$ is larger than 1, the films are (400) preferential oriented. Compared with the two layered films with the same thickness, the calculated $\alpha_{(400)}$ for CCTO grown on LAO(100) treated at annealing temperatures of 800 and 1000ºC are 3.36 and 3.04, respectively. For four layered film annealed at 1000ºC, the calculated $\alpha_{(400)}$ was increased to 3.19 due to increasing film thickness and improving crystallinity. The maximum $\alpha_{(400)}$ of 3.36 is obtained from the 2L CCTO/LAO(100) film annealed at 800ºC which is considered the optimum growth condition for (400) preferential oriented CCTO film. Our overall calculated $\alpha_{(400)}$ are larger than the value of 2.17 reported for CCTO thin film grown on LNO-coated Si substrate [37]. Si et al. have found that the substrate temperature and the oxygen pressure in pulsed deposition system were crucial for single phase formation of CCTO [39]. They have found that

the CCTO thin films deposited on SrTiO$_3$ (100) using as a buffer layer at 780ºC or 20 mTorr showed the (310) orientation along (h00) orientation. In our preparations, the effects of varying oxygen pressure during the annealing process to control the levels of impurity phases and to maintain only the single (l00) phase was not attempted.
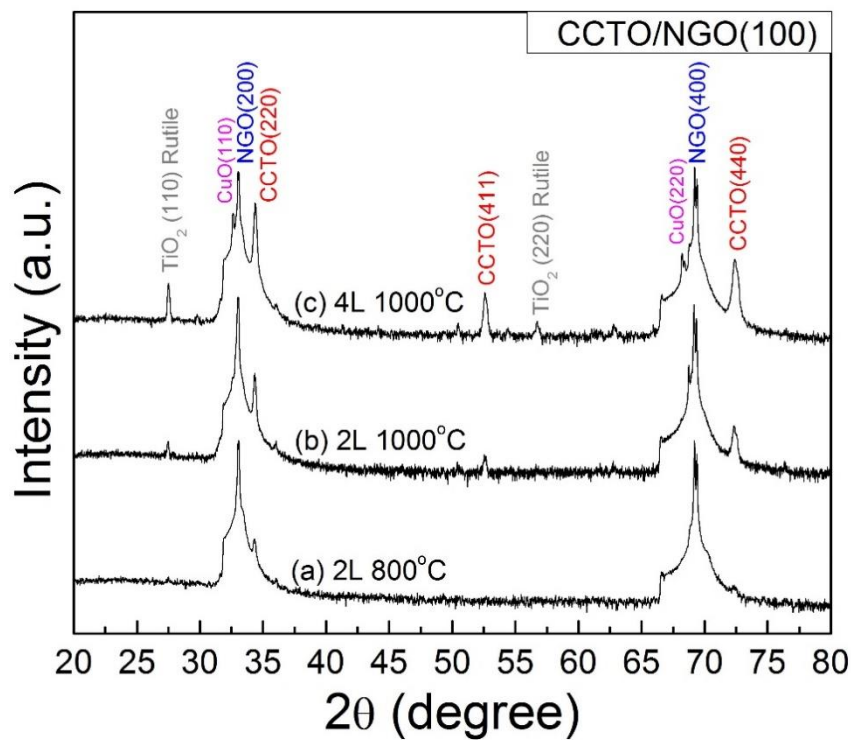
Figure 5.6: θ-2θ X-ray diffraction scan of CCTO films deposited on NGO(100) substrates annealed at 800 ℃ and 1000 ℃. (a) two-layered CCTO/NGO(100) film annealed at 800 ℃, (b) two-layered CCTO/NGO (110) film annealed at 1000 ℃, (c) four-layered CCTO/NGO(100) film annealed at 1000 ℃.
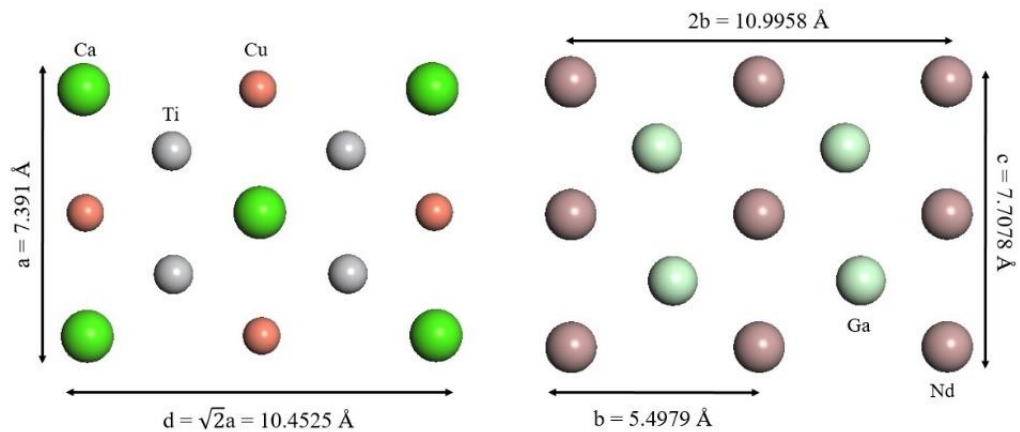
Figure 5.7: The cleaved CCTO (hh0) and NGO (h00) plane models illustrates atomic locations.

Figure 5.6 shows the XRD patterns of the CCTO films grown with different layers on NGO(100) substrates annealed at 800°C and 1000°C, respectively. As seen in Figure 5.6, the dominant (hh0) peaks consisting (220) and (440) reflections from CCTO layer are present in the spectrum next to the (100) and (200) peaks from NGO substrate, respectively. In other words, NGO (100) strongly influences the growth of the (hh0) peaks (220) and (440) of CCTO. However, there was an extra CCTO (441) peak indicating more than one orientation in this spectrum rather than owning the single phase of (hh0). Interestingly, the presence of a small amount of TiO_2 rutile phase seen from (110) and (220) peaks only exists for only the case of CCTO annealed at 1000°C. Some other works reported the existence of TiO_2 rutile phase which is a common phase found in CCTO films and ceramics [57]. There is no detectable TiO_2 rutile phase in the CCTO/NGO(100) films annealed at 800°C. This is consistent with the result from the

CCTO/LAO(100) films annealed at the same temperature. The intensity of TiO_2 reflections for CCTO/NGO(100) annealed at 1000ºC are stronger than that of CCTO/LAO(100) annealed at the same high temperature and grown with the same layer. From the discussion with Professor Dr. Jose H. Hodak concerning the appearing of the TiO_2 peaks as an impurity phase in CCTO films, he suggested that slightly imbalances in the composition of the sol-gel precursor solution are the most likely culpirit for the impurities. During the handing of the sol-gel precursor solution, and even at the moment of casting the films, exposure to moisture from the air causes some hydrolysis of the titanium alcoxide. As a result of this colloidal TiO_2 particle form which appear as a contamination in the films. Surprisingly, the reflections of CuO(110) and (220) for tenorite phase [58] in the films (2L and 4L) annealed 1000°C appeared at 32.51º and 68.12º, respectively nearby (100) and (200) diffracted peaks of NGO(100) substrates, respectively. The CuO phase occurs naturally around the grain boundaries of CCTO and it was readily observed in the films annealed at temperatures of 1000°C and higher [58]. In contrast, our EDX experiments did not confirmed that the grain boundary regions in our high temperature annealed films are richer in Cu than regions within grains. Then, it is noted that the substrate peak intensities are much higher than those of the films. Using the same algorithm for the lattice constant calculation, the highest (220) peak was used to calculate the lattice constant of CCTO film. The calculated lattice constant for the CCTO film on NGO(100) substrate is $a = 7.373$ Å ($a/2 = 3.686$ Å) while NGO has a pseudo cubic calculated lattice constant about $a = 3.86$ Å. Our first expectation is that the film grown on NGO is highly-oriented film similar to the film grown on LAO due to small lattice mismatch about 4.5% which is moderate and may induce the occurrence of lattice distortions in the CCTO films. For

sake of comparison, the work of Feng et al., showed that highly-oriented CCTO films may be grown on the SrTiO$_3$ (STO) substrates were actually in polycrystalline forms due to the large lattice mismatch between CCTO and STO(100) of about 5.7% [38]. Large lattice mismatch between CCTO and NGO(110) and NGO(100) could lead to sufficiently high strain energy that could be prevent the full epitaxial growth of CCTO. Moreover, NGO(100) substrate even with no twining defect like LAO substrate could induce more impurity phase like CuO beside TiO$_2$ at such high annealing temperature of 1000°C. Not only TiO$_2$ rutile phase but also CuO phase was found in the CCTO/NGO(100) film only annealed at 1000°C. Using the same analogous as above for justify the quality of preferential orientation of the CCTO/NGO(100) film, the (hh0) preferential orientation of the film is defined by using the relative intensity of (220) peak compared to that of (400) peak as shown the Eq. (5.2) below

$$\alpha_{(220)} = \frac{I_{(220)}^{film} / (I_{(400)}^{film} + I_{(220)}^{film})}{I_{(220)}^{powder} / (I_{(400)}^{powder} + I_{(220)}^{powder})} \qquad (5.2)$$

Since there are no (400) peaks observed in the CCTO/NGO(100) films, the $\alpha_{(220)}$ for all the films are the same value and equal to 1.41.

Table 5.1: The ratio of $\alpha_{(400)}$ and $\alpha_{(220)}$ orientations of CCTO.

	$\alpha_{(400)} = \dfrac{I^{film}_{(400)}/(I^{film}_{(220)}+I^{film}_{(400)})}{I^{powder}_{(400)}/(I^{powder}_{(220)}+I^{powder}_{(400)})}$	$\alpha_{(220)} = \dfrac{I^{film}_{(220)}/(I^{film}_{(400)}+I^{film}_{(220)})}{I^{powder}_{(220)}/(I^{powder}_{(400)}+I^{powder}_{(220)})}$
2L_CCTO/LAO(100) @800°C	3.36	-
2L_CCTO/LAO(100) @1000°C	3.04	-
4L_CCTO/LAO(100) @1000°C	3.19	-
2L_CCTO/NGO(100) @800°C	-	1.41
2L_CCTO/NGO(100) @1000°C	-	1.41
4L_CCTO/NGO(100) @1000°C	-	1.41
4L_CCTO/NGO(110) @800°C	3.38	-

When the (411) plane is referred for calculation instead of (400), the alpha value are the same again equal to 0.99. Thus, the same formula as written in the report [30] is just tried as followed by the ratio of I(220) to I(400) and I(411), the value ranged from small to big value are shown in the table 5.2.

Table 5.2: The ratio I(220)/I(411) and I(220)/I(400) of CCTO/NGO(100) [30].

Intensity Ratio	I(220)/I(411)	I(220)/I(400)
2L_CCTO/NGO(100) at 800°C	-	-
2L_CCTO/NGO(100) at 1000°C	68.324	1844.75
4L_CCTO/NGO(100) at 1000°C	103.790	6201.50
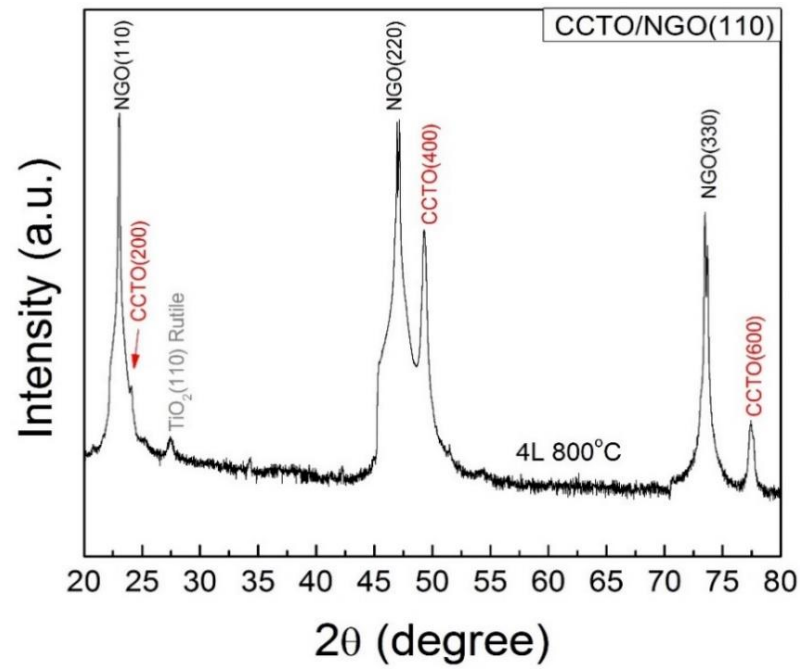
Figure 5.8: θ-2θ X-ray diffraction scan of four-layered CCTO films deposited on NGO (110) substrate annealed at 800 °C.
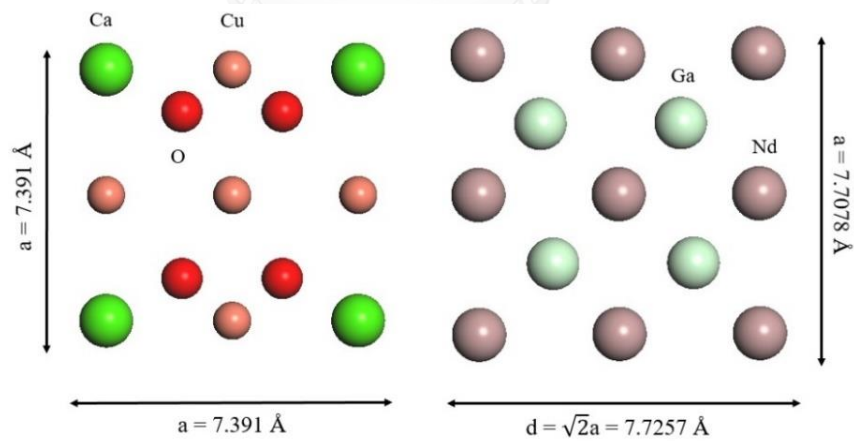
Figure 5.9: The cleaved CCTO (2h00) and NGO (hh0) plane models illustrates atomic locations.

In contrast with the CCTO film grown on NGO(110) as shown in Figure 5.8, the strong peaks were from (h00) planes including (200), (400) and (600). The CCTO film was deposited with four layers and each layer was annealed at 800°C. The X-ray diffraction pattern of the CCTO/NGO(110) indicated the perfect out of plane alignment in one direction. The intensity for (200) plane could not be clearly observed due to the overlapping with (110) diffraction peak from NGO. It was found that there was TiO_2 (110) rutile phase detected in the four-layered CCTO/NGO(110) film even annealed at 800°C. The main characteristic peak of the film deposited on Si substrate is (200) plane [34] which indicated the formation of CCTO polycrystalline while deposited on LAO(100) and NGO(110) the main characteristic peak is (400) plane. Similarly, the film grown on LAO(100) and NGO(110) showed the (600) plane with high intensity, however, the (600) for the film grown on Si could not be found. The obtained $\alpha_{(400)}$ for the 4L CCTO/NGO(110) film annealed at 800°C is 3.38 which is confirmed for (400) preferential oriented CCTO film and comparable to the value of 3.36 which belonged to the 2L CCTO/LAO(110) film annealed at 800°C. The effect of the layer thickness and thermal annealing temperatures on the surface morphology of CCTO films grown on different types of single crystal substrates was investigated using FE-SEM and AFM techniques. The average thickness of CCTO thin films per single layer grown on LAO and NGO are approximately 100 nm. The film surface of all films is crack-free and quite smooth with some tiny holes. It is certain that there are two different areas, (1) and (2), showing different surface morphologies observed in all CCTO films. As seen in Figure 5.10 (b) and (d) in area (1), the grain sizes of CCTO thin films deposited on LAO(100) and NGO(100) for annealing at 800°C are approximately 40-55 nm compared to 100-200 nm grain size in area (2). For the two-layered CCTO films

annealed at 800 °C (Figure 5.10 (a)-(d)), area (1) showed smaller grains with a combination of 200 nm long rod-like and elliptical shapes while area (2) showed bigger grains with mostly square and rectangular shapes. According to the corresponding cross section images, there are some voids and pores appeared in the film cross section which could be possibly produced by solvent evaporation during preheat and annealing process and by organics burning during heat treatment [35]. The porous structure is seen more often when the annealing time is too short and the temperature is too low. Thus, considerable densification occurs during annealing. The two-layered CCTO films annealed at 1000°C (Figure 5.11 (e)-(h)) showed many square and rectangle shaped grains stacking onto each other, which is consistent with the XRD patterns indicating certain preferential orientation. At the annealing temperature of 1000°C, the thermal energy causes coalescence of the rectangular clusters into larger crystals. During this process, the CCTO films became denser and richer in column-like domains, with a sharper interface between the CCTO film and the substrate. At such high annealing temperature of 1000°C, the CCTO films grown on both types of substrate appear to have better crystallization on the surface. The plane views of FE-SEM images for higher magnification are presented in the insert of Figure 5.12 (a) and (c).
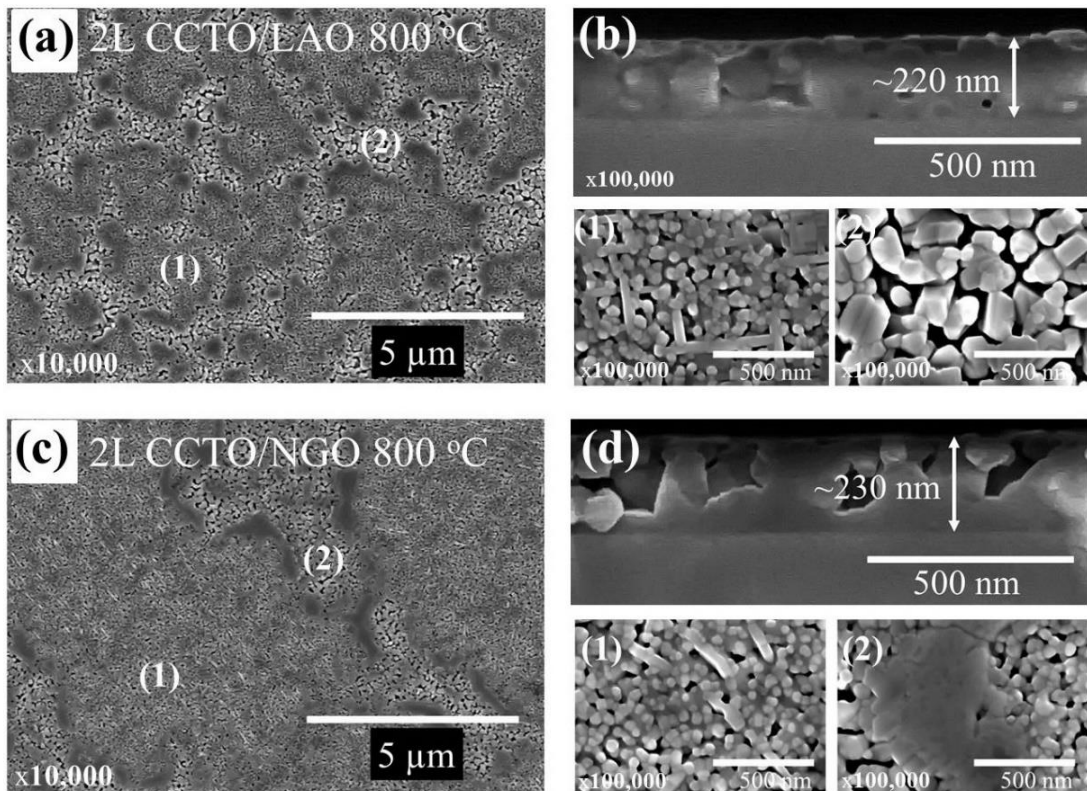
Figure 5.10: FESEM images of two-layered CCTO films (a) Plane view of CCTO/LAO(100) film annealed at 800 ℃ and (b) the corresponding cross section and the zoom in of area (1) and (2), (c) Plane view of CCTO/NGO(100) film annealed at 800 ℃ and (d) the corresponding cross section and the zoom in of area (1) and (2).
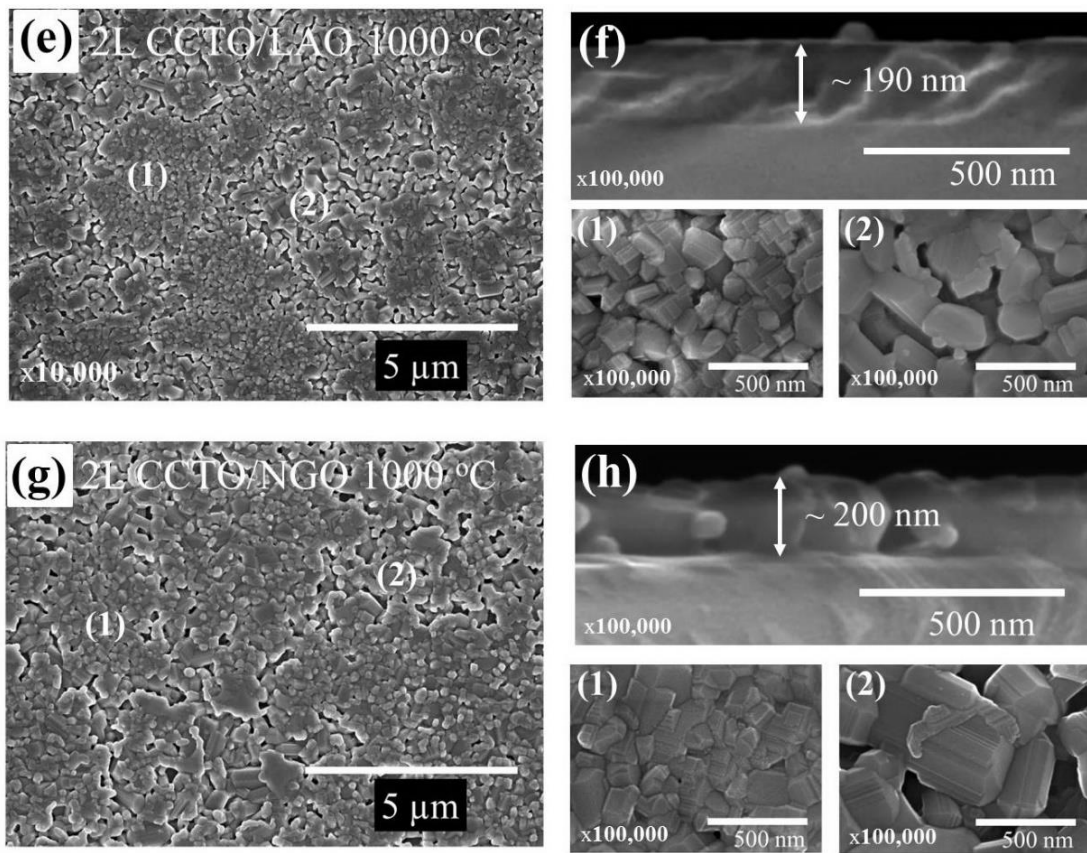
Figure 5.11: (e) Plane view of CCTO/LAO film annealed at 1000 ℃ and (f) the corresponding cross section and the zoom in of area (1) and (2), (g) Plane view of CCTO/NGO film annealed at 1000 ℃ and (h) the corresponding cross section and the zoom in of area (1) and (2).
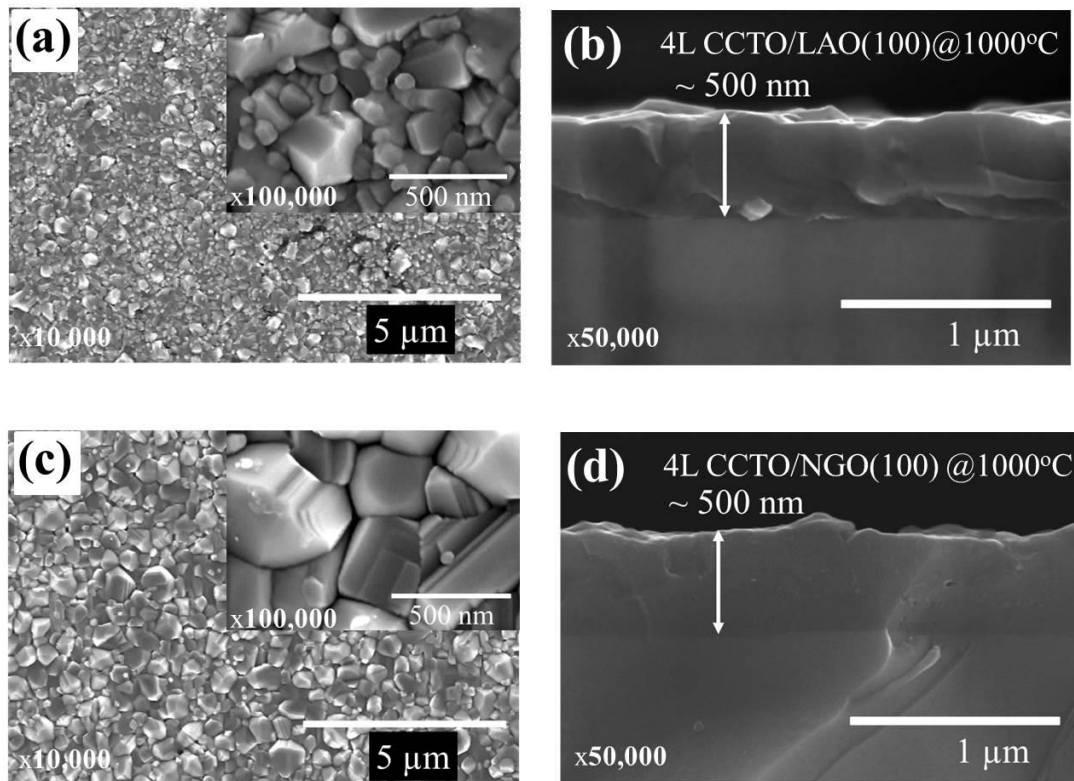
Figure 5.12: FESEM images of four-layered CCTO films (a) Top view of CCTO/LAO(100) film annealed at 1000 ℃ and (b) the corresponding cross section, (c) Top view of CCTO/NGO(100) film annealed at 1000 ℃ and (d) the corresponding cross section.

The surface morphologies of CCTO thin films observed by tapping mode AFM measurements are shown in Figure 5.13-5.16. Analysis of the surface roughness and average grain size was carried out by Gwyddion 2.41 free software. The surface morphology was obtained using an area of 1x1 μm^2. All the films yielded homogeneous microstructures consisting of small and large grains. Comparison among the films grown on the same type of substrates with the same annealing temperature of 800 °C, the grain sizes of two layered films are smaller than that of four layered films. Obviously, the results show that the average grain size increases with the number of layers and with the annealing temperature which is consistent with the results from FE-SEM images. As the film thickness increased from ~250 nm to ~500 nm, the average cluster height and size increased, the surface roughness increased contributing from the more mixture of large and small grains. The root mean square (RMS) roughness for 2L CCTO/LAO(100) annealed at 800°C and 1000°C is 14.58 nm, 16.95 nm, respectively and for the four layered sample annealed at 1000°C is 18.59 nm. The root mean square (RMS) roughness for 2L CCTO/NGO(100) annealed at 800°C and 1000°C is 13.54 nm, 22.34 nm, respectively and for the four layered sample annealed at 1000°C is 21.25 nm. The surface roughness seems to be comparable among the films deposited on the same type of substrates but for deposited on NGO the roughness of the films are a little bigger than that of deposited on LAO. In this work, dielectric constants of film capacitors having interdigitated electrode configuration were determined based on an analytical method derived by Fernell et al. [56].

The values of room temperature dielectric constant and loss tangent measured at 1 MHz of all studied films are shown in Table 5.6-5.9. All films were grown with the approximately the same thickness of 400-500 nm. It was concluded that CCTO/NGO(100) obtained the highest dielectric constant and corresponding the highest loss tangent whereas the CCTO/LAO(100) and CCTO/NGO(110) showed the same moderate high dielectric constant values.

Table 5.3: The value of dielectric constant and loss tangent of all films at 100 kHz with no bias voltage.

Measured at 1 MHz	CCTO/LAO(100) (400nm)	CCTO/NGO(110) (400nm)	CCTO/NGO(100) (400nm)
ε_r	~1040	~1020	~2540
tan (δ)	~0.0496	~0.0185	~0.0825
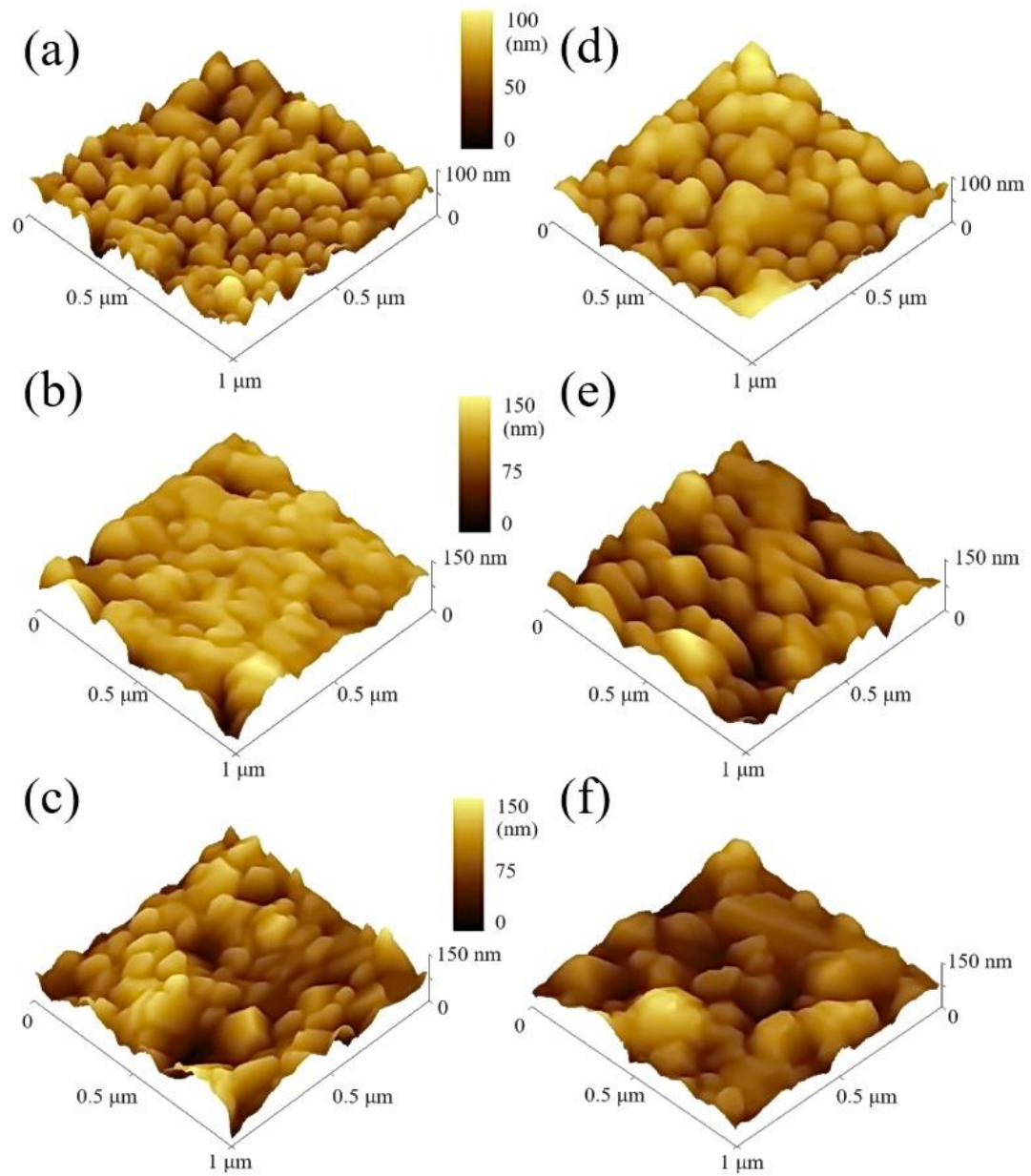
Figure 5.13: AFM images (1x1 μm^2) in 3D of the CCTO films deposited on single crystal substrates. (a) Two-layered on LAO annealed at 800 ºC, (b) Two-layered on NGO annealed at 800 ºC, (c) Two-layered on LAO annealed at 1000 ºC, (d) Two-layered on NGO annealed at 1000 ºC, (e) Four-layered on LAO annealed at 1000 ºC, (f) Four-layered on NGO annealed at 1000 ºC.

5.3 The characterizations of Fe doped CCTO grown on alumina (Al_2O_3) substrates
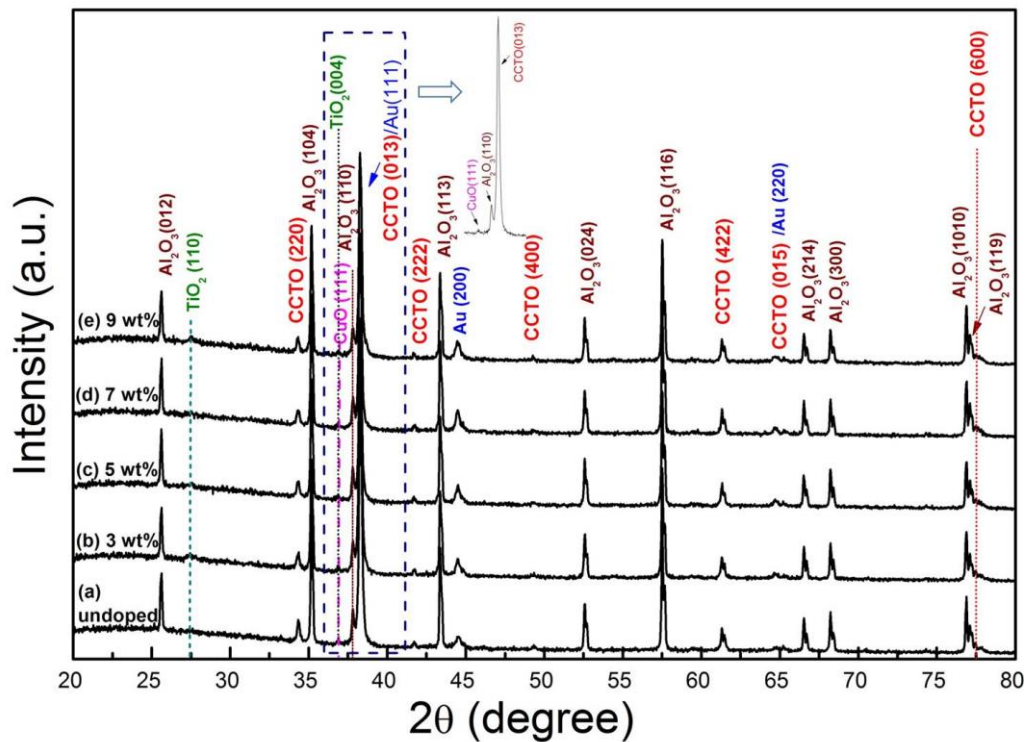
Figure 5.14: X-ray diffraction patterns of Fe-doped CCTO films grown on alumina substrates.

The diffraction patterns of Fe-doped CCTO films deposited on alumina substrates were presented in Figure 5.14. It was seen that all samples were highly crystalline and contain several phases from the substrate and sensing films. The substrate, which was equipped with interdigitate gold electrodes, gave rise the dominant diffraction peaks of Al_2O_3 phase and small Au peaks on (200) and (220) planes while the sensing films contained three material phases. The main phase in sensing films exhibited evident diffraction peaks, which could be identified to be (220) (013) (222)

(400) (422) and (015) planes of CCTO cubic perovskite phase (JCPDS 21-0140). The lattice constant of CCTO cubic thin films calculated by Bragg's expression on (220) plane was 7.376+/-0.003 Å, which was slightly lower than that for of bulk CCTO (7.391 Å). In addition, it could be noticed that the diffraction peaks for Fe-doped CCTO films were relatively low and broad compared to those for undoped films, suggesting that the CCTO grains of Fe-doped films were smaller than that of undoped one. Moreover, two minor phases, including rutile TiO_2 and cubic CuO were also found in all films. However, no iron or iron oxide phase could be detected in all Fe-doped films up even at the highest doping level of 9 wt% [59]. The absence of Fe peaks suggested that Fe might form solid solution with CCTO matrix or the crystallite of Fe phase was very small. Figures 5.18 (a) and (b) showed the EDX spectra of 0 and 9 wt% Fe-doped CCTO films, respectively. The spectra confirmed the presence of calcium (Ca), copper (Cu), titanium (Ti), and oxygen (O) in both films and iron (Fe) only in the doped film. The Fe concentrations of all CCTO films were estimated from EDX spectra and plotted as a function of the concentration of iron in the sol-gel precursor solutions as displayed in Figure 5.15 (c). It was evident that the iron concentration in the film increased linearly with increasing iron concentration in the precursor solution. The slope represented the efficiency of the iron incorporation from the solution into the film. In the range of compositions studied, nearly 70% of the iron in the precursor solution was incorporated into the films. This suggested that some of iron atoms might precipitate out of the precursor solution before the film deposition step. However, the linear trended shown in Figure 5.15 (c) indicates that the iron doping efficiency was nearly the same for all iron compositions.

Table 5.4: The stoichiometry of undoped and Fe-doped CCTO on silicon substrates with different concentration in both of percent by weights and atoms.

Elements/Weight%	Undoped	3% Fe doped	5% Fe doped	7% Fe doped	9% Fe doped
O	42.58	40.39	40.73	44.93	40.40
Ca	6.40	6.44	5.90	4.15	3.23
Ti	30.11	36.36	38.13	30.88	37.32
Fe	0	2.10	3.43	4.23	6.31
Cu	20.91	14.70	11.81	15.81	12.74

Elements/Atomic%	Undoped	3% Fe doped	5% Fe doped	7% Fe doped	9% Fe doped
O	70.42	67.99	68.14	72.36	68.28
Ca	4.23	4.33	3.94	2.66	2.18
Ti	16.65	20.44	21.31	16.61	21.07
Fe	0	1.01	1.64	1.95	3.05
Cu	8.71	6.23	4.97	6.41	5.42
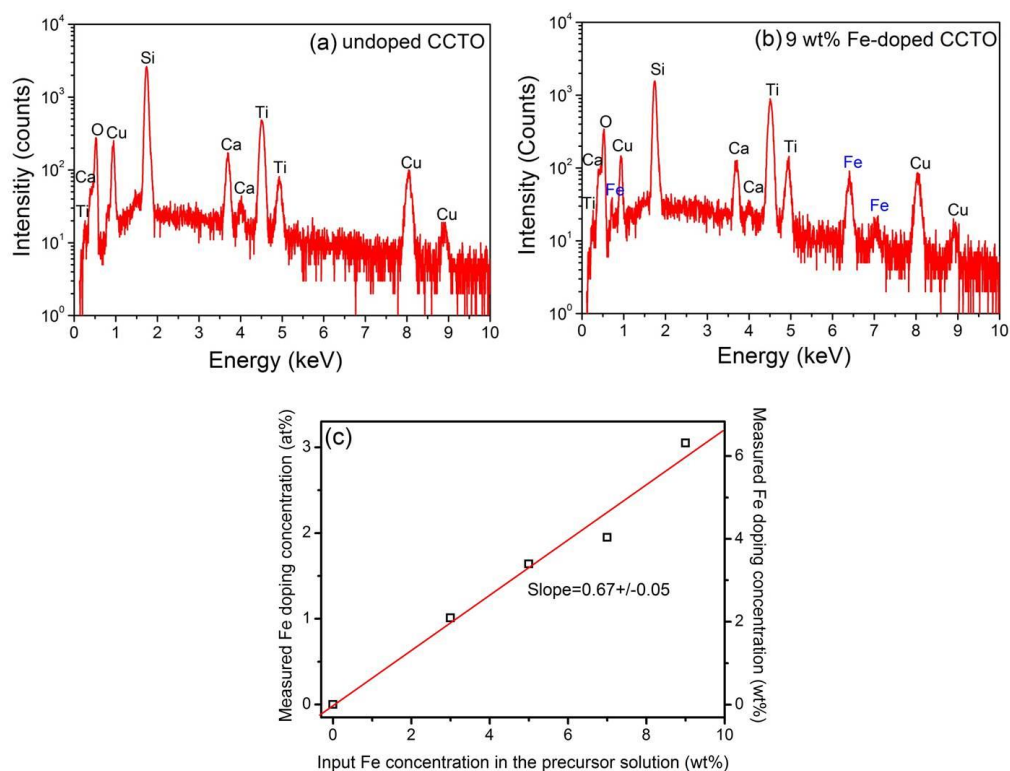
Figure 5.15: The EDX spectra of (a) undoped CCTO and (b) 9 wt% Fe-doped CCTO thin films and (c) the plot of measured Fe doping concentration of Fe in precursor solutions.

Raman spectroscopy was used to gain further insight into the composition and the structure of the Fe-doped CCTO films. Figure 5.16 showed the Raman spectra for undoped and 9 wt% Fe-doped CCTO films. The most dominant Raman shifts at 445 and 509 cm^{-1} could be associated with Ag symmetry rotation-like vibration of the TiO$_6$ (Titanium octahedral structure) and a very board signal at 577 cm^{-1} could be assigned to antistretching of Ti-O-Ti bonding with Ag symmetry. The board peak at ~750 cm^{-1} might be attributed to the symmetric stretching-breathing mode of the TiO$_6$ cage [6]. The weak peaks at 221 cm^{-1} and 246 cm^{-1} might correspond to the bending vibration

mode of (O-Ti-O) in $CaTiO_3$ [60]. These were the characteristic Raman active modes found in CCTO [61]. With Fe doping, the primary Raman peaks of CCTO were still observed with no significant shift. This result was in contrast to the previous report of NiO-doped CCTO [12]. The secondary peak at 608 cm^{-1} was consistent with the presence of a small amount of TiO_2 rutile phase [62] and the minor band at 282 cm^{-1} might arise from the Ag phonon mode in a monoclinic structure of CuO phase [6]. In addition, it could be observed that Raman signatures for CuO and TiO_2 of the Fe-doped film were slightly more pronounced than those of the undoped CCTO. The presence of these secondary phases (CuO and rutile TiO_2) was consistent with the signatures previously observed in the XRD patterns (Figure 5.14). The absence of the characteristic signals for α-Fe_2O_3 phase of iron oxides (A_{1g} modes at 228 cm^{-1} and 497 cm^{-1} and E_g modes at 247 cm^{-1}, 294 cm^{-1}, 412 cm^{-1} and 612 cm^{-1}) confirmed that Fe_2O_3 phases were not present in Fe-doped CCTO films [59].

FESEM micrographs of CCTO films with different Fe doping concentrations were shown in Figure 5.17 (a)-(e). It was seen that all films have typical polycrystalline morphology with nanometer-size grains and contained voids between grains, whose size and density depended considerably on Fe doping.
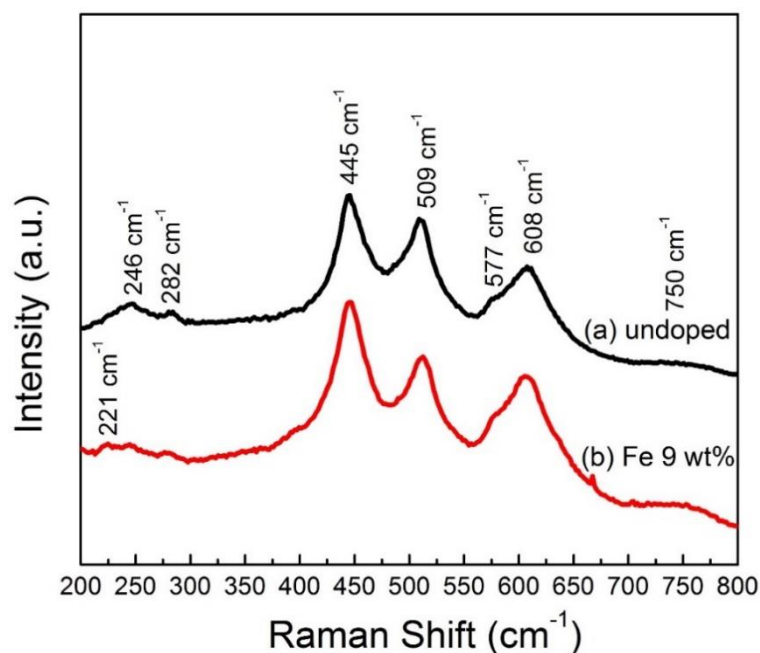
Figure 5.16: Raman spectra for CCTO and 9 wt% Fe-doped CCTO films.

The undoped CCTO film had relatively large grains and high void density. The grains were mostly elliptical with the mean width and length of ~100 nm and ~250 nm, respectively, while the voids were relatively small with varying diameters in the range of 10-30 nm. With Fe doping, grains became smaller and more uniform with the mean grain size ranging between 30 and 50 nm and the void density was also lower than that for undoped CCTO but the grain size and void density were not greatly varied with Fe-doping concentration. This was in accordance with the slight CCTO peak broadening observed in the XRD patterns of Fe-doped CCTO films. Figure 5.17 (f) showed a typical cross-sectional view of a Fe-doped CCTO film on alumina substrate. It could be seen that the film was porous with a number of voids going all the way down to the substrate. In addition, the film surface was much smoother than that of Al_2O_3 substrate and the film thickness was considerably varying between 550 and 800 nm.
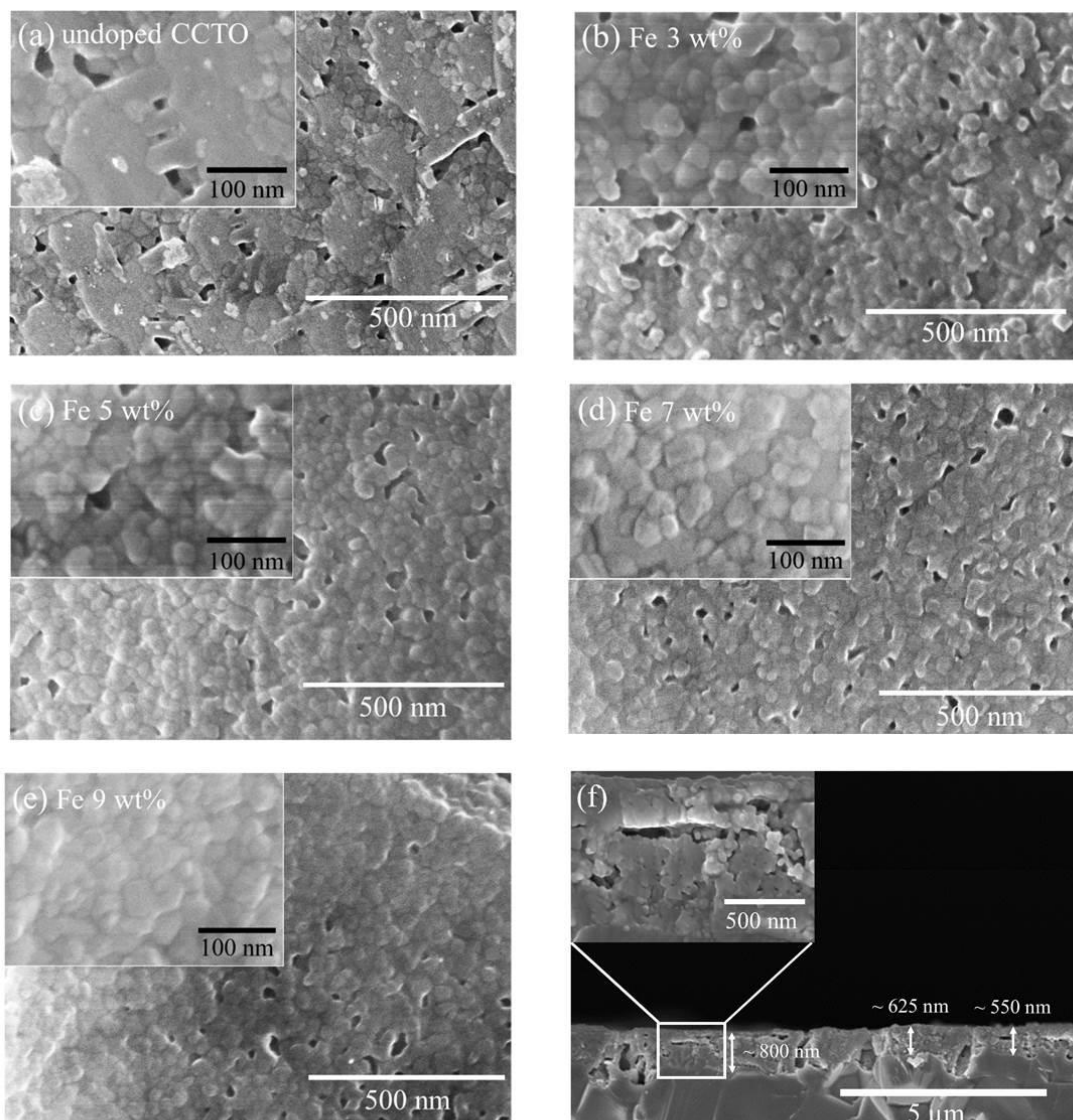
Figure 5.17: FESEM surface images at x100,000 of CCTO films annealed at fixed temperature 800 °C (a) undoped, (b) 3 wt% Fe, (c) 5 wt% Fe, (d) 7 wt% Fe, (e) 9 wt% Fe, (f) typical cross section of CCTO thin film on alumina substrates. The inserted photographs (a) to (e) show a high magnification at x200,000.

The type of doping (i.e. p-type or n-type) depended on the oxidation state of dopant and it was crucial for the understanding of the working mechanism of the sensors. Thus, the oxidation states of the elements present in the doped films were further confirmed by XPS measurements. Figure 5.18 (a) showed a typical XPS survey spectrum for a Fe-doped CCTO film, which contained all expected elemental peaks including O 1s, Ca 2p, Cu 2p, Ti 2p and Fe 2p that were further examined with high-resolution scans as demonstrated in Figures 5.19 (b) to 7 (f), respectively. The O 1s signal (Figure 5.20 (b)) could be decomposed into two Gaussian peaks at binding energies of 529.5 and 531.0 eV, which might be assigned to the lattice oxygen (O^{2-}) and the chemisorbed oxygen species on the surface (O_2^-), respectively [63]. The Ca 2p core level spectrum (Figure 5.19 (c)) comprised the spin doublets of Ca $2p_{3/2}$ and Ca $2p_{1/2}$ at 346.9 and 350.5 eV, which corresponded to the typical Ca^{2+} oxidation state. For the core level of Cu 2p (Figure 5.18 (d)), the spin orbit doublets of Cu $2p_{3/2}$ and Cu $2p_{1/2}$ consisted of the main peaks at 933.9 and 954.0 eV and satellite peaks at 942.2 and 962.2 eV, respectively, which could be all associated with the Cu^{2+} oxidation state [64]. The XPS spectrum of Ti 2p (Figure 5.19 (e)) consisted of Ti $2p_{1/2}$ and Ti $2p_{3/2}$ doublet peaks at binding energies of 464.2 and 458.4 eV, respectively, which were consistent with the reported values for Ti^{4+} of TiO_2 [65, 66]. In the case of the core level of Fe 2p (Figure 5.18 (f)), the spin doublets of Fe $2p_{3/2}$ and Fe $2p_{1/2}$ also contained the main peaks at 711.8 and 725.1 eV and satellite bands at 718.1 and 732.7 eV, respectively, which could be completely assigned to the Fe^{3+} oxidation state [67, 68]. The XPS result confirmed that all the iron incorporated into the CCTO films was present as Fe^{3+} state since there was no Fe^{2+} component, which would display $2p_{3/2}$ and $2p_{1/2}$ peaks at 709 eV and 722 eV, respectively [67].
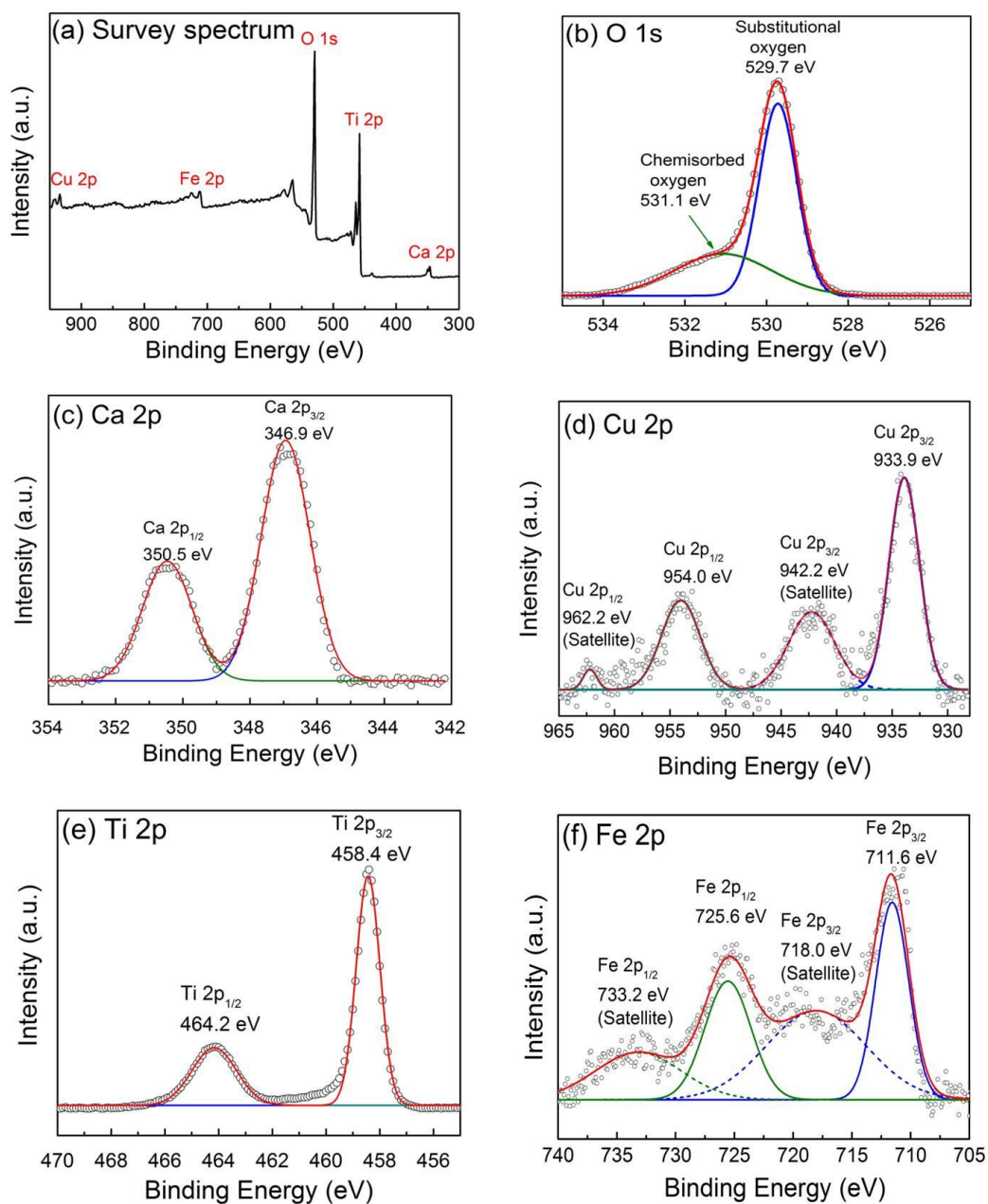
Figure 5.18: X-ray photoelectron spectra (XPS) of (a) Survey spectrum, (b) O 1s, (c) Ca 2p, (d) Cu 2p, (f) Ti 2p, and (f) Fe 2p core levels for Fe-doped CCTO films.

5.4 Gas sensing performance and mechanism of undoped and Fe doped CCTO thin films on alumina substrates

H_2S gas-sensing properties of undoped CCTO and Fe-doped CCTO sensors were characterized at various operating temperatures in the range of 150–350°C and concentrations ranging from 0.25 to 10 ppm. Figure 5.21 illustrated the change in resistance of the CCTO films with different Fe doping concentration under exposure to various H_2S pulses at different concentrations at an operating temperature of 250 °C which showed the best result of sensing response. It could be seen that the baseline resistance of CCTO film increased monotonically by around one order of magnitude with increasing input Fe concentration from 0 to 9 wt% (0 to ∼3 at%). Similar trend of baseline resistance was observed at other operating temperatures. The result might be explained by the p-type doping effect to be discussed later in the next section. Upon exposure to H_2S, the resistance of all CCTO sensors rapidly decreased which confirmed a typical n-type semiconducting behavior towards a reducing gas. In addition, the resistance change of CCTO sensor tended to increase substantially with increasing input Fe-doping concentration from 3 to 9 wt% (∼1 to ∼3 at%). Figure 5.21 (a) demonstrated the sensor response of all CCTO sensors to 10 ppm H_2S at operating temperature ranging from 150 to 350 °C. It was seen that the H_2S responses of CCTO sensors initially increased with increasing operating temperature to reach optimum values and then decreased as the operating temperature increases further. Additionally, the optimal operating temperature depended on the Fe-doping level. The optimal operating

temperature for undoped and 3-7 wt% ($\sim$1$-$2 at%) Fe-doped CCTO sensor was around 300 °C and it was reduced to 250 °C at the highest input Fe-doping concentration of 9 wt% ($\sim$3 at%). Thus, the operating temperature tended to improve with increasing Fe-doping level. Moreover, the sensor response at a given temperature also tended to increase with increasing Fe-doping concentration. In particular, the largest improvement was seen near the optimal operating temperature when the input Fe-doping level increased from 7 wt% to 9 wt% ($\sim$2 to $\sim$3 at%). Therefore, Fe dopants played an important role in the enhancement of the sensor response toward H_2S. Figures 5.21 (b)-(d) displayed the H_2S sensing characteristics in terms of sensor response, response time and recovery time of all CCTO sensors as a function of H_2S concentration at the optimal operating temperature of 250 °C. It could be seen that the response of each sensor initially increased quite linearly with increasing H_2S concentration and tended to saturate at high H_2S concentration (3$-$10 ppm), conforming to the power-law behavior with the exponent value lower than one. In particular, the 9 wt% ($\sim$3 at%) Fe-doped CCTO sensor exhibits the highest response of $\sim$126 to 10 ppm H_2S, which was more than one order of magnitude higher than that of undoped CCTO at the optimum operating temperature. At a low H_2S concentration of 0.5 ppm, the sensor still exhibited a moderate response of $\sim$5.4, yielding a low H_2S detection limit of $\sim$0.05 ppm (predicted at the response of 1.05 based on the power-law relationship).
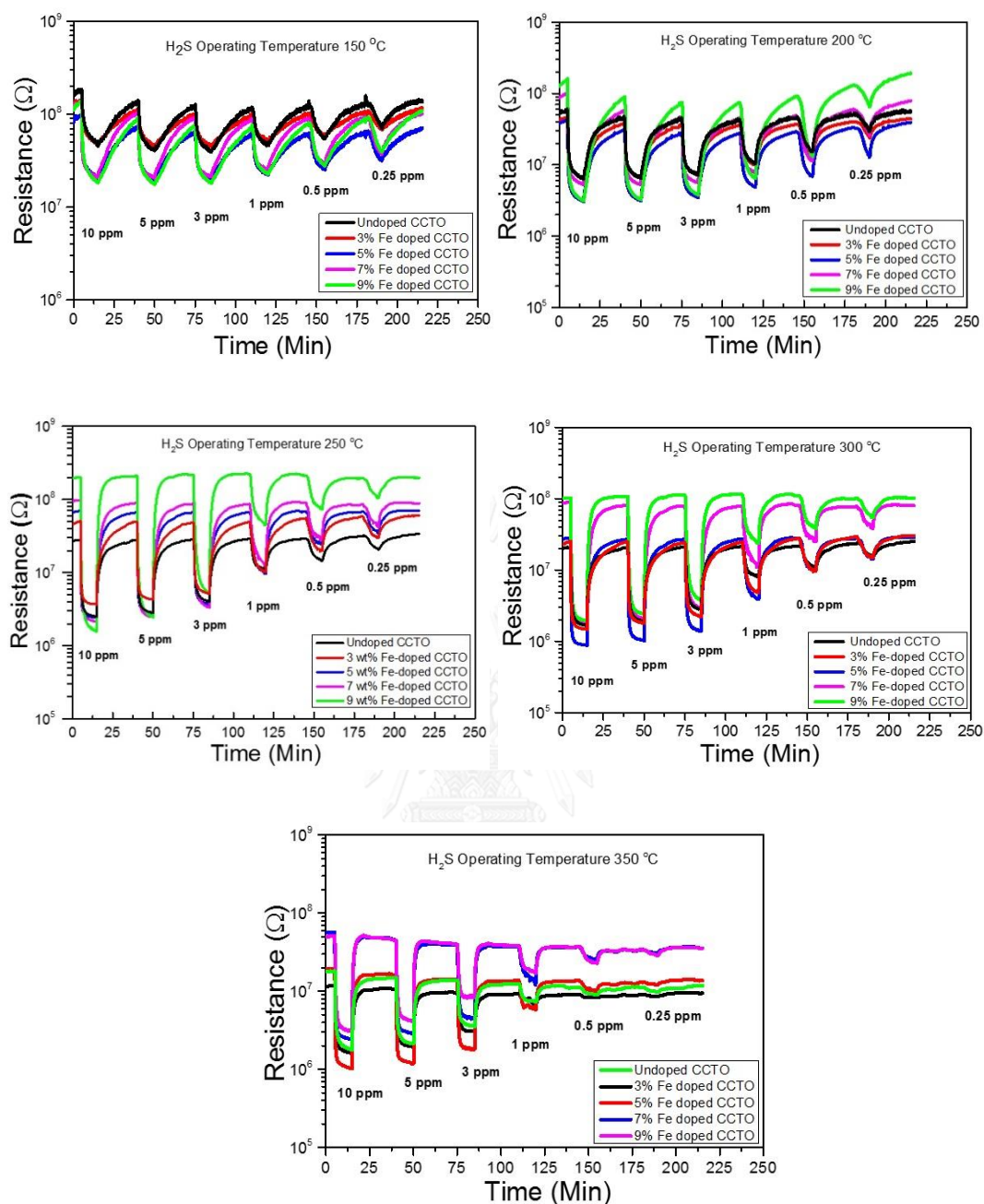
Figure 5.19: Change in resistance of the CCTO films with different Fe doping concentration under exposure to various H₂S pulses at different concentrations at an operating temperature of 150-350 °C.

Moreover, Fe doping at the high input concentration of 9 wt% (~3 at%) substantially improved H_2S response as well as response and recovery times at all gas concentrations (Figures 5.20 (c)-(d)). At high H_2S concentration of 10 ppm, the response time decreases from ~40 s to ~8.5 s and the recovery time reduced from ~1100 s to ~500 s as the input Fe-doping level increased from 0 to 9 wt% (0 to ~3 at%). As the gas concentration decreased, the response time quickly increased due to slower gas adsorption dynamic while the recovery time slowly decreased because of less amount of gas desorption. From overall results, the decrease of sensing time with Fe doping could be an indication of catalytic effect of Fe in CCTO.

The selectivity of CCTO sensors were assessed towards H_2S, NH_3, NO_2, C_2H_5OH, CO, CH_4 and C_2H_2 at their nominal concentrations and the optimal operating temperature of 250 °C as shown in Figure 5.21. It was seen that the undoped sensor shows relatively high response to H_2S moderate responses to C_2H_5OH and CH_4 and much less responses to other gases, displaying good H_2S selectivity against these gases. As Fe doping level increases from 0 to 3 wt% (0 to ~1 at%), responses to H_2S, NO_2, CO and C_2H_5OH slightly increased while those of other gases slightly decreased or remained approximately the same. Thus, the H_2S selectivity against these gases was not much affected. With further increase of Fe-doping level to 5 wt% (1.64 at%), responsed to H_2S increases considerably while those to all other gases also increased but with much lower relative increments. Hence, the H_2S selectivity against various gases were improved notably. As the input Fe-doping concentration increased from 5 to 9 wt% (1.64 to ~3 at%), response to H_2S increases substantially while those of other gases only slightly increased or decrease. Hence, the H_2S selectivity against various gases were improved greatly with the high Fe-doping level. Therefore, Fe dopants effectively

enhanced the sensor response and selectivity towards H₂S. Lastly, the reproducibility and stability of sensors were evaluated. Five sensors from the same batch of testing showed fair response variation of less than 30% and the sensors exhibited good stability with less than 25% of baseline and response shifted after three months of operation.
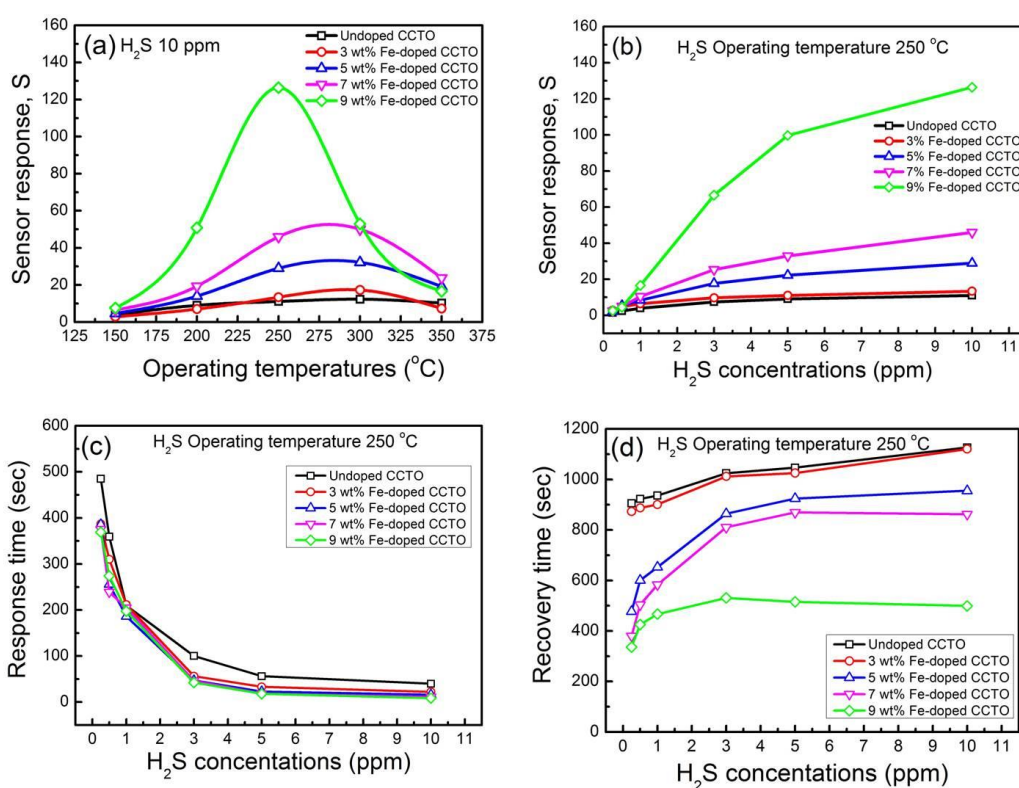
Figure 5.20: (a) Sensor response towards 10 ppm H_2S as a function of operating temperature, (b) sensor response, (c) response time and (d) recovery time as functions of H_2S gas concentrations for CCTO sensors with different Fe doping concentrations.
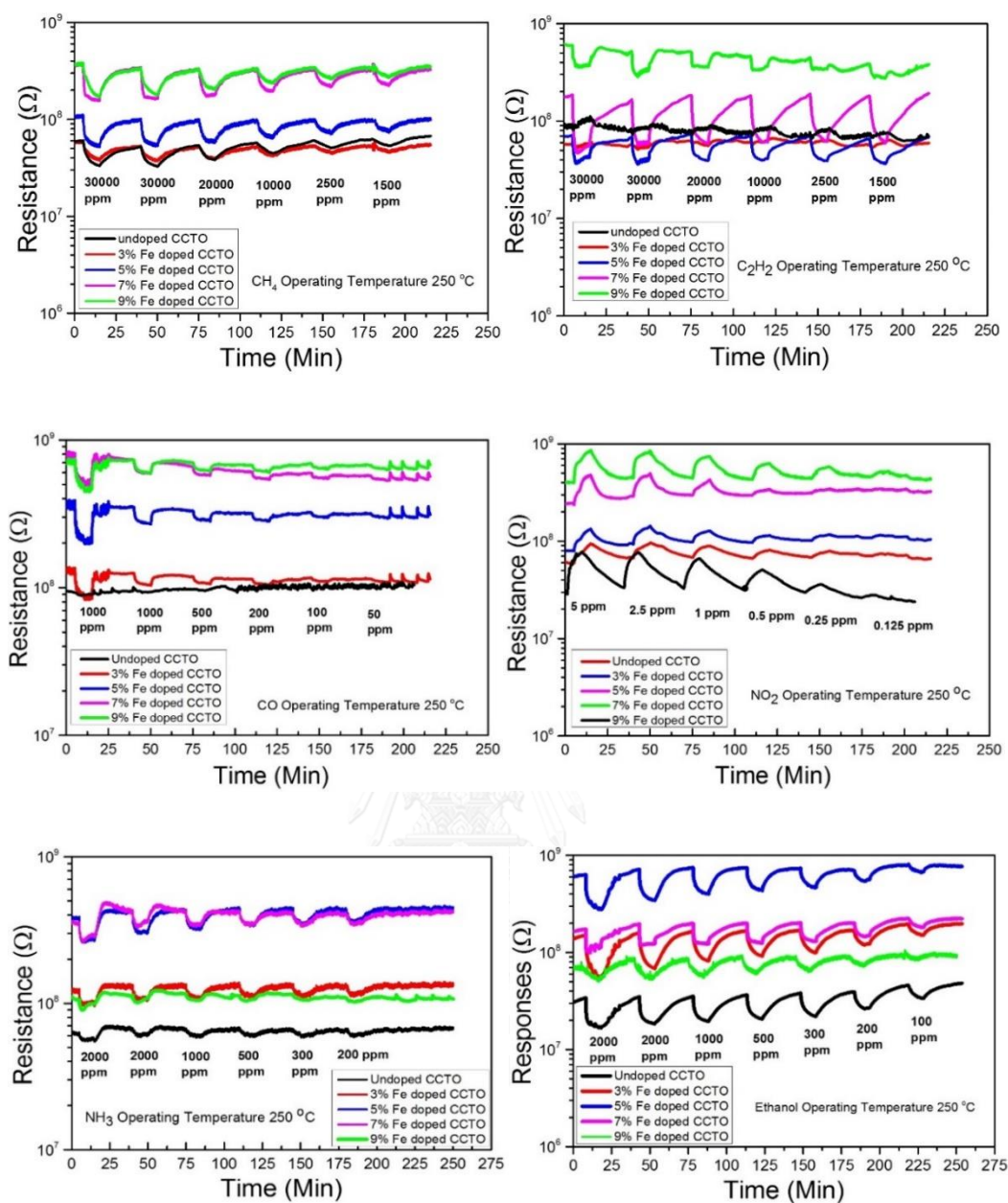
Figure 5.21: Change in resistance of the CCTO films with different Fe doping concentration under exposure to various C_2H_2, CH_4, CO, NO_2, NH_3, and Ethanol pulses at different concentrations at an operating temperature of 250 °C.
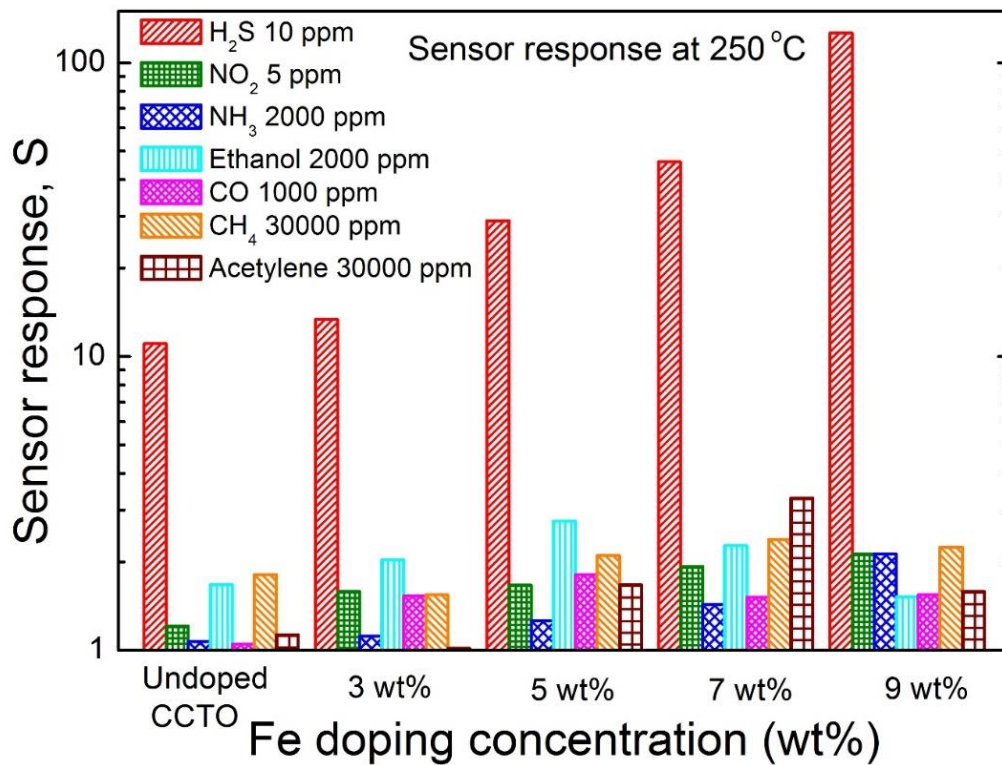
Figure 5.22: Selectivity histogram of CCTO sensors with different Fe-doping concentrations.

In comparison with other recently reported metal oxide materials [69-77] as listed in Table 5.5, the Fe-doped CCTO thin film exhibited relatively high response at the same or lower H_2S concentration except the cases of 2 wt% Pt doped α-Fe_2O_3 nanoparitcles [72] and 0.5 wt% Rudoped WO_3 nanorods [77] which offered higher response of 147−192 at 10 ppm. In addition, it displayed a relatively low optimal operating temperature compared with some other materials including CuO-NiO core-shell microspheres [74], 0.03 wt% Au-doped WO_3 nanoparticles [75], α-MoO3/ZnO composite [76] and 0.5 wt% Ru-doped WO_3 nanorods [77] while other nanostructure materials had lower optimal operating temperatures (110−160°C) and 1 at% Au modified ZnO nanowires could operate at room temperature [69]. Thus, the sol-gel Fe-doped CCTO sensor offered decent H_2S-sensing performances comparable with several advanced nanostructure materials despite its thin film form, which was expected to have relatively small specific surface area. The results suggested that Fe-doped CCTO surface was highly active and significant further enhancement of H_2S sensing performances might be achieved if CCTO nanostructures with very large surface area could be fabricated. The preparation of Fe-doped CCTO nanostructures was currently under development and might be reported elsewhere.

Table 5.5: Gas-sensing response of recently reported metal oxide sensors towards H_2S.

Materials	Methods	Temperature (°C)	Concentration (ppm)	H_2S response	Reference
1 at% Au modified ZnO Nanowires	Hydrothermal	25	5	80	N.S. Ramgir et al. 2013 [65]
5 wt% MoO_3/reduced graphene oxide	Microwave-hydrothermal	110	40	60	D. Li et al. 2015 [66]
Mg-doped In_2O_3 nanotubes	Electro-spun	150 250	10	173 23.87	C. Zhao et al. 2015 [67]
2 wt% Pt doped α-Fe_2O_3 nanoparitcles	Powder coprecipitation	160	100 10	325 147.7	S. Wu et al. 2007 [68]
2 wt% Ag-doped α-Fe_2O_3 nanoparitcles	Chemical coprecipitation	160	100	220	S. Wu et al. 2008 [69]
CuO-NiO core-shell microspheres	Hydrothermal	260	100	47.6	S. Ruan et al. 2015 [70]
0.03 wt% Au-doped WO_3 particles	Screen printing	300	2	12.4	C.O.Park et al. 2014 [71]
α-MoO_3/ZnO composite	Hydrothermal	270	100	30	Y.J. Chen et al. 2012 [72]
0.5 wt% Ru-doped WO_3 nanorods	Hydrothermal	350	10	192	V. Kruefu et al. 2015 [73]
9 wt% Fe-doped $CaCu_3Ti_4O_{12}$ thin film	Sol-Gel	250	10 5	126 100	This work

5.5 Gas sensing mechanisms

From the results, Fe dopants greatly enhance the sensor response and selectivity to H$_2$S. The roles of Fe-dopant on gas-sensing mechanisms of CCTO sensor may be explained based on electronic and catalytic effects of substitutional p-type Fe dopants. With no Fe doping, the undoped CCTO exhibits n-type semiconducting behaviors with a moderate conductivity at an elevated temperature due to structural defects particularly oxygen vacancies that generate electrons in conduction band according to the defect reaction represented in Kröger-Vink notation as:

$$O_o^x \rightarrow V_o^{\bullet\bullet} + 2e' + \tfrac{1}{2}O_2 \qquad (1)$$

Where O_o^x, $V_o^{\bullet\bullet}$, e' and O$_2$ are oxygen site, oxygen vacancy with double positive charge, electron with a single negative charge and oxygen gas, respectively. Near surface, the CCTO structure interacts with oxygen gas at the operating temperature forming various chemisorbed oxygen ions (O$^-$ and O^{2-}) that capture electrons from the conduction band. These processes lead to band bending, potential barrier and depletion regions on surface as well as nanocrystal interfaces. At sufficiently high temperature, some of adsorbed oxygen ions can migrate into the bulk and interact with oxygen vacancies in the lattice. Conversely, oxygen ions from the lattice can also react with an oxidizing gas to form

oxygen atoms on the surface. With Fe doping, Fe^{3+} ions may substitute Ti^{4+} sites, resulting in the creation of hole charge carriers according to the reaction [63]:

$$Fe_2O_3 \rightarrow 2Fe_{Ti}^{'} + 2h^{\bullet} + 2O_o^x + \tfrac{1}{2}O_2 \qquad (2)$$

where Fe_2O_3, $Fe_{Ti}^{'}$ and $h^{\bullet}$ are the quasi-Fe_2O_3 dopant molecule, Fe-Ti substitutional site with a single negative charge and hole with a single positive charge, respectively. The generated holes will recombine with existing electrons, leading to the annihilation of electrons and the increase of electrical resistance. The annihilation of electrons by Fe dopants will also lead to the expansion of electron depletion region on surface and grain interface as oxygen species must acquire electrons deeper into the bulk. The explanation based on Fe-Ti substitution is in accordance with the hypothesis based on XRD and XPS analyses. If the generated hole concentration exceeds the electron concentration of undoped CCTO, the CCTO will become p-type semiconductor and electrical resistance will become decreasing with increasing Fe doping level. Hence, the results indicate that CCTO still exhibits n-type conductivity even at the highest input Fe doping level of 9 wt%. When exposing the CCTO film to H_2S, H_2S molecules will adsorb on the sensor surface and react with preadsorbed oxygen species according to the following reaction paths [78]:

$$H_2S + 3O^-_{(ads)} \rightarrow SO_2 + H_2O + 3e^- \qquad (3)$$

$$H_2S + 3O^{2-}_{(ads)} \rightarrow SO_2 + H_2O + 6e^- \qquad (4)$$
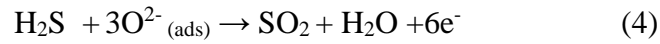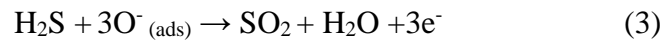
Due to the surface reactions, the electrons from the surface oxygen species will be released into CCTO conduction band, resulting in the reduction of electron depletion layer and electrical resistance of CCTO film. In order to induce the reactions in Eqs. (3)-(4), H_2S must bind on to CCTO surface. With Fe doping, Fe atoms may form favorable reactive sites for H_2S binding since Fe atoms at the Fe occupied lattice positions can have strong chemical interaction with sulfur atoms in H_2S molecules, resulting in simulated reducing reactions of H_2S. In addition, iron oxide has been reported to be an effective catalyst for H_2S oxidation according to [72, 73, 79].

$$FeO_x + x \cdot H_2S \rightarrow FeS_x + x \cdot H_2O \qquad (5)$$

$$FeS_x + \frac{3}{2}x \cdot O_2 \rightarrow FeO_x + x \cdot SO_2 \qquad (6)$$

The reaction in Eq. (5) produces water and sulfide functional groups (FeS_x), which is subsequently regenerated according to reaction in Eq. (6) in air. The reactions do not directly induce electrons but cause the increase in conductivity via the formation of conductive FeS_x. The Fe occupied site in CCTO may be represented as a FeO_6 cage and these reactions can thus be applied. Therefore, Fe dopants in CCTO could be effective catalysts that can selectively enhance the reducing reaction and response rates

with H₂S. Regarding the effect of Fe doping on operating temperature, Fe dopants cause a reduction in the optimum operating temperature. The sensor response to H₂S of Fe-doped CCTO sensors tends to decrease sharply at high temperatures (>250 °C). This characteristic may be explained based on the influence of oxygen species on Fe dopants in CCTO structure. When sensors are activated at higher temperature (250-350°C), O_{ads}^{-} and O_{ads}^{2-} will be more prevalent on surface as well as inside crystal grains. As a result, they can cumulatively adsorb at Fe-occupied lattice sites and may shield Fe atoms from H₂S molecules. Thus, they can act as a barrier to obstruct the reducing reaction and diminish the possibility for H₂S interaction with Fe sites on CCTO surface, resulting in lower H₂S response.

5.6 Electrical properties of undoped and Fe-doped CCTO thin films on LAO (100) and NGO (100)

As very well known, CCTO as a modern ceramic has been become interested in electrical properties as a giant dielectric material with a promising for essential applications such as varistors, pyro-sensors, energy storages, physical memory (RAM), bilayer thin film capacitors, microwave devices, and metal oxide thin films based super capacitors. CCTO exhibits unusual high dielectric constant of 10^4-10^5 for bulk ceramics and 10^2-10^3 for thin film capacitors. There are several factors that could affect the dielectric constant properties such as the film thickness, types of metal dopants, the annealing temperature, the annealing duration time, metal contact electrodes, types of

substrates and the stoichiometry. In general, the dielectric constant and the loss tangent of materials are measured as a function of frequency, applied voltage, and temperature.

In this dissertation, CCTO thin films were grown on LAO and NGO (100) in order to observe the effect of preferred orientation in the films on their dielectric constants. All the studied films had the thickness approximately 400 ± 20 nm. Fe-doped CCTO with 3 and 5 by wt% of Fe dopants were deposited in both types of single crystals in order to compare the dielectric constant and the loss tangent. Thin film capacitors were measured as a function of frequency at room temperature with oscillating voltage at 500 mV. The frequencies were in the range from 40 Hz to 1 MHz. For preparing conditions of CCTO thin films, although samples for device fabrications were coated by 3 layers which was different thickness compared to 4 layers of around 100 nm, the dielectric constants did not exactly differ due to the exponential term as illustrated in E (4.3) of Fernell's approximation [56].
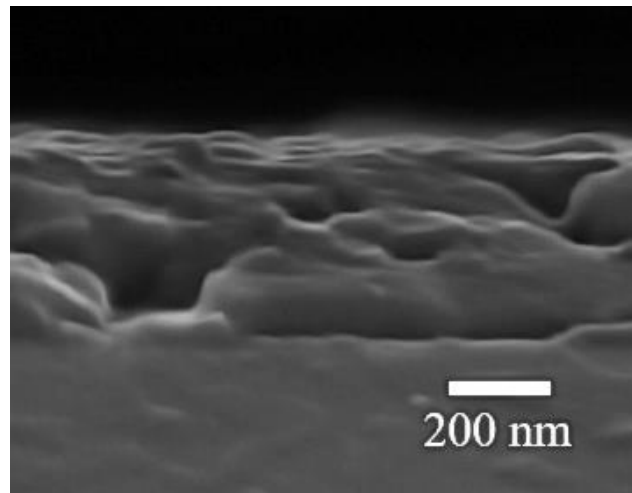
Figure 5.23: The cross section of CCTO grown on single crystals for 3 layer depositions displaying overall thickness approximately 400±20 nm.

As seen from the CCTO/LAO(100) and CCTO/NGO(100) samples, overall, the dielectric constants decreased when the frequency was adjusted from low to high values. An undoped CCTO on LAO(100) sample showed the highest magnitude of dielectric constants around 7480 and it declined over triple at 1 kHz. Both of 3 wt% and 5 wt% Fe-doped CCTO represented similar dielectric constants with 5400 and 5235 respectively and approximately nearly 10 times of dielectric constants were dropped at 1 kHz. The dielectric constants at 1 MHz for undoped CCTO was of 1040 which was higher than that of 3 wt% and 5 wt% of Fe doped CCTO with 878 and 766, respectively.

The trend of dielectric constants for CCTO/NGO(100) samples were also similar to CCTO/LAO(100) samples but the values of dielectric constant of the films deposited on NGO were higher than on LAO. The dielectric constants of CCTO on NGO was at 8800 for 40 Hz of frequency measurement, but the dielectric constants dropped by 3870 at 1 kHz. Furthermore, the dielectric constants of both 3 wt% and 5 wt% Fe-doped CCTO/NGO(100) films showed similar values around 5020 and 5008 respectively at 40 Hz. For every film sample deposited on NGO, the dielectric constants measured at 1 MHz exhibited similar values approximately 2400-2500. The dielectric loss tangent or dissipation factor were the result of oscillating polarized charges under applied alternatively electric fields into crystals. When materials were activated with varied oscillating field, it drove the polarized charges forward and backward. It seemed to be like charge movement of electric current, and this phenomenon leads to lost 90° out of phase with the voltage as described in Eq. (2.28) in the Chapter 2. The CCTO/LAO(100) sample exhibited the dielectric loss tangent about 0.86423 at 10 kHz and it drops to 0.04968 at 1MHz. When the quantity of Fe^{3+} was added into CCTO linearly, the dielectric loss tangents obviously declined significantly as illustrated in the Table 5.7 and 5.8. Undoped CCTO/NGO(100) sample showed the loss tangent nearly twice of undoped CCTO/LAO(100) of 0.65749 at 10 kHz and 0.03282 at 1000 kHz. Likewise, the dielectric constant Fe-doped CCTO with 3 wt% and 5 wt% were compared to that of pure CCTO on NGO (100) that dropped over 7 and 43 times at 10 kHz and 3 and 6 times at 1000 kHz, respectively. With increasing Fe doping content, the resistivity of grains and grain boundaries was assume to increase leading to a decrease in dielectric constant in the studied frequency range.

Table 5.6: The frequency dependence of the dielectric properties of undoped and Fe-doped CCTO deposited on LAO (100) substrates.

CCTO/LAO (100)	Frequency dependence of dielectric properties (Room Temperature)		
	40 Hz	10 kHz	1 MHz
undoped	$\varepsilon_r = 8800$ $\delta = 93.14265$	$\varepsilon_r = 3773$ $\delta = 0.86423$	$\varepsilon_r = 2540$ $\delta = 0.04968$
3 wt% Fe doped	$\varepsilon_r = 5021$ $\delta = 16.56195$	$\varepsilon_r = 2743$ $\delta = 0.13918$	$\varepsilon_r = 2403$ $\delta = 0.06082$
5 wt% Fe doped	$\varepsilon_r = 5008$ $\delta = 6.11932$	$\varepsilon_r = 2543$ $\delta = 0.08405$	$\varepsilon_r = 2425$ $\delta = 0.01493$

Table 5.7: The frequency dependence of the dielectric properties of undoped and Fe-doped CCTO deposited on NGO (100) substrates.

CCTO/NGO (100)	Frequency dependence of dielectric properties (Room Temperature)		
	40 Hz	10 kHz	1 MHz
undoped	$\varepsilon_r = 8800$ $\delta = 183.14265$	$\varepsilon_r = 3773$ $\delta = 1.52172$	$\varepsilon_r = 2540$ $\delta = 0.08250$
3 wt% Fe doped	$\varepsilon_r = 5021$ $\delta = 21.3059$	$\varepsilon_r = 2743$ $\delta = 0.20561$	$\varepsilon_r = 2403$ $\delta = 0.02590$
5 wt% Fe doped	$\varepsilon_r = 5008$ $\delta = 0.81398$	$\varepsilon_r = 2543$ $\delta = 0.03480$	$\varepsilon_r = 2425$ $\delta = 0.01381$
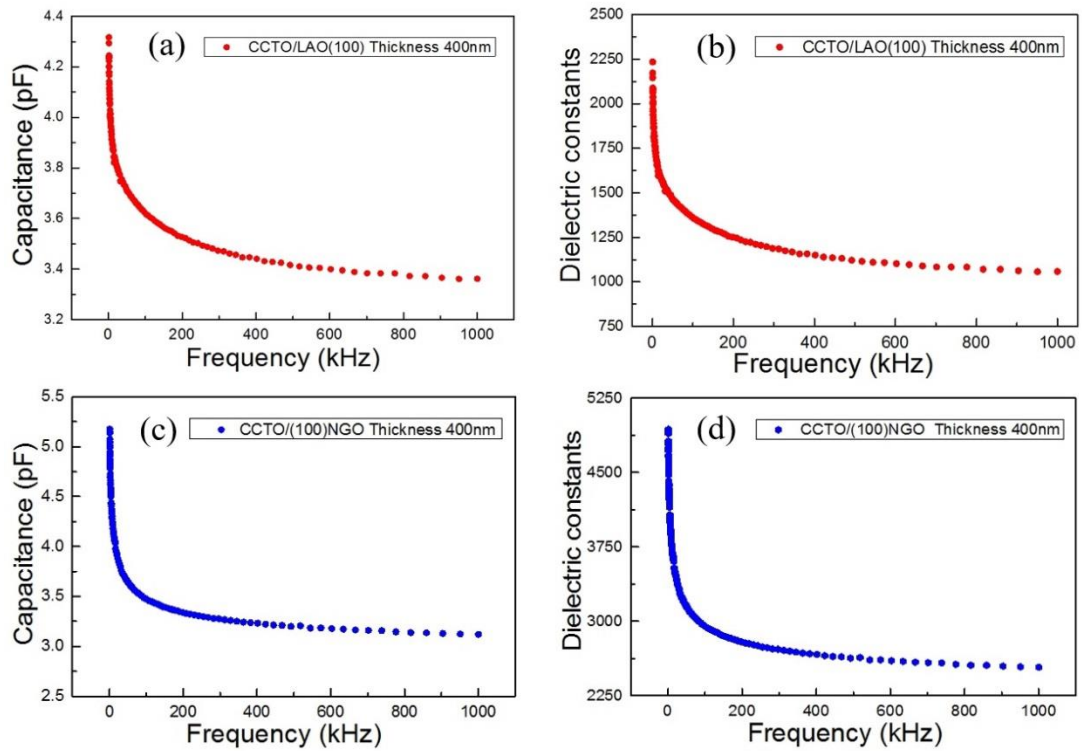
Figure 5.24: The frequency dependence of dielectric constants and the capacitance measurement at frequency in ranging between 1 and 1000 kHz of undoped $CaCu_3Ti_4O_{12}$ thin films grown on $LaAlO_3$ (100) ((a)-(b)) and $NdGaO_3$ (100) ((c)-(d)) with oscillating voltage at 500 mV at room temperature.
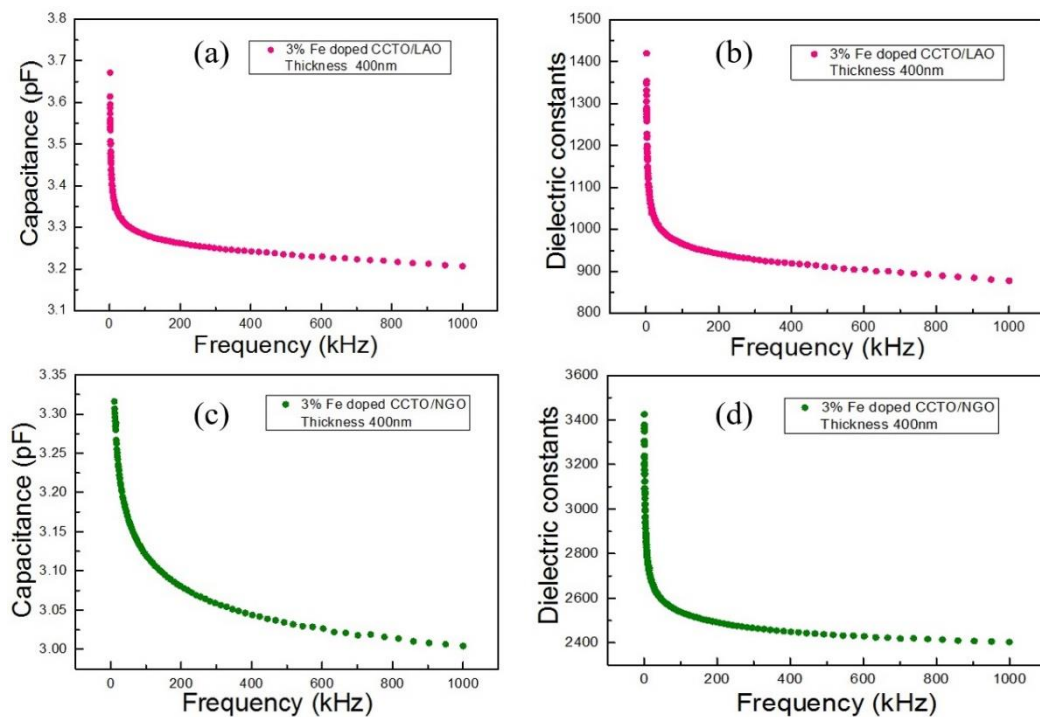
Figure 5.25: The frequency dependence of dielectric constants and the capacitance measurement at frequency in ranging between 1 and 1000 kHz of 3% for Fe doped CaCu$_3$Ti$_4$O$_{12}$ thin films grown on LaAlO$_3$ (100) ((a)-(b)) and NdGaO$_3$ (100) ((c)-(d)) with oscillating voltage at 500 mV at room temperature.
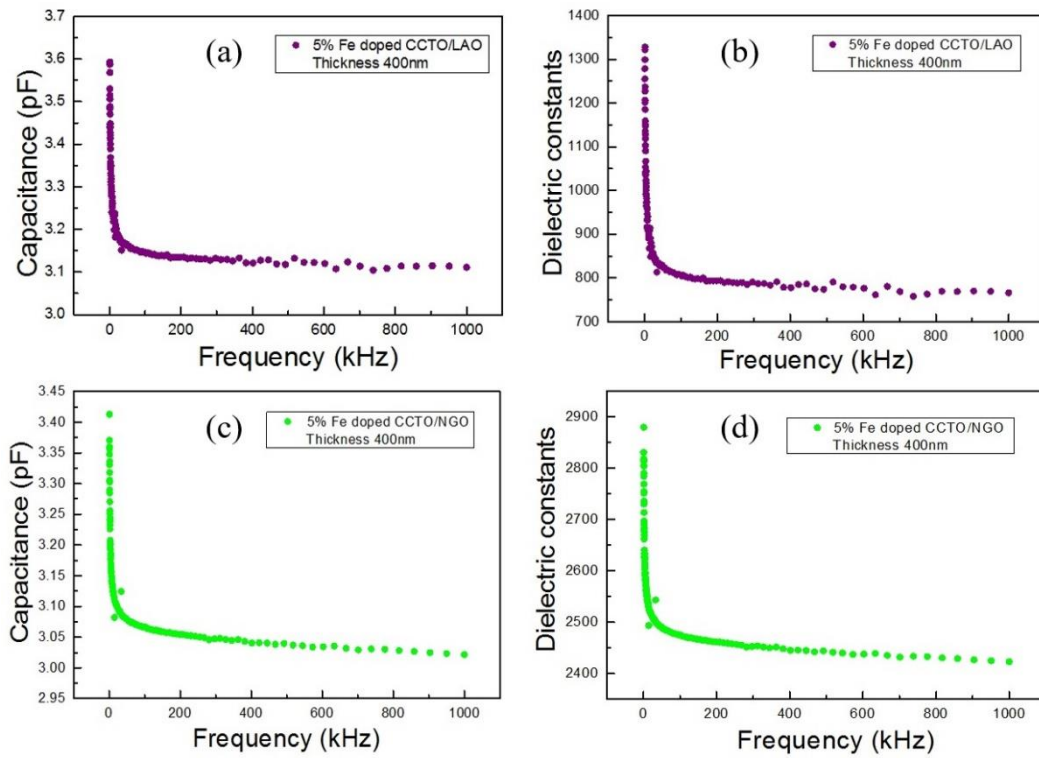
Figure 5.26: The frequency dependence of dielectric constants and the capacitance measurement at frequency in ranging between 1 and 1000 kHz of 5% for Fe doped $CaCu_3Ti_4O_{12}$ thin films grown on $LaAlO_3$ (100) ((a)-(b)) and $NdGaO_3$ (100) ((c)-(d)) with oscillating voltage at 500 mV at room temperature.
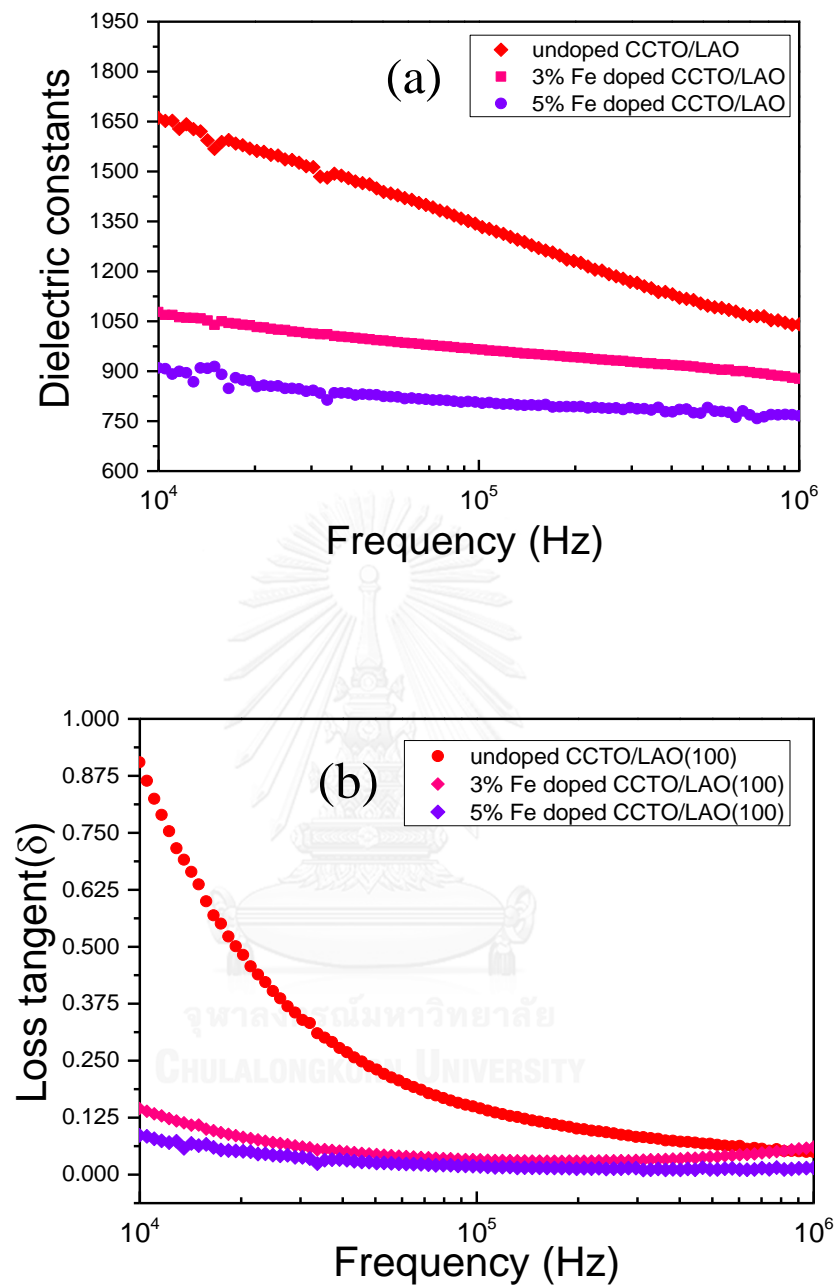
Figure 5.27: The frequency dependence of (a) the dielectric constant and (b) the loss tangent of undoped, 3%wt, 5%wt doped $CaCu_3Ti_4O_{12}$ thin film grown on $LaAlO_3$ (100) substrates measured at room temperature.
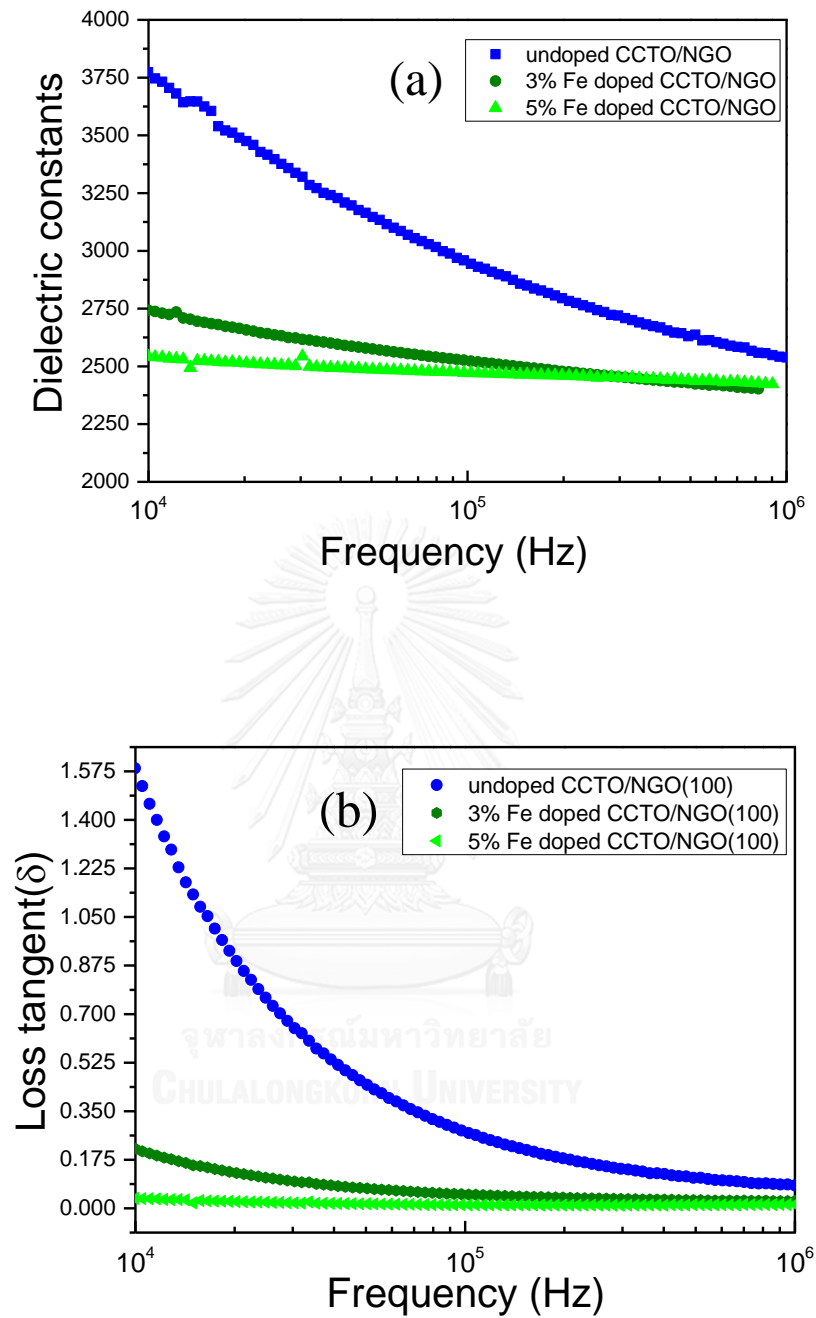
Figure 5.28: The frequency dependence of the dielectric constant and the loss tangent of undoped, 3%wt, 5%wt Fe-doped $CaCu_3Ti_4O_{12}$ thin films grown on $NdGaO_3$ (100) substrates measured at room temperature.

CHAPTER VI

CONCLUSIONS

CCTO thin films were synthesized by a sol gel precursor solution with a spinning coating process. Substrates such as silicon (Si(100)), alumina (Al_2O_3), lanthanum aluminate (LAO(100)), neodymium gallate (NGO(100)) were used for thin film depositions. Material characterizations and devices fabrication were done in this thesis. In order to utilize CCTO as smart electronic devices, the wet photolithographic patterning process has been done in a clean room and the interdigitated Cr/Au or Al electrodes were patterned by a DC sputtering. The patterned films were cut to individual devices; on alumina substrates are for gas sensors and on LAO and NGO substrates are for coplanar capacitors.

The field emission electron microscopy (FESEM) results revealed the surface morphology of CCTO grown on Si(100), alumina, LAO(100), and NGO(100) substrates for both top views and cross section images in order to observe the grain size, the shape, the film dense and the film thickness. Atomic force microscopy (AFM) was utilized to assist in looking at tiny surface areas and obtaining the root mean square roughness for each film. The energy dispersive X-ray spectroscopy (EDS) identified the chemical compositions of pure and Fe-doped CCTO films. Raman spectra verified the chemical fingerprint and vibration modes of the CCTO phases and other phases in

the CCTO films. X-ray diffraction (XRD) technique was used to prove the crystallinity and the preferred-orientations of the films. The chemical states and the elemental compositions of the films at room temperature were analyzed by X-ray photoelectron spectroscopy (XPS). The CCTO films deposited on Si (100) substrate were used for some characterization. The CCTO films deposited on Al_2O_3 substrates were brought to check the gas sensing responses after patterning with Cr/Au electrode. The CCTO films deposited on single crystals, $LaAlO_3$ (LAO(100)) and $NdGaO_3$ (NGO(100)) were fabricated to interdigitated coplanar capacitors with Al electrode for measuring the dielectric constants and the dielectric loss tangent.

The conclusion will be divided into 3 main topics.

Topic#1: Fe-doping in CCTO thin films on Al_2O_3 substrates and their H_2S gas sensing responses.

Various gas targets such as C_2H_2, CH_4, CO, NO_2, NH_3, H_2S and ethanol and several operating temperatures were used in this thesis experiment in order to check the selectivity and the sensitivity. The result of gas sensing measurements on the Fe-doped CCTO film devices revealed that H_2S show a high performance of the gas response and the selectivity compared to other gases. The effects of Fe-doping on structural and gas-sensing properties of CCTO thin film prepared by a sol-gel method were systematically investigated. Characterizations by XRD and Raman spectra confirmed the perovskite CCTO phase and revealed unexpected secondary phases including TiO_2 and CuO but there was no secondary phase of iron or iron oxide compound in Fe-doped CCTO film. EDX and XPS analyses confirmed the presence of Fe atoms and indicated that the oxidation of iron atom was Fe^{3+}. From gas-sensing measurements, Fe dopants greatly

enhanced the sensor response and selectivity to H_2S against NH_3, CO, C_2H_2, CH_4, ethanol and NO_2. The roles of Fe-dopant on gas-sensing mechanisms of CCTO sensor were explained based on electronic and catalytic effects of substitutional p-type dopants. But the behavior of Fe-CCTO films is n-type semiconductor due to the dominant oxygen vacancies in the films compared to the generated holes from the gas mechanism reaction. Note that the best CCTO film that response to H_2S the most was grown under the growth parameters; annealing temperature at 800 °C, 6 thickness layers and the maximum Fe concentration (9 wt%). In particular, the 9 wt% Fe-doped CCTO film sensor exhibited the highest response of ~126 to 10 ppm H_2S, which was more than one order of magnitude higher than that of undoped CCTO at a low optimum operating temperature of 250°C. EDX and XPS analyses analyses confirmed the presence of Fe^{3+} substitution into Ti^{4+} sites. The roles of Fe-dopant on gas-sensing mechanisms of CCTO sensor were explained based on electronic and catalytic effects of substitutional p-type dopants, not much on the microstructure (surface facet sizes are not much different) effects.

In comparison with other recently reported metal oxide materials as listed in Table 5.5 in Section 5.4 in Chapter 5, the Fe-doped CCTO thin film exhibits relatively high response at the same or lower H_2S concentration except for the case of some materials in the form of nano-shapes. Thus, the sol–gel Fe-doped CCTO sensor offers decent H_2S-sensing performances comparable with several advanced nanostructure materials despite its thin film form which is expected to have relatively small specific surface area.

Topic#2: Crystal structure and surface morphology of CCTO films on Si(100) and highly- oriented CCTO films on LaAlO$_3$(100) and NdGaO$_3$(100) single crystal substrates.

Highly-oriented CaCu$_3$Ti$_4$O$_{12}$ (CCTO) thin films deposited on LAO(100), NGO(100) and NGO(110) substrates have been developed successfully using a sol-gel spinning method. The similarity in lattice mismatch and the similarity in crystal structure between the film and the substrate, the orientation of the substrate is a crucial parameter for preferred orientation growth. The NGO (110) can dominant the oriented arrangement of (h00) CCTO which is same as LAO (100); however, the lattice mismatch between NGO (110) and LAO (100) are different while NGO (100) affects in another specific plane of (hh0) CCTO. Overall grain size of CCTO grown on NGO (100) was larger than that of grown on LAO (100). The lattice mismatch of CCTO on LAO(100) was approximately 2.5% whereas that of CCTO on NGO(100) was around 4.5%. If the alpha from calculations higher than one, that means CCTO grown on LAO(100), NGO(100) and NGO (110) exhibited highly-preferred orientation. While, CCTO deposited on NGO (100) provides the preferred (hh0) planes of CCTO which are the maximum relative intensity as seen from the CCTO data base, the result from calculation is higher than one which is the exceptional for this plane. The optimum condition for CCTO thin film grown on LAO (100) is at 800 ^{o}C for annealing temperature because there is no the second phase transition lower than 800 ^{o}C. Actually for the films grown on NGO (100), another formula is used for calculating the preferred orientation to compare among the CCTO/NGO films just by using the intensity ratio of (220) to (411). As a result, the 4 layer-deposition film annealed at 1000 ^{o}C on NGO shows the maximum value because the thicker film and the film annealed at higher

temperature always shows better crystallinity confirmed by FESEM image. Thus, it leads to the high diffracted intensity of (hh0) plane family. The advantage of using NGO as the substrate for CCTO is that the phase transition temperature of NGO is higher than annealing condition for CCTO thin film growth (800-1000 ℃).

Topic#3: Thin film CCTO and Fe-doped coplanar capacitors on LAO and NGO substrates and their dielectric properties.

Thin film capacitors grown on both LAO(100) and NGO(100) show high dielectric constants for low dimensional systems (2D) because of high quality of films by the highly preferential arrangement in the crystal plane. The average thickness of films was around 400 ±20 nm. The Fe added into CCTO for thin film capacitors played an essential role in reducing dielectric loss tangents. The dielectric constants of all Fe-doped CCTO samples decreased. However, the values of dielectric constant for all Fe-doped still remains high but the dielectric loss tangents could be reduced by 2-3 times. The dielectric dependence of frequency for both of undoped and Fe-doped CCTO grown on NGO(100) are higher than that of pure and Fe adding into CCTO deposited on LAO(100). The dielectric loss tangent dependence of frequency at 1 MHz from samples on NGO(100) were twice as that from CCTO on LAO(100), 2540 and 1040 respectively. The dielectric constant and dielectric loss were measured at room temperature with the oscillating voltage of 500 mV. The Fernell's approximation was used to convert the capacitance of the film coplanar capacitor to the dielectric constant. The reason for adding Fe into CCTO films are in order to suppress dielectric loss tangent for coplanar capacitor. However, growth parameter must be chosen carefully and appropriately for proper applications. Alumina is the suitable substrate for gas

sensor application because it is inexpensive, and there is high roughness which could help to increase the small voids in the films resulting in increasing the surface reacting area. In the case of single crystal selection, most voids are large and not much and also there are very expensive for sensor fabrication whereas observable cross sections on CCTO films on alumina annealed at 800 °C exhibit highly porous and tiny grains.

Table 6.1: The summary results of CCTO on single crystals.

Measured at 1 MHz	CCTO/LAO(100) (400nm, @800°C)	CCTO/NGO(110) (400nm, @800°C)	CCTO/NGO(100) (400nm, @800°C)
ε_r	~1040	~1020	~2540
tangent (δ)	~0.0496	~0.0185	~0.0825
Alpha (α)	3.18	3.38	1.41

As illustrated in the table above, it showed the overall consequence of undoped CCTO on single crystal substrates with 800 °C of annealing temperature and the frequency selection. The comparisons of relative permittivity, dielectric loss tangent, and alpha calculations have been concluded that CCTO thin film grown on NGO(100) exhibited better dielectric constants than others. Therefore, the preferred (hh0) plane of CCTO films provided more dielectric constants than the highly oriented (h00) plane of CCTO films.

REFERENCES

[1] Kim, H.E., et al., *Growth and characterization of CaCu₃Ti₄O₁₂ single crystals.* Journal of Crystal Growth, 2014. **408**: p. 60-63.

[2] Zhao, J., J. Liu, and G. Ma, *Preparation, characterization and dielectric properties of CaCu₃Ti₄O₁₂ ceramics.* Ceramics International, 2012. **38**(2): p. 1221-1225.

[3] Chen, C., et al., *Enhanced nonlinear current–voltage behavior in Au nanoparticle dispersed CaCu₃Ti₄O₁₂ composite films.* Solid State Communications, 2011. **151**(19): p. 1336-1339.

[4] Felix, A.A., M.O. Orlandi, and J.A. Varela, *Schottky-type grain boundaries in CCTO ceramics.* Solid State Communications, 2011. **151**(19): p. 1377-1381.

[5] Joanni, E., et al., *P-type semiconducting gas sensing behavior of nanoporous rf sputtered CaCu₃Ti₄O₁₂ thin films.* Applied Physics Letters, 2008. **92**(13): p. 132110.

[6] Ponce, M.A., et al., *Electrical behavior analysis of n-type CaCu₃Ti₄O₁₂ thick films exposed to different atmospheres.* Journal of the European Ceramic Society, 2015. **35**(1): p. 153-161.

[7] Schmidt, R., et al., *Effects of sintering temperature on the internal barrier layer capacitor (IBLC) structure in CaCu₃Ti₄O₁₂ (CCTO) ceramics.* Journal of the European Ceramic Society, 2012. **32**(12): p. 3313-3323.

[8] Lee, S.-Y., et al., *Effect of copper-oxide segregation on the dielectric properties of CaCu₃Ti₄O₁₂ thin films fabricated by pulsed-laser deposition.* Thin Solid Films, 2010. **518**(20): p. 5711-5714.

[9] Lo Nigro, R., et al., *Chemical stability of CaCu₃Ti₄O₁₂ thin films grown by MOCVD on different substrates.* Thin Solid Films, 2007. **515**(16): p. 6470-6473.

[10] Foschini, C.R., et al., *CaCu₃Ti₄O₁₂ thin films with non-linear resistivity deposited by RF-sputtering.* Journal of Alloys and Compounds, 2013. **574**: p. 604-608.

[11] Kumar, P. and D.C. Agrawal, *Dielectric and optical properties of CaCu₃Ti₄O₁₂ thin films containing Ag nanoparticles.* Materials Letters, 2010. **64**(3): p. 350-352.

[12] Li, T., et al., *Effect of NiO-doping on the microstructure and the dielectric properties of CaCu₃Ti₄O₁₂ ceramics.* Ceramics International, 2014. **40**(7, Part A): p. 9061-9067.

[13] Li, T., et al., *The effect of Eu₂O₃ doping on CaCu₃Ti₄O₁₂ varistor properties.* Journal of Alloys and Compounds, 2009. **484**(1–2): p. 718-722.

[14] Mu, C., et al., *Influence of temperature on dielectric properties of Fe-doped CaCu₃Ti₄O₁₂ ceramics.* Physica B: Condensed Matter, 2010. **405**(1): p. 386-389.

[15] Zheng, Q., H. Fan, and C. Long, *Microstructures and electrical responses of pure and chromium-doped CaCu₃Ti₄O₁₂ ceramics.* Journal of Alloys and Compounds, 2012. **511**(1): p. 90-94.

[16] Bai, L., Y. Wu, and L. Zhang, *Influence of FeNb codoping on the dielectric and electrical properties of CaCu₃Ti₄O₁₂ ceramics.* Journal of Alloys and Compounds, 2016. **661**: p. 6-13.

[17] Rai, A.K., et al., *Dielectric properties of iron doped calcium copper titanate, CaCu$_{2.9}$Fe$_{0.1}$Ti$_4$O$_{12}$.* Journal of Alloys and Compounds, 2011. **509**(36): p. 8901-8906.

[18] Moriyama, T., A. Kan, and H. Ogawa, *Crystal structure and ferroelectric properties of Ca(Cu$_{3-x}$M$_x$)Ti$_4$O$_{12}$ (M = Fe and Ni) ceramics.* Materials Science and Engineering: B, 2013. **178**(13): p. 875-880.

[19] Yang, Z., et al., *Dielectric and Electrical Transport Properties of the Fe^{3+}-doped CaCu$_3$Ti$_4$O$_{12}$.* Journal of Materials Science & Technology, 2012. **28**(12): p. 1145-1150.

[20] Fan, H., Q. Zheng, and B. Peng, *Microstructure, dielectric and pyroelectric properties of CaCu$_3$Ti$_4$O$_{12}$ ceramics fabricated by tape-casting method.* Materials Research Bulletin, 2013. **48**(9): p. 3278-3283.

[21] Li, Z. and H. Fan, *Structure and electric properties of sol–gel derived CaCu$_3$Ti$_4$O$_{12}$ ceramics as a pyroelectric sensor.* Solid State Ionics, 2011. **192**(1): p. 682-687.

[22] Parra, R., et al., *Sol–gel synthesis of mesoporous CaCu$_3$Ti$_4$O$_{12}$ thin films and their gas sensing response.* Journal of Solid State Chemistry, 2010. **183**(6): p. 1209-1214.

[23] I.D. Kim, A.R., T. Hyodo, H.L. Tuller, *Microsphere templating as means of enhancing surface activity and gas sensitivity of CaCu3Ti4O$_{12}$ thin films.* Nano Lett., 2006. **6**: p. 193-198.

[24] M. Li, X.L.C., D.F. Zhang, W.Y. Wang, W.J. Wang, *Humidity sensitive properties of pure and Mg-doped CaCu$_3$Ti$_4$O$_{12}$.* Sens. Actuators B, 2010. **147**: p. 447-452.

[25] Z. Qu, Y.F., B. Yu, P. Deng, L. Xing, X. Xue, *High and fast H$_2$S response of NiO/ZnO nanowire nanogenerator as a self-powered gas sensor.* Sens. Actuators, B, 2016. **222**: p. 78-86.

[26] N. V. Toana, N.V.C., N. V. Duya, D. D. Vuongb, N. H. Lamb, N. D. Hoaa, N. V. Hieua, and N.D. Chiena, *Scalable fabrication of SnO$_2$ thin films sensitized with CuO islands for enhanced H$_2$S gas sensing performance.* Appl. Surf. Sci., 2015. **324**: p. 280-285.

[27] Ramirez, A.P., et al., *Giant dielectric constant response in a copper-titanate.* Solid State Communications, 2000. **115**(5): p. 217-220.

[28] Li, Y.W., et al., *Preparation and properties of CaCu$_3$Ti$_4$O$_{12}$ thin film grown on LaNiO$_3$-coated silicon by sol–gel process.* Journal of Crystal Growth, 2008. **310**(2): p. 378-381.

[29] Liu, L., et al., *Electrical heterogeneity in CaCu$_3$Ti$_4$O$_{12}$ ceramics fabricated by sol–gel method.* Solid State Communications, 2007. **142**(10): p. 573-576.

[30] Fang, L. and M. Shen, *Deposition and dielectric properties of CaCu$_3$Ti$_4$O$_{12}$ thin films on Pt/Ti/SiO$_2$/Si substrates using pulsed-laser deposition.* Thin Solid Films, 2003. **440**(1–2): p. 60-65.

[31] Subramanian, M.A., et al., *High Dielectric Constant in ACu$_3$Ti$_4$O$_{12}$ and ACu$_3$Ti$_3$FeO12 Phases.* Journal of Solid State Chemistry, 2000. **151**(2): p. 323-325.

[32] D. E. Kotecki, J.D.B., H. Shen, R. B. Labibowitz, K. L. Saenger, J. J. Lian, T. M., S.D.A. Shaw, C. Cabral, Jr., P. R. Duncombe, M. Gutsche, G. Kunkel, Y. J. Park, Y., and a.R.W. Y. Wang, *Epitaxial Thin Films of the Giant-Dielectric-*

Constant Material CaCu₃Ti₄O₁₂ Grown by Pulsed-laser Deposition. IBM J. Res. Dev., 1999. **43**: p. 367.

[33] Li, H.-C., et al., *Thickness dependence of dielectric loss in SrTiO₃ thin films.* Applied Physics Letters, 1998. **73**(4): p. 464-466.

[34] Prakash, B.S., et al., *Deposition and dielectric properties of CaCu₃Ti₄O₁₂ thin films deposited on Pt/Ti/SiO₂/Si substrates using radio frequency magnetron sputtering.* Thin Solid Films, 2008. **516**(10): p. 2874-2880.

[35] Xu, D., et al., *High dielectric permittivity and low dielectric loss in sol–gel derived Zn doped CaCu₃Ti₄O₁₂ thin films.* Materials Chemistry and Physics, 2015. **153**: p. 229-235.

[36] R. Bodeux, M.G., J. Wolfman, G. Liu, F. Gervais, *CaCu₃Ti₄O₁₂ thin film capacitors: Evidence of the presence of a Schottky type barrier at the bottom electrode.* Thin Solid Films, 2012. **520**: p. 2632-2638.

[37] Jiang †, J.C., et al., *Nanocomposite-like structure in an epitaxial CaCu₃Ti₄O₁₂ film on LaAlO₃ (001).* Philosophical Magazine Letters, 2004. **84**(7): p. 443-450.

[38] Feng, L., et al., *Growth of highly-oriented CaCu₃Ti4O₁₂ thin films on SrTiO₃ (1 0 0) substrates by a chemical solution route.* Applied Surface Science, 2006. **253**(4): p. 2268-2271.

[39] Si, W., et al., *Epitaxial thin films of the giant-dielectric-constant material CaCu₃Ti₄O₁₂ grown by pulsed-laser deposition.* Applied Physics Letters, 2002. **81**(11): p. 2056-2058.

[40] Bdikin, I.K., et al., *The growth and domain structure of YBa₂Cu₃Ox films on neodymium gallate substrates with a deviation of the normal to the surface from the [110] direction in NdGaO₃.* Physics of the Solid State, 2001. **43**(9): p. 1611-1620.

[41] Hodak, S.K. and C.T. Rogers, *Microstructure and dielectric response of SrTiO₃/NdGaO₃ interdigitated capacitors.* Microelectronic Engineering, 2008. **85**(2): p. 444-451.

[42] Liu, Y., R.L. Withers, and X.Y. Wei, *Structurally frustrated relaxor ferroelectric behavior in CaCu₃Ti₄O₁₂.* Physical Review B, 2005. **72**(13): p. 134104.

[43] Singh, L., et al., *Progress in the growth of CaCu₃Ti₄O₁₂ and related functional dielectric perovskites.* Progress in Crystal Growth and Characterization of Materials, 2014. **60**(2): p. 15-62.

[44] Leret, P., et al., *Phenomenological model of grain boundary behaviour under a bias field in Nb-doped CaCu₃Ti₄O₁₂ ceramics.* Journal of Alloys and Compounds, 2011. **509**(41): p. 9719-9723.

[45] Singh, J., *Smart Electronic Materials Fundamentals and Applications.* April 2005, U.K.: Cambridge University press.

[46] Potyrailo, R.A., *Metal Oxide Nanomaterials for Chemical Sensors.* September 2012, New York USA: Springer.

[47] Wahab, M.A., *Solid State Physics structure and properties of Materials.* second editions ed. 2005, Harrow, U.K.: Alpha Science International Ltd.

[48] Heide, P.V.D., *X-ray Photoelectron Spectroscopy an Introduction to Principle and Practices.* 2012, Canada: A JOHN WILEY & Sons, Inc.

[49] Sloog, D.A.a.L., J. J., *Principles of Instrumental Analysis.* 1992, USA: Saunders College Publishing Ltd.

[50] G. Friedbacher and H. Bubert, *Surface and Thin Film Analysis: A compendium of Principles Instrumentation and Applications*. second edition ed. 2011: Wiley-VCH Verlag GmbH & Co. KGaA.

[51] S. L. Zhang, *Raman Spectroscopy and its Application in Nanostructures*. 2012, Malaysia: A JOHN WILEY & Sons, Inc.

[52] Kasa, Y., *Microstructural and Dielectric properties of Calcium Copper Titanate Thin Films prepared by a Sol-gel Meathod*. 2010, Chulalongkorn University.

[53] Supasai, T., *Electrical, Optical and gas sensing properties of Barium Titanate/Strontium Taitanate Thin Films*. 2010. , Chulalongkorn University.

[54] Hodak, S.K., et al., *Design of Low Cost Gas Sensor Based on SrTiO₃ and BaTiO₃ Films.* Journal of Nanoscience and Nanotechnology, 2010. **10**(11): p. 7236-7238.

[55] C. J. Brinker, G.W.S., *Sol gel science the physics and chemistry of sol gel processing* 1990, New York, USA: Academic Press.

[56] Fernell, G.W., Cermak, I. A., and wong, S. K. , *Capacitance and field distributions for interdigital surface-wave transducers.* IEEE T. Son. Ultrason, 1970. **17**: p. 188-195.

[57] Ouyang, X., et al., *Enhanced extrinsic dielectric response of TiO₂ modified CaCu₃Ti₄O₁₂ ceramics.* Ceramics International, 2015. **41**(10, Part A): p. 13447-13454.

[58] Mohamed, J.J., S.D. Hutagalung, and Z.A. Ahmad, *Influence of sintering parameters on melting CuO phase in CaCu₃Ti₄O₁₂.* Journal of King Saud University - Engineering Sciences, 2013. **25**(1): p. 35-39.

[59] Balouria, V., et al., *Nano-crystalline Fe₂O₃ thin films for ppm level detection of H₂S.* Sensors and Actuators B: Chemical, 2013. **181**: p. 471-478.

[60] Moreira, M.L., et al., *Structural and optical properties of CaTiO₃ perovskite-based materials obtained by microwave-assisted hydrothermal synthesis: An experimental and theoretical insight.* Acta Materialia, 2009. **57**(17): p. 5174-5185.

[61] Moura, F., et al., *Intense photoluminescence emission at room temperature in calcium copper titanate powders.* Ceramics International, 2013. **39**(4): p. 3499-3506.

[62] Ma, H.L., et al., *Raman study of phase transformation of TiO₂ rutile single crystal irradiated by infrared femtosecond laser.* Applied Surface Science, 2007. **253**(18): p. 7497-7500.

[63] Punginsang, M., et al., *Effects of cobalt doping on nitric oxide, acetone and ethanol sensing performances of FSP-made SnO₂ nanoparticles.* Sensors and Actuators B: Chemical, 2015. **210**: p. 589-601.

[64] Biesinger, M.C., et al., *Resolving surface chemical states in XPS analysis of first row transition metals, oxides and hydroxides: Sc, Ti, V, Cu and Zn.* Applied Surface Science, 2010. **257**(3): p. 887-898.

[65] Yao, Z., et al., *Structure and dielectric behavior of Nd-doped BaTiO₃ perovskites.* Materials Chemistry and Physics, 2008. **109**(2–3): p. 475-481.

[66] Zimmermann, R., et al., *Electronic structure systematics of 3d transition metal oxides.* Journal of Electron Spectroscopy and Related Phenomena, 1998. **96**(1–3): p. 179-186.

[67] Yamashita, T. and P. Hayes, *Analysis of XPS spectra of Fe^{2+} and Fe^{3+} ions in oxide materials.* Applied Surface Science, 2008. **254**(8): p. 2441-2449.

[68] Aronniemi, M., J. Lahtinen, and P. Hautojärvi, *Characterization of iron oxide thin films.* Surface and Interface Analysis, 2004. **36**(8): p. 1004-1006.

[69] Ramgir, N.S., et al., *Room temperature H_2S sensor based on Au modified ZnO nanowires.* Sensors and Actuators B: Chemical, 2013. **186**: p. 718-726.

[70] Bai, S., et al., *Synthesis of MoO_3/reduced graphene oxide hybrids and mechanism of enhancing H_2S sensing performances.* Sensors and Actuators B: Chemical, 2015. **216**: p. 113-120.

[71] Zhao, C., et al., *Improving gas-sensing properties of electrospun In_2O_3 nanotubes by Mg acceptor doping.* Sensors and Actuators B: Chemical, 2015. **207, Part A**: p. 313-320.

[72] Wang, Y., et al., *H_2S sensing characteristics of Pt-doped $α-Fe_2O_3$ thick film sensors.* Sensors and Actuators B: Chemical, 2007. **125**(1): p. 79-84.

[73] Wang, Y., et al., *Low-temperature H_2S sensors based on Ag-doped $α-Fe_2O_3$ nanoparticles.* Sensors and Actuators B: Chemical, 2008. **131**(1): p. 183-189.

[74] Wang, Y., et al., *Enhanced H_2S sensing characteristics of CuO-NiO core-shell microspheres sensors.* Sensors and Actuators B: Chemical, 2015. **209**: p. 515-523.

[75] Lee, I., et al., *The stability, sensitivity and response transients of ZnO, SnO_2 and WO_3 sensors under acetone, toluene and H_2S environments.* Sensors and Actuators B: Chemical, 2014. **197**: p. 300-307.

[76] H.L. Yu, L.L., X.-M. Gao, Y. Zhang, F. Meng, T.S. Wang, G. Xiao, Y.J. Chen, C.-L. Zhu, *Synthesis and H_2S gas sensing properties of cage-like $α-MoO_3$/ZnO composite.* Sens. Actuators B 2012. **197**: p. 171-172.

[77] Kruefu, V., et al., *Ultra-sensitive H_2S sensors based on hydrothermal/impregnation-made Ru-functionalized WO_3 nanorods.* Sensors and Actuators B: Chemical, 2015. **215**: p. 630-636.

[78] Wetchakun, K., et al., *Semiconducting metal oxides as sensors for environmentally hazardous gases.* Sensors and Actuators B: Chemical, 2011. **160**(1): p. 580-591.

[79] M.A. Shields, N.I.D., P.D. Clark, *Catalytic H_2S conversion and SO_2 production over iron oxide and iron Oxide/Gamma-Al_2O_3 in liquid sulfur.* Ind. Eng. Chem. Res., 2007. **46** p. 7721-7728.

Appendix A

X-ray Diffraction Database

The crystal structure of the CCTO films on substrates were synthesized by the sol gel method and they were observed from XRD spectra compared to the XRD database reported by the International Centre for Diffraction Data (ICDD) as illustrated by

| Pattern : 00-021-1276 | | Radiation = 1.540598 | | Quality : High |

TiO₂

Titanium Oxide
Rutile, syn
Also called: titania

Lattice : Tetragonal		*Mol. weight =* 79.90
S.G. : P42/mnm (136)		*Volume [CD] =* 62.43
a = 4.59330		*Dx =* 4.250
		Dm = 4.230
c = 2.95920		
	Z = 2	*I/cor =* 3.40

General comments: No impurity over 0.001%.
Vickers hardness number: VHN₁₀₀=1132-1187.
Sample source or locality: Sample obtained from National Lead Co., South Amboy, New Jersey, USA.
General comments: Pattern reviewed by Syvinski, W., McCarthy, G., North Dakota State Univ, Fargo, North Dakota, USA, *ICDD Grant-in-Aid* (1990). Agrees well with experimental and calculated patterns.
General comments: Two other polymorphs, anatase (tetragonal) and brookite (orthorhombic), converted to rutile on heating above 700 C.
General comments: Additional weak reflections [indicated by brackets] were observed.
Optical data: A=2.9467, B=2.6505, Sign=+
Additional pattern: Validated by calculated pattern.
General comments: Optical data on specimen from *Dana's System of Mineralogy*, 7th Ed., I 555.
General comments: Naturally occurring material may be reddish brown.
Color: White
Reflectance: Opaque mineral optical data on specimen from Sweden: R₃R%= 20.3, Disp.=Std.
Temperature of data collection: Pattern taken at 25 C.
Data collection flag: Ambient

Natl. Bur. Stand. (U.S.) Monogr. 25, volume 7, page 83 (1969)

Radiation : CuKa1	*Filter :* Monochromator crystal
Lambda : 1.54056	*d-sp :* Not given
SS/FOM : F30=108(0.0087,32)	*Internal standard :* W

2th	I	h	k	l
27.447	100	1	1	0
36.086	50	1	0	1
39.188	8	2	0	0
41.226	25	1	1	1
44.052	10	2	1	0
54.323	60	2	1	1
56.642	20	2	2	0
62.742	10	0	0	2
64.040	10	3	1	0
65.480	2	2	2	1
69.010	20	3	0	1
69.790	12	1	1	2
72.410	2	3	1	1
74.411	1	3	2	0
76.510	4	2	0	2
79.822	2	2	1	2
82.335	6	3	2	1
84.260	4	4	0	0
87.464	2	4	1	0
89.557	8	2	2	2
90.708	4	3	3	0
95.275	6	4	1	1
96.017	6	3	1	2
97.176	4	4	2	0
98.514	1	3	3	1
105.099	2	4	2	1
106.019	2	1	0	3
109.406	2	1	1	3
116.227	4	4	0	2
117.527	4	5	1	0
120.059	8	2	1	3
122.788	8	4	3	1
123.660	8	3	3	2
131.847	6	4	2	2
136.549	8	3	0	3
140.052	12	5	2	1
143.116	2	4	4	0
155.869	2	5	3	0

| Pattern : 00-029-1360 | | Radiation = 1.540598 | | Quality : High |

TiO₂

Titanium Oxide
Brookite

2th	I	h	k	l
25.340	100	1	2	0
25.689	80	1	1	1
30.808	90	1	2	1
32.791	4	2	0	0
36.252	25	0	1	2
37.297	18	2	0	1
37.934	6	1	3	1
38.371	4	2	2	0
38.576	4	2	1	1
39.205	5	0	4	0
39.967	8	1	1	2
40.153	18	0	2	2
42.340	16	2	2	1
46.072	16	0	3	2
48.012	30	2	3	1
49.173	18	1	3	2
49.694	3	2	1	2
52.012	3	2	4	0
54.205	20	3	2	0
55.234	30	2	4	1
55.711	5	1	5	1
57.176	13	1	1	3
57.685	2	2	3	2
59.991	7	1	2	3
62.065	10	0	5	2
63.065	4	1	6	0
63.415	9	3	1	2
63.643	12	2	5	1
64.104	12	2	0	3
64.603	6	1	3	3
65.002	10	2	1	3
65.876	9	1	6	1
68.768	5	4	0	0
70.432	8	3	3	2
71.490	3	4	0	1
71.931	2	2	1	3
73.648	2	0	0	4
76.948	10	0	2	4
79.024	2	4	3	1
79.283	1	1	2	4
83.643	4	3	3	3
84.287	2	0	8	0
84.724	2	4	4	1
86.743	4	0	4	4
95.590	3	5	2	1
95.590	3	4	2	3
95.993	2	2	8	1
97.609	4	3	2	4
102.559	2	1	2	5
103.201	4	3	7	1
103.201	4	2	5	4

Lattice : Orthorhombic

S.G. : Pcab (61)

a = 5.45580

b = 9.18190

c = 5.14290

a/b = 0.59419

c/b = 0.56011

Z = 8

Mol. weight = 79.90

Volume [CD] = 257.63

Dx = 4.120

Dm = 4.140

Optical data: A=2.5831, B=2.5843, Q=2.7004, Sign=+, 2V=~28°
Additional pattern: To replace 00-016-0617 and validated by calculated pattern.
Color: Black
Additional pattern: See ICSD 36408 (PDF 01-076-1934).
Sample source or locality: Specimen from Magnet Cove, Arkansas, USA (USNM 97661).
Analysis: Spectrographic analysis: 0.1-1.0% Si; 0.01-0.1% each of Al, Fe, and V; 0.001-0.01% Mg.
General comments: Niobian brookite from Mozambique [Chemical analysis (wt.%): Ti O2 80.7, Nb2 O5 14.1, FeO 5.53]; Carvalho et al., *Rev. Cien. Geol. Ser. A,* **7** 61 (1974) reports an identical pattern.
Temperature of data collection: Pattern taken at 25 C.
General comments: Intensities verified by calculated pattern.
Data collection flag: Ambient.

Natl. Bur. Stand. (U.S.) Monogr. 25, volume 3, page 57 (1964)

Radiation : CuKa1

Lambda : 1.54056

SS/FOM : F30= 58(0.0115,45)

Filter : Beta

d-sp : Not given

Pattern : 03-065-5714	*Radiation* = 1.540598 *Quality* : Calculated

TiO₂

Titanium Oxide

Lattice : Body-centered tetragonal	*Mol. weight* = 79.90
S.G. : I41/amd (141)	*Volume [CD]* = 136.30
a = 3.78500	*Dx* = 3.894
c = 9.51400	
Z = 4	*I/cor* = 5.04

NIST M&A collection code: A 50867 ST1243   1
Temperature factor: TF Isotropic TF given by author
Sample preparation: Commercial pigmentary material was used
Remarks from ICSD/CSD: Anatase-synthetic
Data collection flag: Ambient

Cromer, D.T., Herrington, K., J. Am. Chem. Soc., volume 77, page 4708 (1955)
Calculated from NIST using POWD-12++

Radiation : CuKa1	*Filter* : Not specified
Lambda : 1.54060	*d-sp* : Calculated spacings
SS/FOM : F30=597(0.0014,35)	

2th	I	h	k	l
25.304	999	1	0	1
36.949	56	1	0	3
37.793	175	0	0	4
38.566	71	1	1	2
48.036	238	2	0	0
53.886	148	1	0	5
55.061	146	2	1	1
62.107	23	2	1	3
62.684	103	2	0	4
68.756	49	1	1	6
70.287	49	2	2	0
74.053	4	1	0	7
75.046	74	2	1	5
76.032	20	3	0	1
80.740	3	0	0	8
82.156	5	3	0	3
82.672	35	2	2	4
83.154	15	3	1	2
93.244	5	2	1	7
94.202	17	3	0	5
95.162	19	3	2	1
98.325	11	1	0	9
99.812	7	2	0	8
101.236	5	3	2	3
107.478	24	3	1	6
108.988	12	4	0	0
112.826	2	3	0	7
113.868	22	3	2	5
114.918	13	4	1	1
118.472	35	2	1	9
118.472	35	1	1	10
120.117	6	2	2	8
121.749	5	4	1	3
122.353	15	4	0	4
122.921	10	3	3	2
131.049	20	4	2	0
132.007	5	1	0	11
135.995	3	3	2	7
137.389	19	4	1	5
142.878	1	4	0	6
143.850	7	3	0	9

Pattern : 01-075-1149	Radiation = 1.540598	Quality : Alternate

$CaCu_3Ti_4O_{12}$

Calcium Copper Titanium Oxide
Also called: Calcium tricopper tetratitanium oxide

2th	I	h	k	l
16.947	20	1	1	0
24.056	13	2	0	0
29.573	10	2	1	1
34.279	999	2	2	0
38.475	4	3	1	0
42.315	141	2	2	2
45.891	5	3	2	1
49.262	406	4	0	0
52.470	2	4	1	1
55.545	1	4	2	0
58.512	1	3	3	2
61.386	248	4	2	2
64.184	2	5	1	0
69.597	1	5	2	1
72.230	158	4	4	0
74.824	1	5	3	0
77.387	1	4	4	2
79.926	1	5	3	2
82.443	76	6	2	0
84.947	1	5	4	1
87.440	16	6	2	2
89.929	1	6	3	1

Lattice : Body-centered cubic

S.G. : Im-3m   (229)

a = 7.39300

Mol. weight = 614.31

Volume [CD] = 404.08

Dx = 5.049

Z =   2

I/cor = 5.33

ICSD collection code: 030592
Test from ICSD: No R value given.
Test from ICSD: At least one TF missing.
Cancel:
Data collection flag: Ambient.

Deschanvres, A., Raveau, B., Tollemer, F., Bull. Soc. Chim. Fr., volume 1967, page 4077 (1967)
Calculated from ICSD using POWD-12++ (1997)

Radiation : CuKa1	*Filter :* Not specified
Lambda : 1.54060	*d-sp :* Calculated spacings
SS/FOM : F22=1000(0.0000,22)	

Pattern : 01-075-2188	*Radiation* = 1.540598	*Quality :* Calculated

(CaCu₂)Ti₄O₁₂

Calcium Copper Titanium Oxide
Also called: Calcium tricopper tetratitanium oxide

Lattice : Body-centered cubic		*Mol. weight =* 614.31
S.G. : Im-3 (204)		*Volume [CD] =* 403.75
a = 7.39100		*Dx =* 5.053
	Z = 2	*I/cor =* 5.76

ICSD collection code: 032002
Temperature factor: ITF
Cancel:
Data collection flag: Ambient.

Bochu, B., Deschizeaux, M.N., Joubert, J.C., Collomb, A., Chenavas, J., Marezio, M., J. Solid State Chem., volume 29, page 291 (1979)
Calculated from ICSD using POWD-12++

Radiation : CuKa1	*Filter :* Not specified
Lambda : 1.54060	*d-sp :* Calculated spacings
SS/FOM : F22=1000(0.0000,22)	

2th	I	h	k	l
16.952	27	1	1	0
24.062	3	2	0	0
29.581	38	2	1	1
34.289	999	2	2	0
38.486	73	0	1	3
42.327	49	2	2	2
45.904	40	3	2	1
49.276	263	4	0	0
52.485	13	4	1	1
55.562	3	0	2	4
58.529	8	3	3	2
61.405	401	4	2	2
64.204	5	0	1	5
69.618	6	1	2	5
72.252	92	4	4	0
74.848	17	4	3	3
77.413	7	6	0	0
79.951	7	6	1	1
82.471	101	6	2	0
84.975	1	1	4	5
87.470	1	6	2	2
89.961	2	1	3	6

Pattern : 01-078-0428	Radiation = 1.540598	Quality : Calculated

CuO

Copper Oxide

2th	I	h	k	l
36.637	769	1	1	1
42.559	999	2	0	0
61.761	450	2	2	0
74.003	171	3	1	1
77.893	109	2	2	2

Lattice : Face-centered cubic

S.G. : Fm-3m (225)

a = 4.24500

Z = 4

Mol. weight = 79.55

Volume [CD] = 76.49

Dx = 6.907

I/Icor = 5.43

ICSD collection code: 061323
Test from ICSD: No R value given.
Test from ICSD: At least one TF missing.
Cancel:
Data collection flag: Ambient.

Schmahl, N.G., Eikerling, G.F., Z. Phys. Chem. Neue Folge. (Wiesbaden), volume 62, page 268 (1968)
Calculated from ICSD using POWD-12++ (1997)

Radiation : CuKa1

Lambda : 1.54060

SS/FOM : F5=1000(0.0000,5)

Filter : Not specified

d-sp : Calculated spacings

| Pattern : 00-048-1548 | Radiation = 1.540598 | Quality : High |

CuO

Copper Oxide
Tenorite, syn

					2th	I	h	k	l
					32.509	13	1	1	0
					35.418	37	0	0	2
					35.544	100	1	1	-1
					38.709	98	1	1	1
					38.903	21	2	0	0
					46.260	3	1	1	-2
					48.717	30	2	0	-2
					51.344	1	1	1	2
					53.487	7	0	2	0
					56.743	1	0	2	1
					58.265	10	2	0	2
					61.526	20	1	1	-3
					65.813	10	0	2	2
					66.222	15	3	1	-1
					66.449	1	3	1	0
					67.905	6	1	1	3
					68.125	14	2	2	0
					68.907	1	2	2	-1
					71.683	1	3	1	-2
					72.373	5	3	1	1
					72.944	1	2	2	1
					74.978	6	0	0	4
					75.245	5	2	2	-2
					79.733	1	0	2	3
					80.157	2	2	0	-4
					80.241	1	1	1	-4
					82.362	4	3	1	-3
					83.065	2	2	2	2
					83.568	2	3	1	2
					83.568	2	4	0	0
					86.533	1	4	0	-2
					86.775	1	2	2	-3
					87.968	1	1	1	4
					88.054	1	1	3	0
					89.790	3	1	3	-1
					91.729	1	1	3	1
					95.565	1	2	0	4
					98.391	1	2	2	3
					98.391	1	0	2	4
					99.684	2	3	1	3
					101.935	1	4	0	2
					103.357	2	1	1	-5
					103.565	2	2	2	-4
					107.049	2	4	2	0
					109.519	1	1	3	-3
					110.170	3	4	2	-2
					111.181	1	4	0	-4
					113.489	2	1	1	5
					114.060	1	4	2	1
					114.060	1	3	3	-1
					115.744	1	1	3	3
					116.838	1	5	1	-1
					120.221	1	2	2	4
					120.509	3	3	3	1
					120.509	3	3	1	-5

Lattice : Base-centered monoclinic

S.G. : C2/c (15)

Mol. weight = 79.55

Volume [CD] = 81.22

Dx = 6.505

a = 4.68830

b = 3.42290

beta = 99.51

c = 5.13190

a/b = 1.36969

Z = 4

c/b = 1.49928

Sample preparation: Cu2 (OH)3 N O3 was thermally decomposed to form Cu O. This was annealed at 1000 C in air for 5 hours.
Additional pattern: To replace 00-005-0661.
Data collection flag: Ambient.

Langford, J., Louer, D., J. Appl. Crystallogr., volume 24, page 149 (1991)

Radiation : CuKa1

Lambda : 1.54060

SS/FOM : F30 = 65(0.0148,31)

Filter : Monochromator crystal

d-sp : Diffractometer

External standard : BaF2

Pattern : 00-046-1212	Radiation = 1.540598	Quality : High

Al₂O₃

Aluminum Oxide
Corundum, syn
Also called: α- Al2 O3

2th	**i**	**h**	**k**	**l**
25.579	45	0	1	2
35.153	100	1	0	4
37.777	21	1	1	0
41.676	2	0	0	6
43.356	66	1	1	3
46.176	1	2	0	2
52.550	34	0	2	4
57.497	89	1	1	6
59.740	1	2	1	1
61.118	2	1	2	2
61.300	14	0	1	8
66.521	23	2	1	4
68.214	27	3	0	0
70.420	1	1	2	5
74.299	2	2	0	8
76.871	29	1	0	10
77.226	12	1	1	9
80.422	1	2	1	7
80.700	2	2	2	0
83.217	1	3	0	6
84.359	3	2	2	3
85.143	1	1	3	1
86.363	2	3	1	2
86.503	3	1	2	8
88.997	9	0	2	10

Lattice : Rhombohedral

S.G. : R-3c   (167)

a = 4.75870

c = 12.99290

Z =   6

Mol. weight = 101.96

Volume [CD] = 254.81

Dx = 3.987

Sample source or locality: The sample is an alumina plate as received from ICDD.
General comments: Unit cell computed from d_obs.
Optical data: A–1.7604, B–1.7686, Sign—
Data collection flag: Ambient.

Huang, T., Parrish, W., Masciocchi, N., Wang, P., Adv. X-Ray Anal., volume 33, page 295 (1990)

Radiation : CuKa1

Lambda : 1.54056

SS/FOM : F25=379(0.0026,25)

Filter : Not specified

d-sp : Diffractometer

148

Pattern : 00-031-0022   Radiation = 1.540598   Quality : Indexed

LaAlO₃

Aluminum Lanthanum Oxide

2th	I	h	k	l
23.441	80	0	1	2
33.382	100	1	1	0
39.366	3	0	2	1
41.167	45	2	0	2
41.285	40	0	0	6
47.942	60	0	2	4
52.553	3	2	1	1
54.060	20	1	2	2
54.146	11	1	1	6
59.684	30	3	0	0
59.769	30	2	1	4
59.854	13	0	1	8
70.088	14	2	2	0
70.238	19	2	0	8
75.094	8	3	1	2
75.234	6	1	0	10
80.030	16	1	2	8

Lattice : Rhombohedral

S.G. : R3m   (160)

a = 5.36400

c = 13.11000

Mol. weight = 213.89

Volume [CD] = 326.67

Dx = 1.087

Additional pattern: To replace 00-009-0072.
Data collection flag: Ambient.

Mizuno, M. et al., Yogyo Kyokaishi (J. Ceram. Assoc. Jpn.), volume 82, page 631 (1974)

Radiation :

SS/FOM : F17=22(0.0220,34)

Filter : Not specified

d-sp : Not given

Pattern : 00-054-0869	Radiation = 1.540598	Quality : High

NdGaO₃

Gallium Neodymium Oxide

Lattice : Orthorhombic	*Mol. weight* = 261.96
S.G. : Pbnm (62)	*Volume [CD]* = 229.10
a = 5.41863	*Dx* = 7.595
b = 5.49568	
c = 7.69348	
a/b = 0.98598 Z = 4	
c/b = 1.39991	

Sample preparation: Single crystal was grown by the Czochralsky method.
Color: Violet
Temperature of data collection: Pattern taken at 12(1) K.
Additional pattern: To replace 00-021-0972.
Data collection flag: Ambient.

Vasylechko, L., Semiconductor Electronic Dept., L'viv Polytechnic National Univ., Ukraine., ICDD Grant-in-Aid (2002)

Radiation : Sync	*Filter* : Monochromator crystal
Lambda : 1.13341	*d-sp* : Diffractometer
SS/FOM : F30 = 47(0.0198,32)	

2th	i	h	k	l
19.997	4	1	0	1
23.002	118	1	1	0
23.075	62	0	0	2
25.783	79	1	1	1
32.532	232	0	2	0
32.822	999	1	1	2
33.006	250	2	0	0
34.609	65	0	2	1
36.609	2	1	2	0
36.933	2	2	1	0
38.499	2	1	2	1
38.789	5	1	0	3
38.804	23	2	1	1
40.276	99	0	2	2
40.672	91	2	0	2
42.254	38	1	1	3
43.732	6	1	2	2
44.011	3	2	1	2
47.038	360	2	2	0
47.191	170	0	0	4
48.488	45	0	2	3
48.588	71	2	2	1
51.512	4	1	2	3
51.761	6	2	1	3
53.033	18	2	2	2
53.139	38	1	1	4
53.321	18	3	1	0
54.106	112	1	3	1
54.741	15	3	1	1
58.254	219	1	3	2
58.504	141	0	2	4
58.805	137	2	0	4
58.859	301	3	1	2
59.927	24	2	2	3
62.287	3	2	3	1
62.691	3	3	2	1
62.691	3	1	0	5
62.856	2	3	0	3
64.791	66	1	3	3
65.199	7	1	1	5
65.358	5	3	1	3
68.178	31	0	4	0
68.850	204	2	2	4
69.287	49	4	0	0
69.410	52	0	4	1
70.000	10	0	2	5
72.264	4	2	3	3
72.651	4	2	1	5
72.876	6	4	1	1
73.407	3	1	3	4
73.559	4	3	3	0
73.824	11	0	0	6
73.941	19	3	1	4
74.119	6	4	0	2
74.752	46	3	3	1
77.874	37	2	4	0
78.296	89	3	3	2
78.526	148	1	1	6
78.664	50	4	2	0
78.966	28	0	4	3
79.044	65	2	4	1
79.607	26	2	2	5
79.830	17	4	2	1
82.296	7	4	1	3
83.020	8	0	2	6
83.278	10	2	0	6
83.318	11	4	2	2
83.957	36	1	3	5
84.107	37	3	3	3
84.480	8	3	1	5
87.075	30	0	4	4
88.107	48	4	0	4
88.298	58	2	4	3
89.071	14	4	2	3
91.138	3	4	3	1
91.246	3	3	2	5
91.715	2	5	0	1
92.157	4	3	3	4
92.298	11	2	2	6
92.419	60	1	5	1
92.824	8	5	1	0
93.536	5	1	1	7
95.881	18	1	5	2
96.361	41	2	4	4
96.622	61	1	3	6
97.136	159	4	2	4

2th	i	h	k	l
97.136	159	3	1	6
97.438	111	0	4	5
97.438	111	5	1	2
97.992	12	0	2	7

Appendix B

Conventional crystal structure of lanthanum aluminate

(LaAlO$_3$, LAO)

(a)   (b)
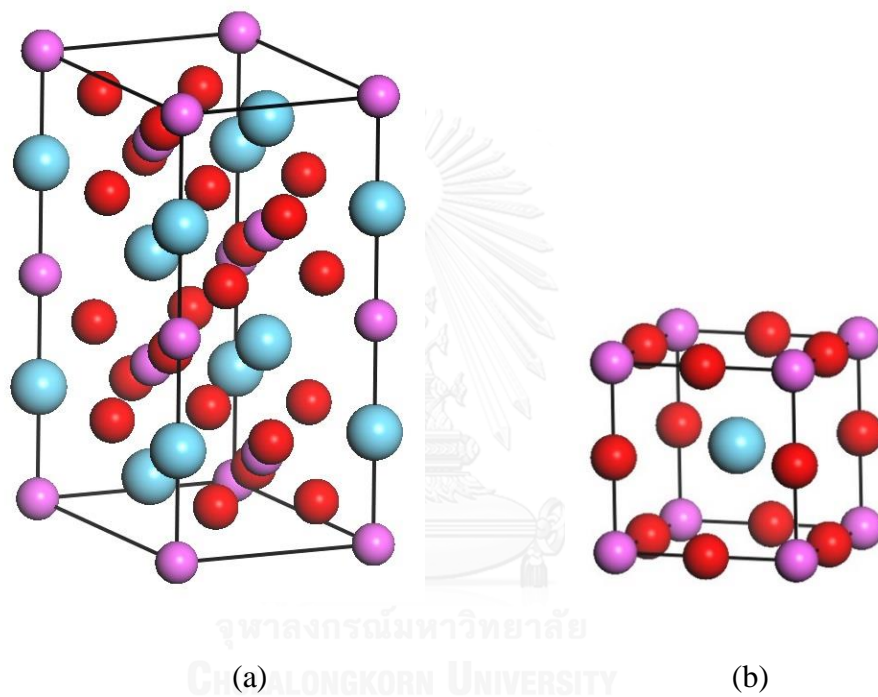
(a) The Rhombohedral phase and (b) The cubic phase of LAO

Rhombohedral structure defined as hexagonal in space group ($R\bar{3}c$, No.167)

	x	y	z
La	0	0	0.25
Al	0	0	0
O	0.527	0	0.25

Lattice parameter $a = b = 5.3589$ Å $c = 13.0858$ Å

                                       $\alpha = \beta = 60°$ $\gamma = 120°$

Cubic Structure in space group ($Pm\bar{3}m$, No. 221)

|	x	y	z
La	0.5	0.5	0.5
Al	0	0	0
O	0.5	0	0

Lattice parameter $a = b = c = 3.7913$ Å

                                       $\alpha = \beta = \gamma = 90°$

Conventional crystal structure of neodymium gallate (NdGaO₃, NGO)
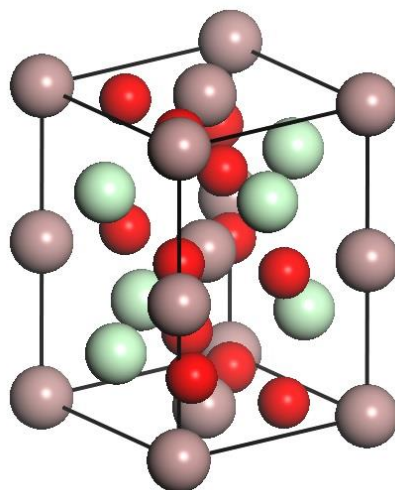
The crystal structure of NGO

Orthorhombic structure in space group (*Pbnm*, No.62)

	x	y	z
Nd	0.49092	0.04142	0.25
Ga	0	0	0.5
O1	0.08	0.0174	0.75
O2	0.7107	0.2097	0.5422

Lattice parameter   a = 5.4276 Å   b = 5.4979 Å   c = 7.7078 Å

α = β = γ = 90°

VITA

I were born in Chiangmai province in 1980.

I began going to preschool at Chantorn Wittaya in the third year after being born.

I graduated elementary school in 1991 at Chantorn Wittaya school, Bangkok.

I finished learning at Phuttha Bucha middle and high school in 1994 and 1997 respectively.

I got bachelor degree in Physics science at Srinakarinwirot University in 2001.

I also got the master degree of science in physics at Chulalongkorn University in 2006.

I studied English for academic purpose at the English academy the University of Auckland, New Zealand in 2010 and continued taking the intensive English and exam skills at Crown instituted studies in Auckland city in 2011.

I decided to pursue a PhD study in Nanoscience and Technology at Chulalongkorn University in Thailand from 2012 to 2015.